13:40:19 OCA PAD AMENDMENT - PROJECT HEADER INFORMATION 03/28/96

Active

Project #: E-18-673 Cost share #: E-18-330 Rev #: 2
Center # : 10/24-6-R8128-0A0 Center shr #: 10/22-1-F8128-0A0 OCA file #:
Work type : RES
Contract#: AGMT DTD 940502 Mod #: ADM. REVISION Document : CONT
Prime #: Contract entity: GTRC

Subprojects ? : N CFDA:
Main project #: PE #:

Project unit: MSE Unit code: 02.010.112
Project director(s):
SPEYER R F MSE (404)853-9944

Sponsor/division names: SS ENERGY ENVIRONMENTAL / ROCKFORD, IL
Sponsor/division codes: 218 / 109

Award period: 940101 to 951121 (performance) 951121 (reports)

Sponsor amount	New this change	Total to date
Contract value	0.00	232,819.00
Funded	0.00	232,819.00
Cost sharing amount		40,535.00

Does subcontracting plan apply ?: N

Title: FLAME SUPPORT LAYER OPTIMIZATION FOR THE NEXT GENERATION POROUS RADIANT BURNE

PROJECT ADMINISTRATION DATA

OCA contact: Jacquelyn L. Bendall 894-4820

Sponsor technical contact

SHYAM N. SINGH
(815)229-5615

SS ENERGY ENVIRONMENTAL INT'L. INC.
129 S. PHELPS AVE., SUITE 406
ROCKFORD, IL 61108

Sponsor issuing office

SHYAM N. SINGH
(815)229-5615

SS ENERGY ENVIRONMENTAL INT'L INC.
129 S. PHELPS AVE., SUITE 406
ROCKFORD, IL 61108

Security class (U,C,S,TS) : U ONR resident rep. is ACO (Y/N): N
Defense priority rating : N/A N/A supplemental sheet
Equipment title vests with: Sponsor X GIT
ACQUISITION COST > $1,000
Administrative comments -
ISSUED TO REVISE REPORTING REQUIREMENTS IN ACCORDANCE WITH SPONSOR'S LETTER
DATED NOVEMBER 21, 1995.

CA8120

Georgia Institute of Technology
Office of Contract Administration
PROJECT CLOSEOUT - NOTICE

15-SEP-1997 16:00

4
(2)

Closeout Notice Date 15-SEP-1997

Project Number E-18-673 Doch Id 36576

Center Number 10/24-6-R8128-0A0

Project Director SPEYER, ROBERT

Project Unit MSE

Sponsor SS ENERGY ENVIRONMENTAL/ROCKFORD, IL

Division Id 4700

Contract Number AGMT DTD 940502 Contract Entity GTRC

Prime Contract Number

Title FLAME SUPPORT LAYER OPTIMIZATION FOR THE NEXT GENERATION POROUS RADIANT BU

Effective Completion Date 21-NOV-1995 (Performance) 21-NOV-1995 (Reports)

Closeout Action:	Y/N	Date Submitted
Final Invoice or Copy of Final Invoice	Y	19-APR-1996
Final Report of Inventions and/or Subcontracts	N	
Government Property Inventory and Related Certificate	Y	
Classified Material Certificate	N	
Release and Assignment	N	
Other	N	

Comments

Distribution Required:

Project Director/Principal Investigator	Y
Research Administrative Network	Y
Accounting	Y
Research Security Department	N
[redacted]	Y
Research Property Team	Y
Supply Services Department	Y
Georgia Tech Research Corporation	Y
Project File	Y

E-18-673
1 + 2 (new)

RADIANT EFFICIENCIES OF COMMERCIALLY MANUFACTURED GAS RADIANT BURNERS

Robert F. Speyer, Wen-Yi Lin, and Gaurav Agarwal

School of Materials Science and Engineering, Georgia Institute of Technology, Atlanta, GA 30332

ABSTRACT

The radiant efficiencies of five gas radiant burners were evaluated as a function of gas/air mixture and combustion intensity. Solaronics and Krieger burners showed the highest levels of maximum efficiency (53.9% and 52.1%, respectively), the Hi-Tech burner showed a moderate maximum efficiency (39.4%), and the Acotech (without screen flame support layer) and Marsden burners showed the lowest maximum efficiencies (28.4% and 25.5%, respectively). At combustion intensities above 250 kW/m^2, the Krieger burner exceeded the Solaronics burner in efficiency. High efficiency required a flame support layer which further extracted sensible heat from combustion products. A theoretical maximum efficiency model showed that the performances of these burners fell significantly below that which is possible. Based on the model, optimum burners: approach blackbody emittance, demonstrate heat transfer between combustion products and solids to the point where their temperatures approach, and have a large fraction blocking surface area flame support layer.

1 INTRODUCTION

Infrared heating is used in a number of industrial applications such as in powder coat painting and drying operations in the pulp and paper industry. The use of natural gas as the energy source for infrared heating has shown an increased market share over the years, largely due to the economics of gas versus electric power. The function of gas radiant heaters is to convect the heat of combustion to solid surfaces which in turn radiate to the load. Solids have significantly higher emissivities than gases so that the radiant intensity is much greater than with an open flame.

Varying conceptions of these burners are available on the open market. The work presented herein correlates the radiant performance of five of these burners to the materials and geometries of their construction. These five are representative of the breadth of unique designs available. Preliminary characterization of these burners was performed using scanning electron microscopy (with energy dispersive spectroscopy) along with x-ray diffraction.

The Acotech (N. V. Acotech S. A., Belgium) burner (Figure 1) is a metal (Fe-Cr-Al) fiber mat. The fibers are approximately 40 μm in diameter. This mat is mounted on a distributor housing from which the gas/air premix enters. As an option, a ported metal screen can be used upstream of the fiber mat, functioning as a distributor. A fiber mat with periodic perforations is also available, which requires a lower pressure gradient across the mat. Stable radiant surface combustion has been demonstrated both experimentally[1] and with models[2], over a wide range of thermal inputs. The Hi-Tech (Hi-Tech Ceramics, Inc., Alfred Station, NY) burner (Figure 2) consists of a porous cordierite ($Mg_2Al_4Si_5O_{18}$) diffuser base where the combustible mixture enters, and a much more open flame support layer within which combustion takes place. Combustion within porous ceramic media has been extensively evaluated[3]–[7]. Both the Acotech and Hi-Tech burner materials were compression sealed (using thermally insulating braids of fiber-wool) to Eclipse (Rockford, IL) housings. The Solaronics (Solaronics Process S. A., France) burner (Figure 3) is a single unit consisting of a mullite/cordierite ported tile diffuser base, a metal (Fe-Al-Cr-Co) screen flame support layer, and a steel housing. All hot metal parts are insulated from the housing by a alumina/cordierite inserts. Hexagonally shaped openings surround each gas/air exit port. The Krieger (E. Providence, RI) burner (Figure 4) is designed so that the gas/air mixture is forced through nozzles which are thermally isolated by aluminosilicate glass fiber-wool. Ignition takes place on the downstream side of these nozzles and combustion products are forced around a series of interconnected circular metal alloy plates (flame retention plate) and then past a metal screen. The housing is thermally isolated from the radiating metal through a layer of aluminosilicate glass wool. The Marsden (Marsden, Inc., Pennsauken, NJ) burner (Figure 5) is approximately six times the area as the other burners evaluated. It is composed of a 2.54 cm thick Si-Al-Zr oxide glass fiber mat through which the premix diffuses and combusts. All burners with exception of the Marsden burners were provided courtesy of the respective manufacturer.

Figure 1: a) Acotech metal fiber mat, 15.7 cm × 15.7 cm, 2.2 mm thick. b) Perforated metal fiber mat. c) Microstructure of metal fibers before use as a radiant burner. d) Microstructure of metal fibers after use as a radiant burner showing an oxide scale on the surface.

Figure 2: Tri-layer Hi-Tech burner, 14.0 cm × 14.0 cm, 21 mm thick. a) Front (downstream) view. b) Side view of a fractured burner tile. The burner tile used in this work was similar, but a bi-layer design; 25.6 pores per cm base layer, 3.9 pores per cm flame support layer.

Figure 3: a) Solaronics burner, 10.5 cm × 14.0 cm outer dimensions. Screen: 1.5 mm dia. wire, 5 mm separation. b) Magnified view showing rough-textured ported tile. Burner tile hexagon 2.5 mm dia., gas/air port hole 1.25 mm dia.. Distance between the center of screen and the top edge of ceramic tile: 9.5 mm.

Figure 4: a) Schematic cutaway view of the Krieger burner. The ceramic fiber nozzle exit was 2.22 cm below the flame retention plate. b) Front view, outer dimensions 19.8 cm × 14.8 cm. The screen was 1.28 cm above the flame retention plate, and was made up of 1.6 mm dia. wire, 5 mm separation.

Figure 5: a) Full view of the Marsden burner, outer dimensions 61 cm × 29 cm. b) Magnified view of glass fiber mat. c) Microstructure of glass fiber mat.

The Marsden burner was provided by a competing burner manufacturer.

2 EXPERIMENTAL PROCEDURE

2.1 Instrumentation

The burner testing facility was described in detail in our previous work[8] and is shown in schematic form in Figure 6. Separate mass flow controllers were used for gas and air lines, with input pressures of 68.9 kPa and 280 kPa, respectively. The air line fed through a preheat system (Sylvania Emissive Products, Exeter, NH) with an upstream chromel/alumel thermocouple for temperature control. Gas and air flow, as well as preheat temperature were maintained by proportional-integral-derivative feedback control (on flow or preheater element power) from a 486-level computer. All programming was in Microsoft QuickBasic 4.5. Gas and air lines converged into a premixer which fed into a burner housing. These housings could be exchanged via a screw thread fitting on the mixer. The burner surfaces were mounted perpendicular to the floor.

A radiometer (total radiation pyrometer) was positioned at an angle of 24°C from the burner normal and distance of 33.6 cm, so that the entire field of view of the detector was filled with the burner face. The radiometer consisted of a blackened water-cooled thermoelectric detector, viewing the burner through a single crystal sapphire window, and either a 7 or 15° view angle restrictor. The radiometer was aimed by removing the detector and manually adjusting the position of the aperture housing while viewing through it. The 15° view angle restrictor was used for all studies unless otherwise stated.

A two-hole 2.3 mm diameter alumina rod was mounted on a movable stage, in turn positioned by computer instruction. Fed through the rod was a Pt/Pt-10%Rh thermocouple using 0.127 mm dia. wire and a fine bead. A 50 μm inner diameter fused silica capillary was positioned through one of the holes so that its opening was in line with the thermocouple junction. This capillary fed into a quadrapole mass spectrometer for gas analysis. The movable stage was positioned by the computer so that the capillary and thermocouple junction were in near-contact with the base layer of the burner, and then relocated incrementally (1 mm steps) to more distant positions after measurements were taken. This fostered analysis of the location and progress of combustion.

To study the effect of atmospheric entrainment on the operation of these burners, an

Figure 6: Schematic of the Georgia Tech radiant burner testing facility.

Table I: Gas Composition (Atlanta Gas Light Company) for Gas/Air Ratio Calculation

Gas Composition	Stoichiometric Combustion
97.34% CH_4	$CH_4 + 2O_2 = 2H_2O + CO_2$
1.61% C_2H_6	$C_2H_6 + \frac{7}{2}O_2 = 3H_2O + 2CO_2$
0.24% C_3H_8	$C_3H_8 + 5O_2 = 4H_2O + 3CO_2$
0.05% C_4H_{10}	$C_4H_{10} + \frac{13}{2}O_2 = 5H_2O + 4CO_2$
0.08% C_5H_{12}	$C_5H_{12} + 8O_2 = 6H_2O + 5CO_2$
0.04% C_6H_{14}	$C_6H_{14} + \frac{19}{2}O_2 = 7H_2O + 6CO_2$
0.04% C_7H_{16}	$C_7H_{16} + 11O_2 = 8H_2O + 7CO_2$
0.62% CO_2	

enclosure was manufactured out of aluminum. This enclosure connected snugly to the upstream entry throat of the burner housing, and extended with its longest dimension in the direction perpendicular to the burner face (length 91.5 cm, width 31 cm, height: 26 cm, far end gas exit opening diameter: 5 cm). A stack gas analyzer (Model 6000HC, Cosa Instruments Corporation, Norwood, NJ) probe was sealed into the enclosure approximately half the distance of its length. This probe consisted of a chromel/alumel thermocouple and a suction device drawing sampled gases into a detector box. This box contained solid electrolyte sensors designed to determine the concentration of O_2, CO, CO_2, NO, NO_2, and combined NO_x. Full scale range of CO sensitivity was 8000 ppm, with an accuracy of ± 2 ppm. Pans of water were placed on top of the enclosure so that its temperature would not exceed the melting point of aluminum.

2.2 Calibration

In contrast to our previous work[8], mixtures were formulated by varying the gas flow rate, maintaining the air flow rate constant. This facilitated changes in mixtures with only minute changes in mixture flow rate, since the gas volume required for stoichiometric combustion was approximately one tenth that of the air volume. The composition of gas and the requirements for stoichiometric combustion are shown in Table I. Assuming that the ratio of oxygen to air is 0.20946[9], the gas to air ratio for stoichiometric combustion from calculations based on Table I is 0.103. To distinguish this method from previous

work, mixtures will be designated on the basis of percent excess gas. For example, the 20% excess gas designation would have a gas to air ratio of $1.2 \times 0.103 = 0.125$, and the -20% excess gas designation would have a gas to air ratio of $0.8 \times 0.103 = 0.082$.

The manufacturer's calibration for the gas and air mass flow controllers were used. These calibrations were based on the type of gas used and the approximate input pressure. The manufacturer's stated accuracy was $\pm 1\%$ of full scale. The stack gas analyzer runs a pre-programmed self-calibration routine based on evaluation of unaltered atmospheric air, just prior to use.

The radiometer used in this work generated a thermoelectric voltage proportional to the irradiation incident on its surface. Of interest was the hemispherical radiosity (referred to herein as radiosity), which is the radiant power emitting (and reflecting) hemispherically from a unit surface. With view restrictors, the detector could be positioned adequately close to the radiating surface so that the entire (unrestricted) field of view of the detector surface was filled with the radiating surface. If there is no variation in the radiant flux with solid angle from the surface normal, the radiating surface may be considered a diffuse emitter. For such a diffuse emitter, moving the detector farther away (still filling the field of view) permits view of a greater area of the radiating surface; however, from any given point on the radiating surface, a smaller solid angle of radiation will be incident on the detector. The net result is that moving the detector does not change the irradiation incident on it—so long as the un-restricted field of view is still filled with the radiating surface. A mathematical proof of this is provided as an appendix. On that basis, the irradiation is constant with radiometer position. Since radiosity and the measured irradiation are linearally related, and the irradiation and the transducer output are linearally related, the instrument can be calibrated to measure radiosity directly. The diffuse emitter assumption was adopted, as well as evaluated in this work.

Two blackbody cavities were constructed to use as calibration sources for the total radiation pyrometer. A cylindrical graphite cavity of inside diameter 2.5 cm and length 14.0 cm was used with a front cap having an opening of 1.5 cm diameter. Graphite is known to closely emulate blackbody characteristics. However, in an oxidizing environment, a high partial pressure of carbon dioxide would be expected to form in the optical path between the back wall of the cavity and the detector. This would result in calibration errors in spectral regions where CO_2 gas is emitting/absorbing, which (in the wavelength

range of blackbody radiation) is 2400-2900 and 4200-4700 nm. H_2O vapor also has an absorption/emission peak at 2400-2900 nm[15]. To calibrate without the effect of CO_2 absorption, a steel cavity was manufactured and used. When exposed to elevated temperatures, the steel formed a rough iron oxide scale, which also approached blackbody emittance. This cavity was conical in shape, where the back wall was greater in diameter (5.89 cm) than the view hole (1.27 cm). The back wall had a conical shape with a cone angle of 155.6°. The shape of the cavity was intended to discourage line of sight reflection of radiation originating from the exterior, back out the entry port. The cavity was 10.69 cm long. Both cavities were of adequate size so that the entire field of view of the total radiation pyrometer detector (with view restrictors) was filled by the back walls. The cavities were elevated on refractories inside a small Kanthal Al-wound furnace, with computer feedback control on furnace temperature. Fiberboard insulation was used to insulate all portions of the cavity but its opening from the ambient. The control system was instructed to raise the furnace temperature to a specified value and hold for 120 min. After the furnace temperature was clearly stabilized (roughly 30 min after the soak temperature was first reached), a Pt/Pt-10%Rh thermocouple junction (0.127 mm dia. wire) in an alumina sleeve was inserted to make firm contact with the back wall, and time was allotted ($\sim$ 5 min) for the thermocouple junction temperature to equilibrate with the cavity wall. The voltage from the thermocouple was read with a microvolt meter and converted to temperature, accounting for cold junction temperature (measured by a thermometer). Temperatures were confirmed using a Pt-6$\hat{\text{R}}$h/Pt-30%Rh thermocouple. The process was repeated for additional temperatures, for both the 15 and 7° apertures. The Stefan-Boltzmann blackbody radiation law was then used to determine the radiosity from the blackbody cavities of known (measured) temperatures. The resulting calibration lines of radiosity versus detector output are shown in Figure 7. There is good agreement between the calibrations using the graphite and steel cavities. The radiometer was then sent to an independent facility (Optronic Laboratories, Inc., Orlando, FL) to calibrate against their blackbody source. Their results, also shown in the figure, are in good agreement with calibrations from the graphite and steel cavities.

The radiant efficiency (referred to as efficiency in this work) was calculated as:

$$e = \frac{R_T}{\dot{V}_g \Delta H_c / A}$$

Figure 7: Calibration data for total radiation pyrometers. 15° or 7° refers to the field of view angle of the aperture, steel or graphite refers to the blackbody cavity used. Least squares lines were calculated where radiosity in kW/m^2 is y and transducer output in mV is x. 7° aperture and steel cavity: $y = 7.78 + 9914.89x$, 15° aperture and steel cavity: $y = 11.16 + 2543.92x$, 15° aperture and graphite cavity: $y = -4.29 + 2824.53x$.

where e is the efficiency, R_T is the radiosity, $\dot{V}_g$ is the volume flow rate of gas at room temperature, ΔH_c is the heat content per unit volume of gas (38.19 MJ/m^3, Atlanta Gas Light Company, Atlanta GA), and A is the square area of the burner. Only regions at which gas/air mixture emerged and in turn resulted in surface heating were used in the determination of the square area of the burner. These "hot dimensions" were: Solaronics: 18.1 cm × 11.6 cm, Krieger: 18.9 cm ×13.3 cm, Marsden: 61 cm × 29 cm, Acotech: 14.3 cm ×14.3 cm, Hi-Tech 13.2 cm × 13.2 cm.

2.3 Experimental Methods

As shown in Figure 8 from our previous work[8], the radiosity of a burner reaches a saddle point for a given gas/air mixture, and the mixture of maximum radiosity does not change with flow rate. For that reason, in the present work, the flow rate was held at a specified value while mixtures were varied: The burners were ignited on the -20% excess gas (gas deficient, or lean) side, and left to reach steady state conditions for 5 min. The mixture was then changed in 1% excess gas intervals with 1 min pauses before radiosity measurements were taken. The experiment was repeated in a similar fashion starting from 20% excess gas, stepping to -20% excess gas. The average of the mixtures corresponding to the maxima in efficiency was used as the fixed mixture for subsequent flow studies. Flow studies were performed from high flow rate to low flow rate, with an 8 min initial soak, and a 2 min hold after each flow adjustment before measurements were taken. Mixture flow rate, in this work, is expressed in terms of combustion intensity:

$$CI = \frac{\dot{V}_g \Delta H_c}{A}$$

which normalizes flow for different burner sizes.

The effect of radiometer orientation relative to the burner face was studied at 10° intervals from orthogonal orientation to 20° from the burner plane (Figure 9). To continue to fill the field of view of the radiometer at oblique angles, the detector was moved closer to the burner. Burners were left at a specified mixture and flow for 5 min prior to taking radiosity measurements. Measurements were made with the radiometer on the left side of the burner, measuring the most oblique angle, and rotating around to the right. The radiometer was sighted based on orientation of the aperture housing using a laser pointer.

Burners were first ignited, then the enclosure was sealed around the burner for combus-

Figure 8: Radiosity of a Hi-Tech burner as a function of mixture and flow. In this previous work[8], mixtures were obtained by varying air flow rate, keeping gas flow rate constant.

Figure 9: Measurement of irradiance at various angles. Distances shown are in cm.

tion product analyses. Initial soak periods, and hold times between mixture steps were the same as previously indicated. Combustion product analyses were performed during an additional 30 s hold after the normal hold times. The Hi-Tech burner was not evaluated in this and a selection other analyses due to inadvertent fracture during handling. Combustion product analysis for the Marsden burner was not performed due to its large size.

3 MODEL FOR MAXIMUM EFFICIENCY

Under steady state, the heat flow of combustion must be equal to the heat carried away by the exiting combustion products plus that radiated by the solid:

$$\Delta H_c \dot{V}_g = \dot{n} \Delta \bar{H}_e + \epsilon A \sigma \left({T_s}^4 - {T_L}^4 \right) \tag{1}$$

where $\dot{n}$ is the mole flow rate of the combustion products, $\Delta \bar{H}_e$ is the sensible heat of the exiting combustion products per mole, ϵ is the greybody emittance of the solid, A is the area of emitting surface, σ is the Stephan-Boltzmann constant, T_s is the temperature of the radiating solid, and T_L is the temperature of the load (ambient at 298 K). Since the volume flow rate of gas and air are known, the mole flow rate of the gas/air mixture can be determined by the ideal gas law, stipulating atmospheric pressure p and room temperature T_L. The volume flow rate of exiting combustion products is related to the volume flow rate of gas and air by the molar ratio of products to reactants Z. Thus:

$$\dot{n} = \frac{\left(\dot{V}_g + \dot{V}_a \right) Z p}{R T_L} \tag{2}$$

where $\dot{V}_a$ is the volume flow rate of air. Based on Table I, $Z = 1.001$. On a per mole of natural gas basis, 1.0250, 2.0184, and 7.673 moles of CO_2, H_2O, and N_2, respectively, form as combustion products. The enthalpy change (from room temperature) of combustion products of this composition can then be calculated using tabulated data[12] (Figure 10).

The greatest heat transfer from the combustion products to solid surfaces will occur when the solid and exit gas temperatures are equal. With this assumption, the only variable in equation 1 is T_s, which can be determined by iterative calculation via a computer program. From this, the maximum theoretical efficiency of the burner can be calculated

Figure 10: Sensible heat of products of stoichiometric combustion of natural gas (Atlanta Gas Light Company) and air.

as:

$$e = \frac{\epsilon A \sigma \left({T_s}^4 - {T_L}^4 \right)}{\Delta H_c \dot{V}_g} \tag{3}$$

The surface temperature and theoretical maximum efficiency of a burner as a function of combustion intensity, using this model, are shown for various greybody emittances in Figure 11.

This model is appropriate for comparison with the Marsden and Acotech burners, where a constant temperature single emitting surface can be assumed. For the Solaronics and Krieger burners, the metal screen flame support layers would interact with radiation and combustion products exhausted from the base layer. To model this configuration, heat balances are established based on the schematic shown in Figure 12. For maximum efficiency, it is again assumed that the temperature of exhaust combustion products must equal the temperature of the base. It is further assumed that the temperature of the fraction of combustion products convecting to the flame support layer also exits the flame support layer at the same temperature as the flame support layer. Under these conditions the heat balance at the base is:

$$\Delta H_c \dot{V} = f \epsilon \sigma A \left({T_A}^4 - {T_B}^4 \right) + f \dot{n} \Delta \bar{H}_{T_A \rightarrow T_B} + (1-f) \epsilon \sigma A \left({T_A}^4 - {T_L}^4 \right) + (1-f) \dot{n} \Delta \bar{H}_{T_A \rightarrow T_L} \tag{4}$$

where f is the fraction closed surface area of the flame support layer, T_A, T_B, and T_L are absolute temperatures of base surface, flame support layer and load (ambient, 298 K), respectively, $f \Delta \bar{H}_{T_A \rightarrow T_B}$ is the sensible heat per mole given up from base exhaust combustion products to the flame support layer, and $\Delta \bar{H}_{T_A \rightarrow T_L}$ is the sensible heat per mole given up from base exhaust combustion products to the load. The heat balance at the flame support layer is:

$$f \epsilon \sigma A \left({T_A}^4 - {T_B}^4 \right) + f \dot{n} \Delta \bar{H}_{T_A \rightarrow T_B} = f \epsilon \sigma A \left({T_B}^4 - {T_L}^4 \right) + f \dot{n} \Delta \bar{H}_{T_B \rightarrow T_L} \tag{5}$$

where $\bar{H}_{T_B \rightarrow T_L}$ is the sensible heat per mole given up from combustion products in contact with the flame support layer to the load.

In equations 4 and 5, values for greybody emittance (assumed same for both base and flame support layer), fraction closed surface area, volume flow rate, and load temperature are assigned. On that basis, the two variables, namely the base and flame support layer temperatures, can be determined. This was performed using simplex numerical optimization routine[13]. The theoretical maximum efficiency of the burner ensemble (e.g. base

Figure 11: Theoretical temperatures and efficiencies for a burner where the exit combustion product temperature is assumed equal to the temperature of the radiating solid. Numbers in the figure are the greybody emittances.

Figure 12: Heat balances for a burner with a flame support layer. The subscript r refers to radiation and e refers to convection from exhausted combustion products. Subscripts such as AB refer to source and sink locations respectively, where A is the base, B is the flame support layer, and L is the load at 25°C.

plus flame support layer) was then determined as:

$$e = \frac{f\epsilon\sigma A\left({T_A}^4 - {T_B}^4\right) + (1-f)\,\epsilon\sigma A\left({T_A}^4 - {T_L}^4\right)}{\Delta H_c \dot{V}} \tag{6}$$

Fixing the greybody emittance at 0.8, base and screen temperatures for varying values of f are shown in Figure 13. The corresponding theoretical maximum efficiencies are plotted in Figure 14. Fixing the fraction closed surface of the flame support layer at 0.5, base and screen temperatures for varying values of ϵ are shown in Figure 15, and the corresponding theoretical maximum efficiencies are shown in Figure 16.

4 RESULTS

Figures 17 and 18 show the radiosity and efficiency behavior of the Acotech burner as a function of mixture. The radiosity/efficiency of the burner during incremental steps from lean to rich are below those values for steps in the other direction. The average maximum in efficiency was judged to be 7% excess gas. By comparison to the maximum in efficiency, the maximum in radiosity was shifted to a more rich mixture. Although similar plots were generated for other burners, only the lean-to-rich directions are shown in Figures 19 and 20. Maxima in efficiency were calculated from the average of the maxima from rich-to-lean and lean-to-rich experiments. The determined maxima were, in terms of percent excess gas: Acotech: 7, Hi-Tech 7.5, Solaronics: 6, Krieger: 6, Marsden: 2.

The mixture of maximum efficiency was fixed for each burner for the subsequent flow rate studies. The mixture and flow studies yielded self consistent results as implied by Figure 21. Figure 22 shows the effect of working from low to high versus high to low combustion intensities for the Krieger burner. This burner, which had demonstrated the greatest thermal lag of all the burners, showed negligible shift for the two directions of flow rate. Figures 23 and 24 show the radiosity and efficiency results respectively for all the tested burners under high-to-low combustion intensity conditions. Superimposed in Figure 24 are theoretical maximum efficiencies for no flame support layer ($f = 0$), a flame support layer of Solaronics dimensions ($f = 0.56$), and a flame support layer of Krieger dimensions ($f = 0.66$). In all cases, the emittances of solid surfaces are assumed to be unity. Radiosities for all burners increased with increasing combustion intensity, while the efficiencies either traced through a maximum, or continuously decreased with

Figure 13: Base and flame support layer temperatures from the theoretical maximum efficiency model. Numbers next to each curve correspond to assumed value of f. Solid lines: base surface. Dashed lines: flame support layer. The assumed value of ϵ is 0.8.

Figure 14: Theoretical maximum efficiencies assuming a greybody emittance of 0.8. Numbers next to each curve correspond to assigned values of f.

Figure 15: Base and flame support layer temperatures from the theoretical maximum efficiency model. Numbers next to each curve correspond to the assumed value of ϵ. Solid lines: base surface. Dashed lines: flame support layer. The assumed value of f is 0.5.

Figure 16: Theoretical maximum efficiencies assuming the fraction closed surface of the flame support layer is 0.5. Numbers next to each curve correspond to assigned values of ϵ.

Figure 17: Rich-to-lean and lean-to-rich radiosity measurements of the Acotech burner as a function of mixture, using a combustion intensity of 221 kW/m^2.

Figure 18: Efficiency plots for the same experiment as in Figure 17.

Figure 19: Radiosity as a function of mixture for various burners. Combustion intensities in kW/m^2 were Krieger: 179, Solaronics: 216, Hi-Tech: 258, Acotech: 221, Marsden: 160.

Figure 20: Efficiency plots for the same experiment as in Figure 19. Efficiencies should not be compared since combustion intensities for each burner were not matched.

Figure 21: Mixture and flow studies for the Acotech burner.

Figure 22: Radiosity and efficiency as a function of combustion intensity for the Krieger burner. Mixture: 6% excess gas.

Figure 23: Comparative radiosities of commercial radiant burners.

Figure 24: Comparative efficiencies of commercial radiant burners. Theoretical maximum efficiencies for blackbody surfaces ($\epsilon = 1$) with varying closed area fraction flame support layers are superimposed.

increasing combustion intensity (with the exception of the Marsden burner). The Solaronics burner demonstrated the highest efficiency of 53.9% at a combustion intensity of 188.5 kW/m^2. The Krieger burner demonstrated a more unchanging efficiency behavior than the Solaronics and showed higher efficiencies at combustion intensities above 250 kW/m^2. The Hi-Tech burner showed a moderate efficiency which only decreased slightly with increasing combustion intensity, to the point where it approached the performance of the Solaronics burner at ~500 kW/m^2. The Marsden burner was not evaluated at combustion intensities exceeding 272.4 kW/m^2, due to flow limit restrictions of the mass flow controllers. Figure 25 shows CH_4 analysis for the burners as a function of combustion intensity. Combustion intensities where a significant change in CH_4 with position correlate well to combustion intensities just below the those of the maxima in experimentally measured efficiency in Figure 24 (see discussion).

Figure 26 shows the variation of radiosity with radiometer angle relative to the burner face. The burners demonstrated a general independence of radiosity with detector angle. Some burners, e.g. Hi-Tech, showed a slight increase in radiosity as angles deviated from orthogonal orientation. At oblique angles, the radiometer with the 15° aperture showed inconsistent results.

A comparison of CO analyses for the Krieger, Acotech, and Solaronics burners is shown in Figure 27. A precipitous jump in CO content can be seen at 3%, 5% and 8% excess gas for the three burners, respectively.

5 DISCUSSION

The theoretical efficiencies shown in Figure 11 are independent of surface area. This can be seen by combining equations 1 and 3:

$$e = \frac{\epsilon A \sigma \left(T_s^4 - T_L^4 \right)}{\Delta H_c \dot{V}_g} = \frac{\Delta H_c \dot{V}_g - \dot{n} \Delta \bar{H}_e}{\Delta H_c \dot{V}_g}$$

where it is apparent that none of the terms on the right hand side have an area dependence. For a given volume flow rate, increasing burner surface area would be expected to foster decreased surface temperature. However, as a function of combustion intensity, the surface temperature did not change with changes in the assigned value of surface area in the program; both ordinate and abscissa had cancelling surface area contributions.

Figure 25: Intensity of the CH_4 peak (AMU number 16) as a function of position away from the burner base for various combustion intensities. The zero position for the Krieger burner corresponded to the location of the flame retention plate.

Figure 26: Irradiation as a function detector angle from the burner surface, for various burners and apertures (7 or 15°). The y-axis "Radiosity" annotation is valid for diffuse emitters.

Figure 27: CO analyses for various burners as a function of mixture. Values were normalized to 3% oxygen. Combustion intensities in kW/m^2: Krieger: 220, Acotech: 220, Solaronics: 215.

The theoretical maximum efficiency model for a burner with a flame support layer indicates that the presence of a flame support layer increases the theoretical maximum efficiency. Qualitatively, the flame support layer provides a second surface to draw heat from the exhaust combustion product stream. This results in lower sensible heat lost as exhaust to the ambient, therefore increasing radiant efficiency. Conceivably, another downstream screen could make a further analogous contribution. However, each screen, or increased blocking area on a single screen, fosters higher base temperatures, which in turn would reach the degradation limit of many practical burner materials. Clearly, the higher the emittance of the base and screen materials, the higher their efficiency and the lower their temperatures. Note that as the screen area fraction diminishes, e.g. $f \rightarrow 0$, equation 4 defaults to equation 1, as would be expected.

It at first appears unintuitive that efficiency increases with increasing f; the base and flame support layer temperatures increase, hence their corresponding exiting combustion product temperatures would increase, which then would mean that the exhausted combustion product enthalpies would increase. However, with increasing f, the fraction of convection loss from the flame support layer increases. Since the temperature of the flame support layer is significantly lower than the base (Figure 13), a net decrease in combustion product heat loss results.

The experimental results might imply that entrainment of atmospheric air motivated rich mixtures to demonstrate maximum radiosity. This, however, is not our interpretation. Mass flow controllers are considered to be a highly accurate means of measuring and controlling gas flow; however, the manufacturer indicates that the devices are accurate to within $\pm 1\%$ of full scale. On that basis, maximum errors in mixture are shown in Figure 28. At low flow rates, significant errors in mixture are possible. Thus, it is not surprising for the measured maxima in radiosity and efficiency to be offset from indicated stoichiometric combustion (0% excess gas) as in Figures 17–20. The maxima for the Marsden burner more closely approached indicated stoichiometric combustion, since the output of the mass flow controllers was much closer to full scale. The onset of the precipitous increase in CO content (Figure 27) was close to the mixtures of maximum radiosity. These data clearly imply that the maximum in radiosity did not correspond to the indicated rich mixtures, but rather corresponded to true stoichiometric combustion. Hence, entrainment of atmospheric air into the combustion process is not considered

Figure 28: Maximum error in mixture based on a $\pm 1\%$ of full scale error, offset to opposite extremes for gas and air flow respectively. Vertical dashed lines indicate the range of flow for all burners with the exception of the Marsden burner.

significant.

In the mixture studies (Figure 17), radiosity showed a steady increase when increasing excess gas from the lean side. This was expected; with an abundance of air, increasing gas content increased the combustion intensity. Starting at the maximum in radiosity and continuing to increase the percent excess gas, the overabundance of gas did not increase the radiosity, since available oxygen for combustion (local to solid surfaces) was fixed. The slight decrease in radiosity in this range of excess gas can be attributed to the increased the volume flow rate (from increased natural gas flow) of room temperature mixture, with no extra combustion heat, thus decreasing the solid surface temperature. Lower values of radiosity were measured from the lean-to-rich study as compared to rich-to-lean. These minor shifts were manifestations of thermal lag; the burner always started at a colder state in each step in mixture going from lean to rich, while it came from a hotter state in each step in the other direction.

The maxima in radiosity were shifted to higher percent excess gas than the maxima in efficiency (compare Figures 19 and 20). Decreasing percent excess gas acted to increase the calculated value of efficiency since combustion intensity is in the denominator. This influence tended to flatten, and shift to lower percent excess gas, the efficiency maxima as compared to the radiosity maxima. The maxima in efficiency were chosen to be the fixed mixtures used for combustion intensity studies, rather than the maxima in radiosity, since efficiency optimization was the central focus of the investigation.

A wide variation in efficiencies is shown in Figure 24. For all burners with the exception of Marsden and Acotech (without screen), a maxima in efficiency was apparent. Decreasing from high combustion intensity, the efficiency increased to a maximum as a greater fraction of the heat of combustion contributed to convection to the solid, relative to heat lost as exhausted combustion products. For decreasing combustion intensity past the maximum efficiency, Figure 25 clearly shows that the flame began to lift downstream of the radiating surfaces.

Based on Figure 24, burners with flame support layers had significantly higher efficiencies. This is most impressively clear when comparing the Acotech burner, with and without a stainless steel flame support layer[1]. The model showed that the flame support layer can function to remove heat from the exhaust stream and convert it into additional

[1] Since no effort was made to optimize screen characteristics, the potential output of this burner may be higher.

radiant energy. The flame support layer also back-radiates to the base surface where the exiting gas ignites. By keeping that surface at elevated temperature, it is postulated that combustion goes to completion within a thin skin layer, fostering efficient convective heat transfer of the heat of combustion to the base surface. Without the flame support layer, the base layer would not be as hot, so a greater fraction of combustion would occur at downstream locations, where there are no solids to convect to. The flame support layer also functions as a blocking surface, forcing turbulent flow, also improving convective heat transfer to the base. The much lower value of combustion intensity at the maximum in efficiency for the Solaronics burner, as compared to the Hi-Tech burner, implies that the Kanthal screen flame support layer of the former is more effective at keeping the base layer hot at lower flow rates[2].

In the high combustion intensity range, the non-perforated Acotech burner showed higher efficiency than its perforated counterpart, since the high upstream pressure forced a greater fraction of combustible mixture through the holes, so that convection to the entirety of the downstream surface was less efficient. The Krieger burner showed a comparatively lower sensitivity of efficiency to varying combustion intensity. For this burner, convection heat transfer is more forced than the other designs, so increasing combustion intensity did not result in as significant a fraction of heat loss to the exhaust combustion product stream. The Krieger burner did not achieve the ultimate efficiency reached by the Solaronics burner; the internal-heating design of the burner fosters significant temperature rise in the burner housing[14]. This in turn contributed additional heat losses which may have affected the ultimate efficiency of the burner.

The theoretical limit for the Marsden and Acotech (without front metal screen) burners is the $f = 0$ case (Figure 24). For the Solaronics and Krieger burners, the theoretical maximum efficiencies are the $f = 0.56$ and $f = 0.66$ cases, respectively. It is apparent that there is appreciable room for improvement of all burners; that is, the actual burners do not behave in accordance with the assumptions made in the model. These involve non-blackbody surface emittances, imperfect convection between combustion products and solid surfaces (temperatures do not become equal), and entrainment of atmospheric air between the base and flame support layer. Further, the true convective surface area of base and flame support layer are not reflected by the model: The base contains capillaries for

[2] Other flame support layer densities are manufactured by Hi-Tech, which may demonstrate different behavior.

the emergence of gas/air mixture, which will form low temperature spots on the surface. On the other hand, the rough-textured bases would have a higher convective/radiative surface area than determined simply from its hot dimensions (which were the values used in determination of combustion intensity).

Using a single-location measurement, the calculation of radiosity, and from it, efficiency, is correct only if the diffuse emitter assumption is valid for these burners. As clearly indicated from Figure 26, the diffuse emitter assumption is validated to the resolution limit of the radiometer used. Perfectly smooth dielectrics should have a decreasing radiant flux with angle from the surface normal due to increased internal reflection. Smooth metal surfaces show and increase, followed by a drop-off in radiant flux with angle[15]. However, since all burner faces were far from smooth, random local surface orientations annihilated such effects, and the burners behaved as diffuse emitters. It clearly was not possible to fill the field of view of the 15° aperture at the most oblique angles. The slight increase in radiosity with angles shifting away from orthogonal can be attributed to decreased water vapor absorption of radiation[14].

6 CONCLUSIONS

Radiant efficiencies were determined from measurements from a (blackbody cavity) calibrated total radiation pyrometer, and mass flow controllers for gas and air flow. To ensure that each burner's efficiency characteristics were properly represented, the gas/air mixture of maximum efficiency was first determined for each burner, thereby correcting for any inaccuracies in measurements from mass flow controllers. Combustion intensity studies then followed using the determined mixtures. The more efficient burners demonstrated a maximum in efficiency with combustion intensity, where at combustion intensities below the maximum, the flame began to lift downstream of the solid surfaces. The Solaronics burner showed the highest measured efficiency of 53.9% at 188.5 kW/m^2. The Krieger burner showed consistently high efficiencies and the least variation with combustion intensity; the direct impingement of hot combustion products on the flame retention plate fostered effectual convective heat transfer to the solid surfaces. The merits of a flame support layer were clearly demonstrated by an increase in efficiency from 28.4% to 38.8% for the Acotech burner when a stainless steel flame support layer was used.

7 ACKNOWLEDGEMENTS

We would like to express our appreciation to Messrs. Chris Vallencourt from Krieger Corp., Truett Sweeting from Hi-Tech Ceramics, Thierrry Delfosse from Solaronics Corp., and Willy Marrecau from Bekaert Corp. (Acotech), for providing us with burners, and for helpful discussions. The authors acknowledge project managers Dr. Kevin Krist of the Gas Research Institute and Mr. Shyam Singh of SSEEI, Inc., for funding this investigation. This manuscript was prepared by the Georgia Institute of Technology as an account of work sponsored by the Gas Research Institute. Neither GRI, members of GRI, nor any person acting on behalf of either; A. Makes any warranty or representation, expressed or implied, with respect to the accuracy, completeness, or usefulness of the information contained in this manuscript, or that the use of any information, apparatus, method, or process disclosed in this manuscript may not infringe on privately-owned rights, or B. Assumes any liability with respect to the use of, or for damages resulting from the use of, any information, apparatus, method, or process disclosed in this manuscript.

8 APPENDIX

The view factor F_{ij} is defined as the fraction of the radiation leaving surface i, which is intercepted by surface j. With terms as defined in Figure 29a, the view factor is determined by:[10]

$$F_{ij} = \frac{1}{A_i} \int_{A_i} \int_{A_j} \frac{\cos\theta_i \cos\theta_j}{\pi x^2} dA_i dA_j$$

If the radiating and intercepting planes are parallel: $\theta_i, \theta_j = 0$, and

$$F_{ij} = \frac{A_j}{\pi x^2}$$

Heat transfer from i to j is then:

$$q_{ij} = A_i F_{ij} \sigma \left(T_i^4 - T_j^4\right) = \frac{A_i A_j}{\pi x^2} \sigma \left(T_i^4 - T_j^4\right)$$

Figure 29b can be visualized to indicate a detector at a distance x_1 from the radiating surface, with a view restriction angle θ_r, resulting in a view radius r_1 on the radiating surface. If the distance between the radiating surface and the detector is extended to x_2, the view radius changes to r_2. Since the view restriction angle remains constant,

Figure 29: a) View factor associated with radiation exchange between elemental surfaces of area dA_i and dA_j. b) Viewed area as a restricted-view detector is drawn away from a radiating surface.

$x_1 r_2 = r_1 x_2$ by similar triangles. Comparing heat flows:

$$q_{ij_1} = \frac{4\pi {r_1}^2}{\pi {x_1}^2} A_j \sigma \left(T_i^4 - T_j^4\right) = \frac{4\pi {r_2}^2}{\pi {x_2}^2} A_j \sigma \left(T_i^4 - T_j^4\right) = q_{ij_2}$$

Thus, changing the position of the detector does not change the radiant power incident on it.

References

[1] M. Golombok, A. Prothereo, L. C. Shrivill, and L. M. Small, "Surface Combustion in Metal Fibre Burners", *Combust. Sci. and Tech.* vol. 77, pp. 203-223, 1991.

[2] F. Andersen, "Heat Transport Model for Fibre Burners", *Prog. Energy Combust. Sci.*, vol. 18, pp. 1-12, 1992.

[3] Y.-K. Chen, R. D. Matthews, J. R. Howell, "The Effect of Radiation on the Structure of Premixed Flame Within a Highly Porous Inert Medium", *Radiation, Phase Change Heat Transfer, and Thermal Systems*, ASME HTD, vol., 81, pp. 35-41, 1987.

[4] L. B. Younis and R. Viskanta, "Experimental Determination of the Volumetric Heat Transfer Coefficient Between Stream of Air and Ceramic Foam", *Int. J. Heat Mass Transfer*, vol. 36, no. 6, pp. 1425-1434, 1993.

[5] C. Chaffin, M. Koenig, M. Koeroghlian, R. D. Matthews, M. J. Hall, S. P. Nichols, and I-G. Lim, "Experimental Investigation of Premixed Combustion within Highly Porous Media", *ASME/JSME Thermal Engineering Proceedings*, vol. 4, pp. 219-224, 1991.

[6] P. Hsu, J. R. Howell, and R. D. Matthews, "A Numerical Investigation of Premixed Combustion Within Porous Inert Media", *ASME/JSME Thermal Engineering Proceedings*, vol. 4, pp. 225-231, 1991.

[7] T. Xiong, R. Viskanta, "A Basic Study of a Porous-matrix Combustor-heater", *Fossil Fuels Combustion*, PD-vol. 39, pp. 31-39, 1992.

[8] R. F. Speyer, W. Lin, and G. Agarwal, "Performance Evaluation of Porous Radiant Gas Burners", *Journal of Experimental Heat Transfer*, vol. 8, no. 1, pp. 73-95, 1995.

[9] R. C. Weast, ed., CRC Handbook of Chemistry and Physics, 58th edition, CRC Press, Inc, Cleveland, OH, 1978.

[10] R. Seigel and J. R. Howell, *Radiation Heat Transfer*, Hemisphere Publishing Corp, (1992).

[11] F. D. Incropera and D. P. DeWitt, *Fundamentals of Heat and Mass Transfer*, 2d ed, John Wiley and Sons, New York, 1985.

[12] R. J. Reed, *North American Combustion Handbook*, 3d ed., North American Mfg. Co., Cleveland, OH, 1986.

[13] M. W. Chase, Jr., C. A. Davies, J.R. Downey, Jr., D. J. Frurip, R. A. McDonald, and A. N. Syverud, "JANAF Thermochemical Tables, Third Edition", *Journal of Physical and Chemical Reference Data*, vol. 14, Supplement No. 1, 1985.

[14] R. F. Speyer, "Deconvolution of Superimposed DTA/DSC Peaks Using the Simplex Algorithm", *J. Mat. Res.*, 8 (3) 675-679 (1993).

[15] W. Lin, G. Agarwal, and R. F. Speyer, "Performance Considerations of Commercially Manufactured Gas Radiant Burners", unpublished work.

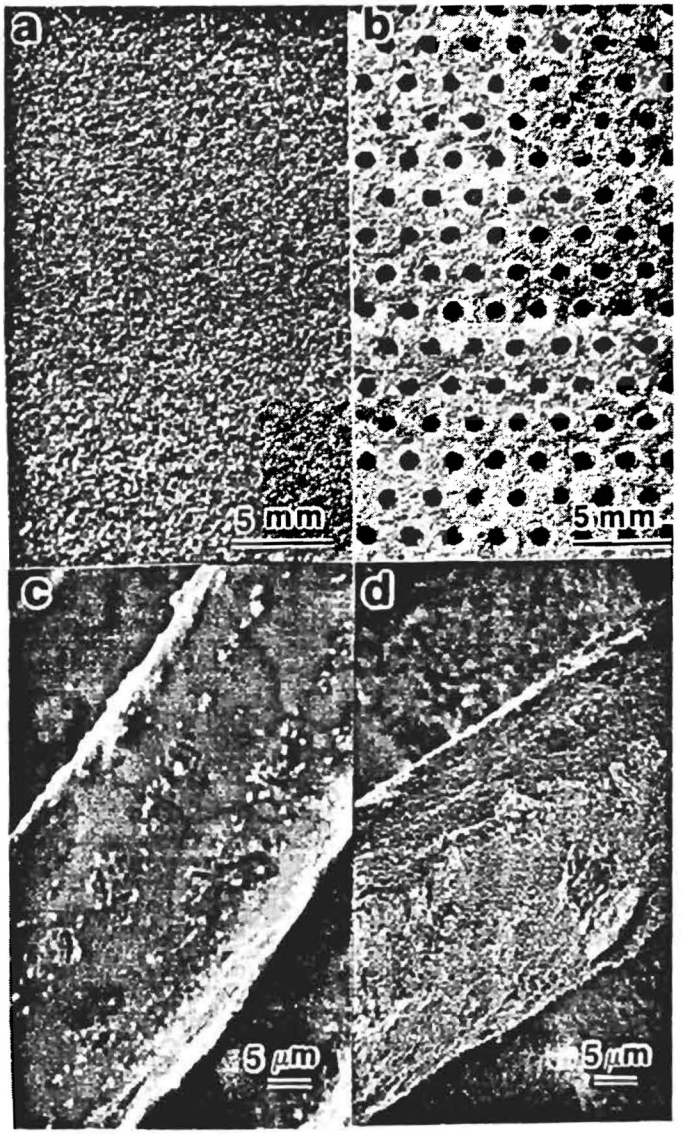
a
5 mm
b
5 mm
c
5 μm
d
5 μm

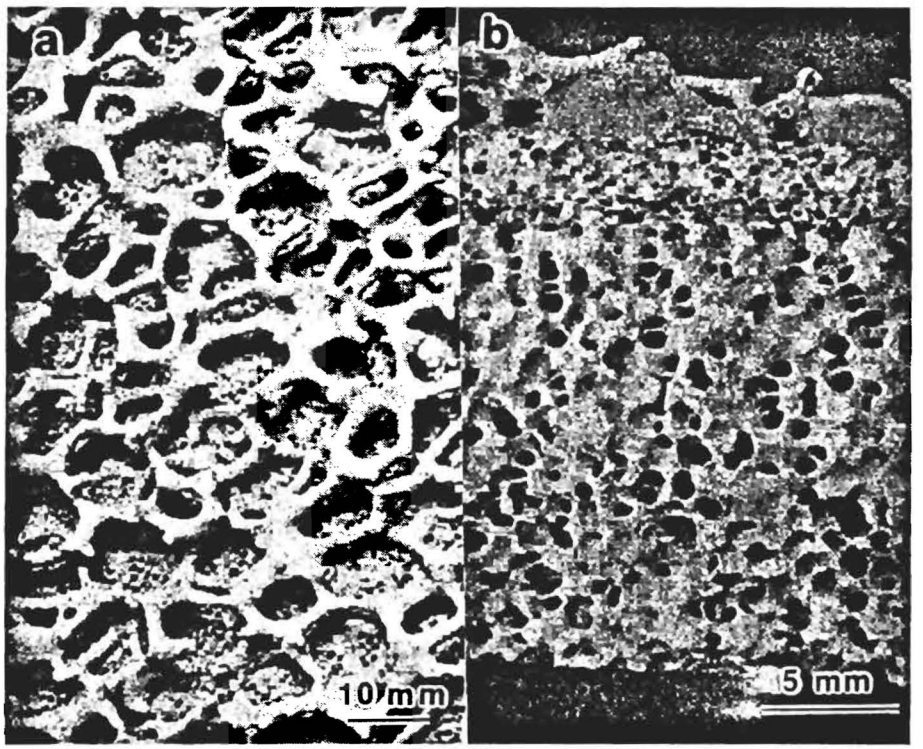
a
10 mm
b
5 mm

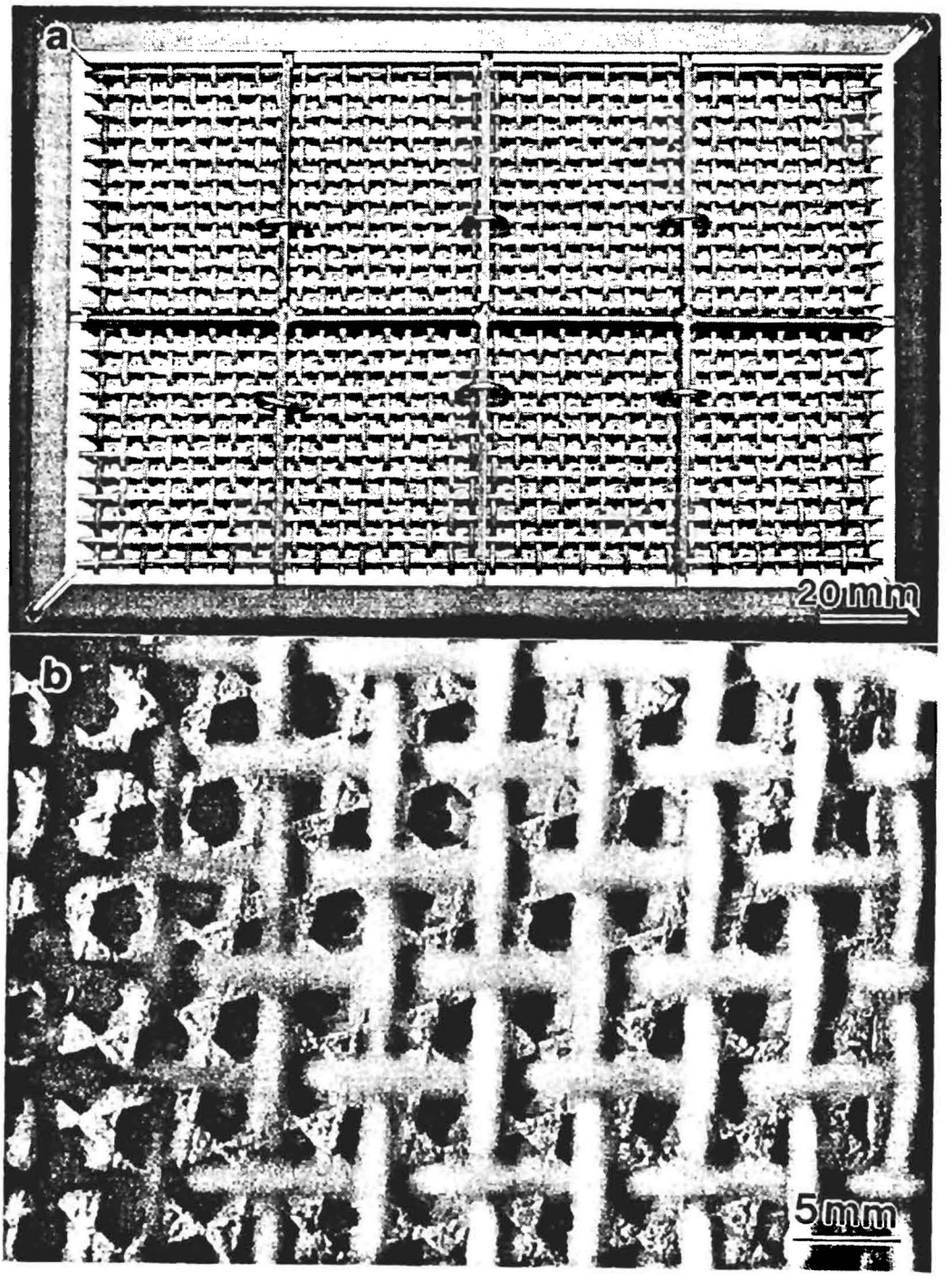
a
20mm
b
5mm

a

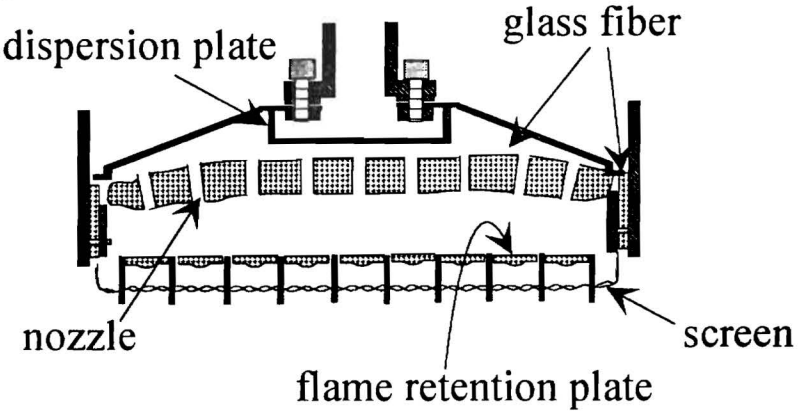
dispersion plate
glass fiber
nozzle
screen
flame retention plate

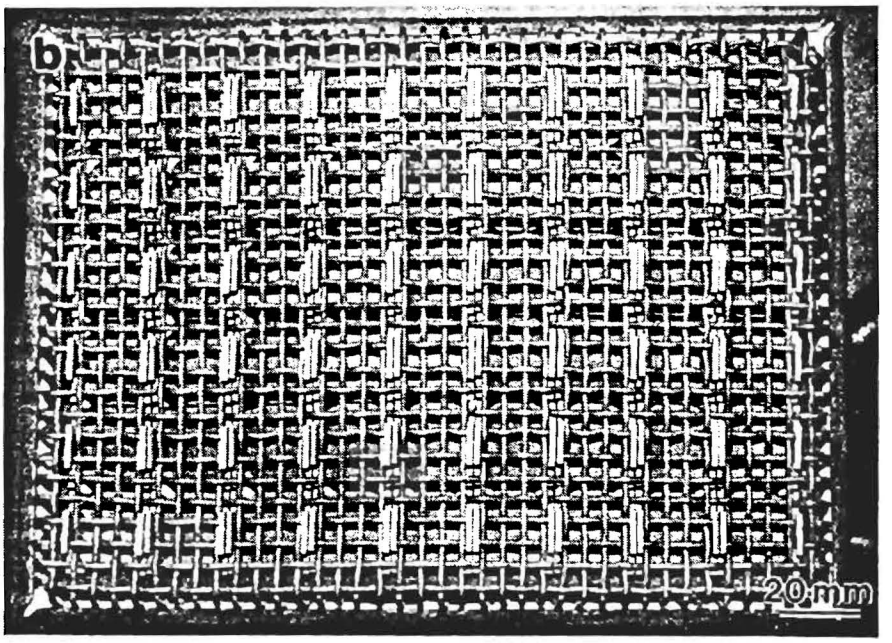
b
20 mm

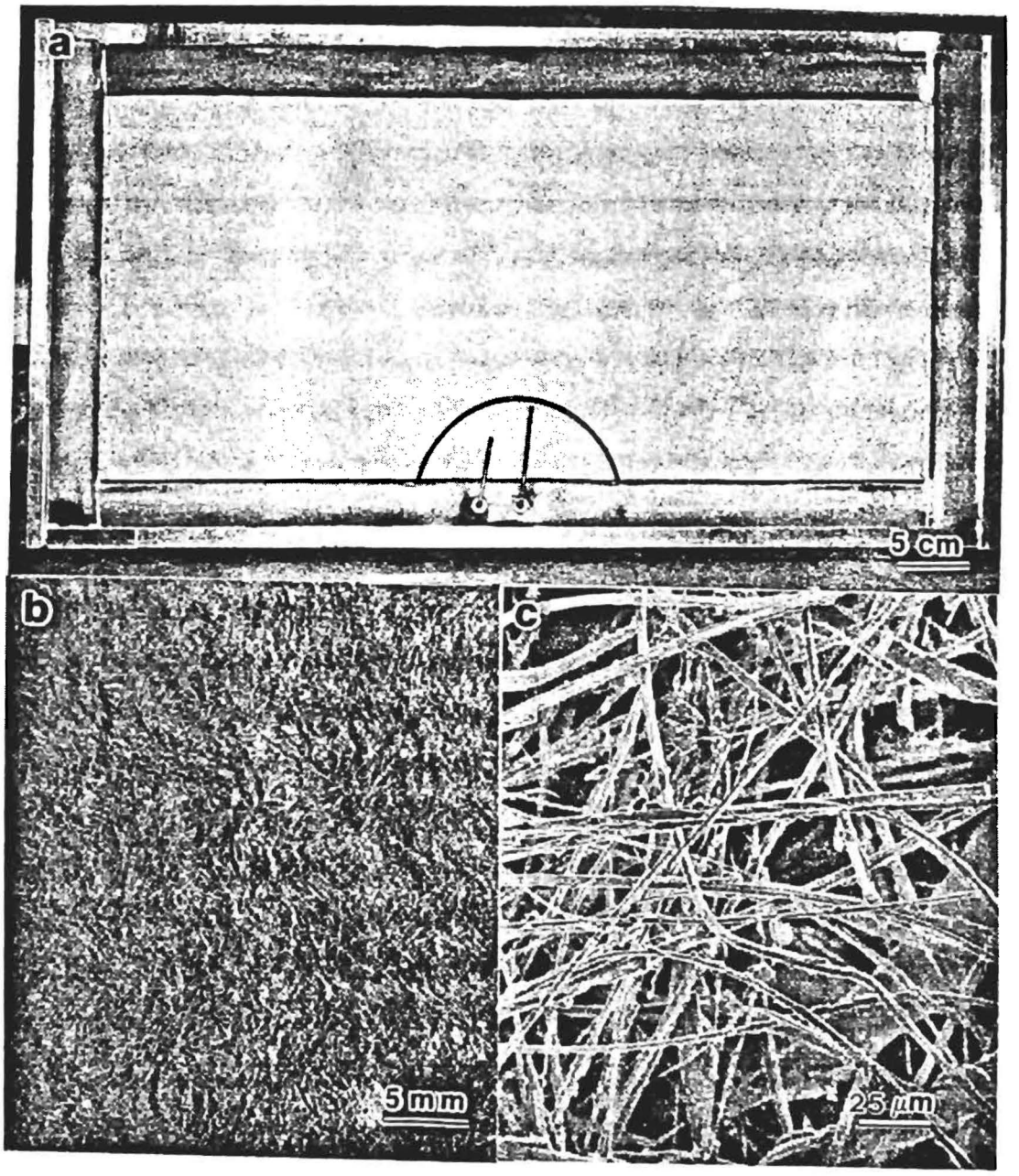
a
5 cm
b
5 mm
c
25 μm

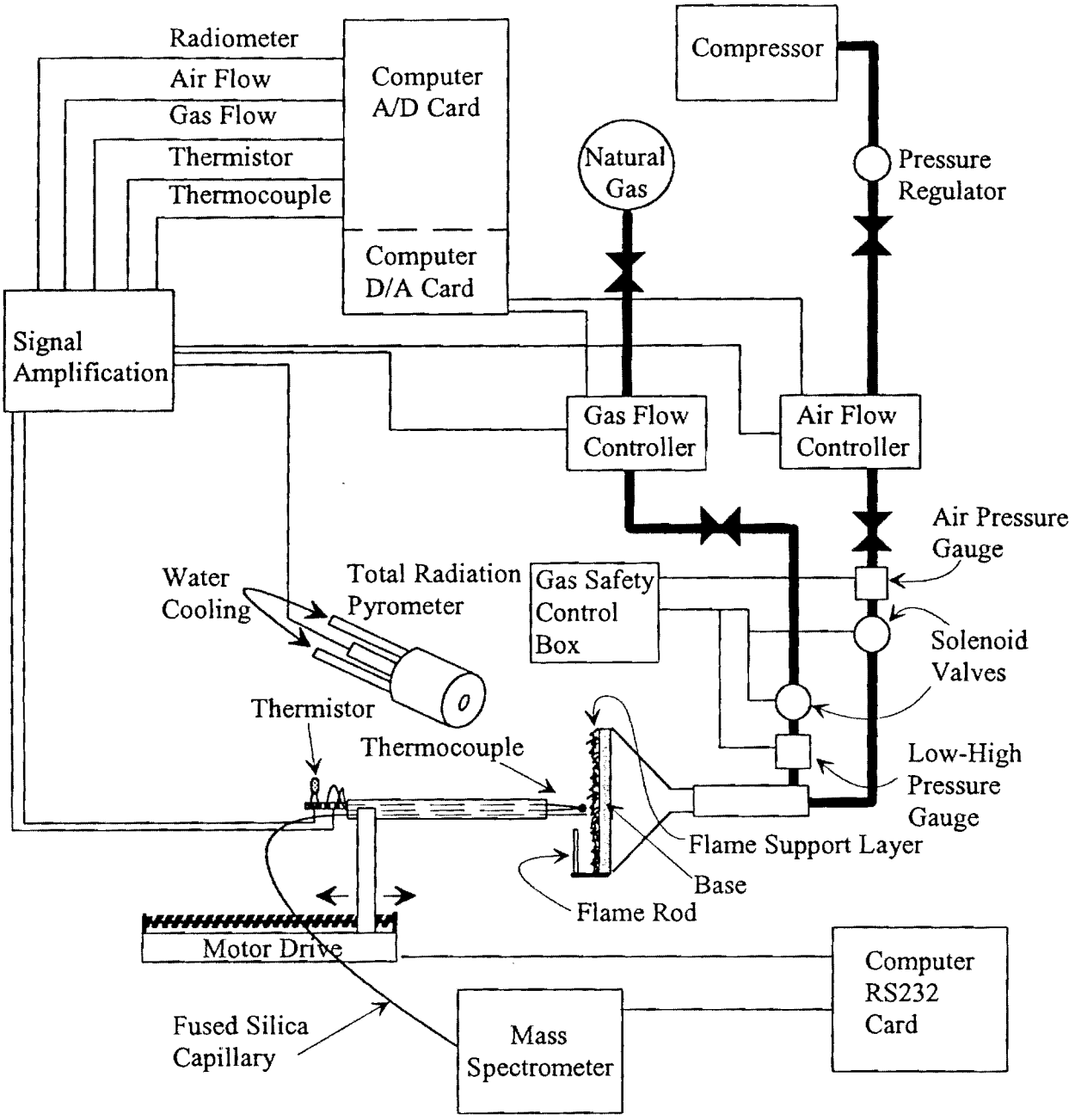
Radiometer
Air Flow
Gas Flow
Thermistor
Thermocouple
Computer A/D Card
Computer D/A Card
Compressor
Natural Gas
Pressure Regulator
Signal Amplification
Gas Flow Controller
Air Flow Controller
Air Pressure Gauge
Water Cooling
Total Radiation Pyrometer
Gas Safety Control Box
Solenoid Valves
Thermistor
Thermocouple
Low-High Pressure Gauge
Flame Support Layer
Base
Flame Rod
Motor Drive
Computer RS232 Card
Fused Silica Capillary
Mass Spectrometer

FIG 6

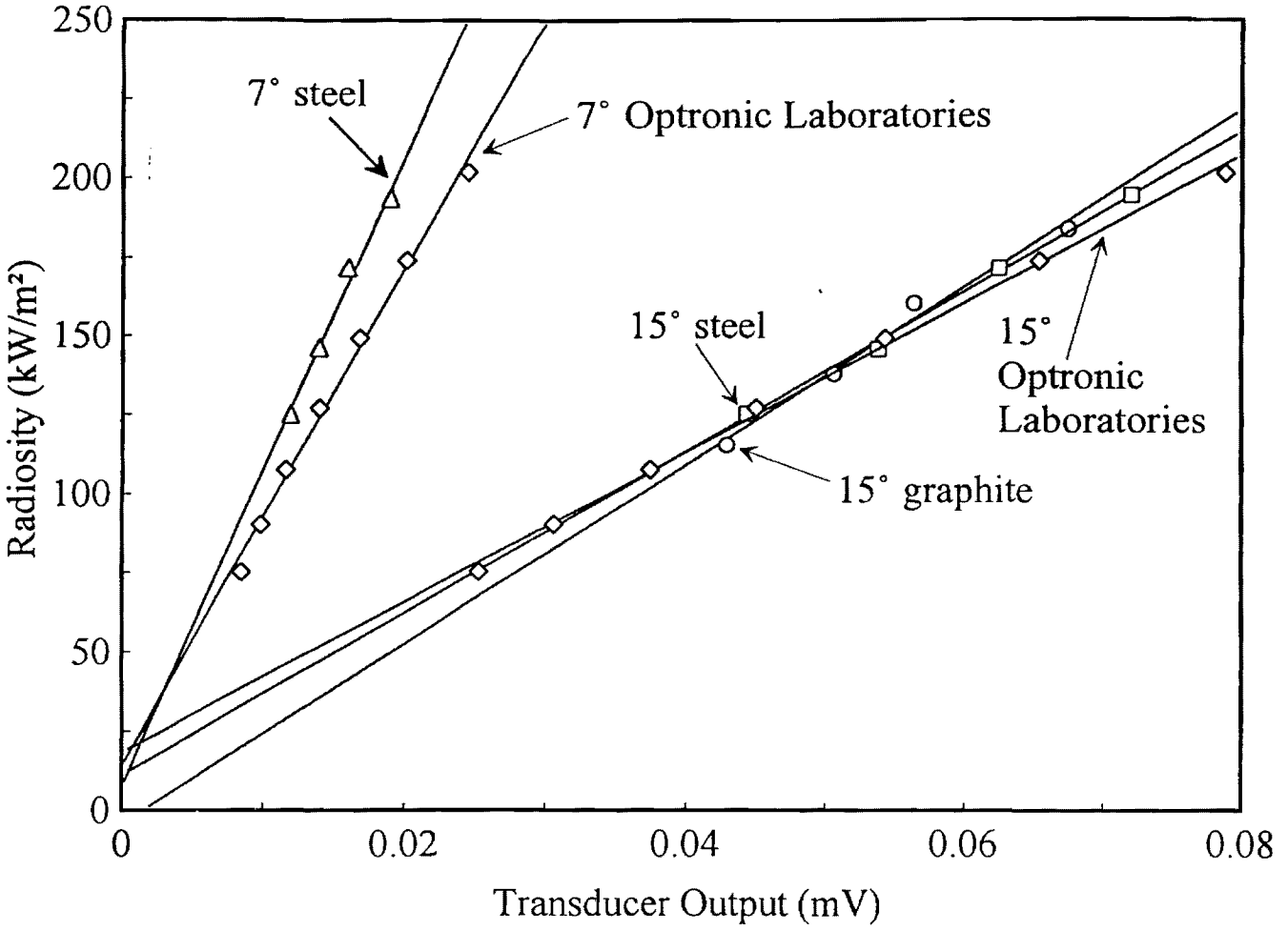
250
200
150
100
50
0
Radiosity (kW/m²)
0
0.02
0.04
0.06
0.08
Transducer Output (mV)
7° steel
7° Optronic Laboratories
15° steel
15° graphite
15° Optronic Laboratories

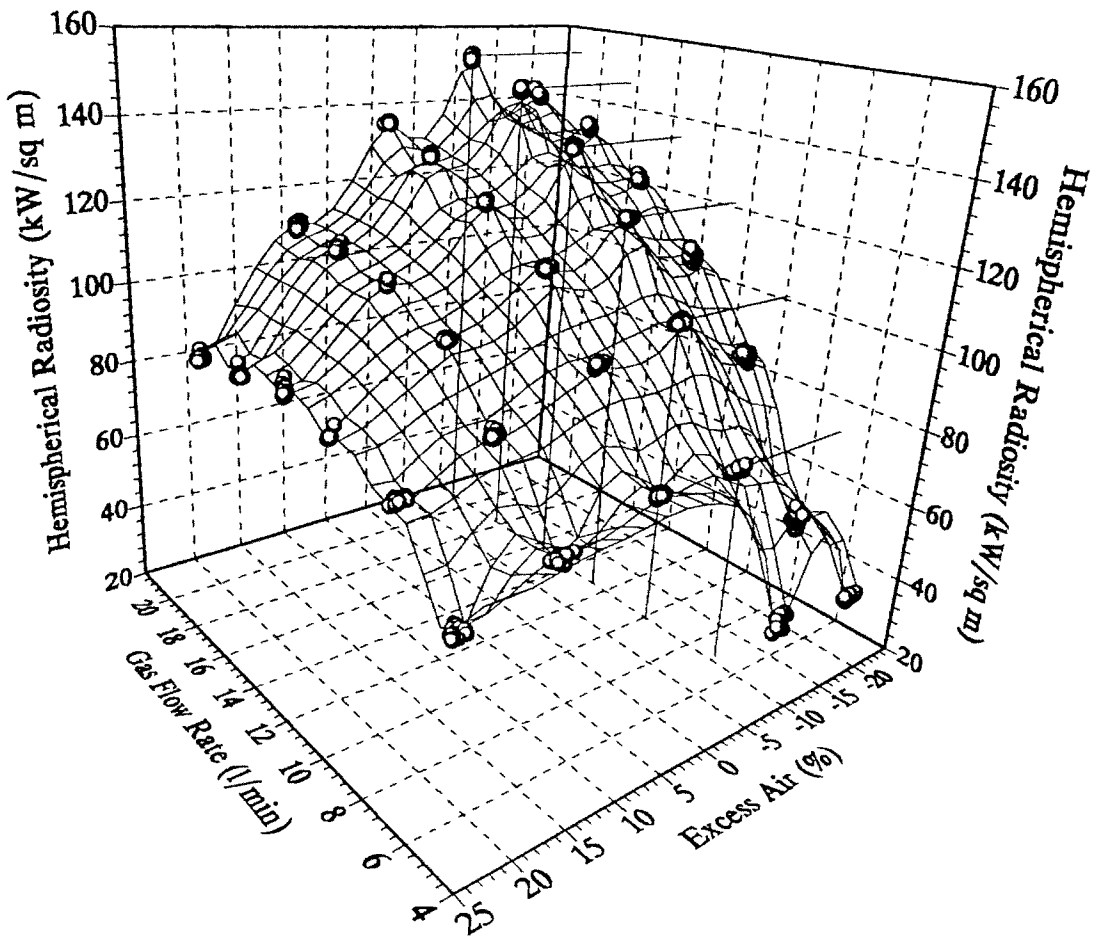
Hemispherical Radiosity (kW/sq m)
160
140
120
100
80
60
40
20
Gas Flow Rate (l/min)
20 18 16 14 12 10 8 6 4
Excess Air (%)
25 20 15 10 5 0 -5 -10 -15 -20
Hemispherical Radiosity (kW/sq m)
160
140
120
100
80
60
40
20

F16 8

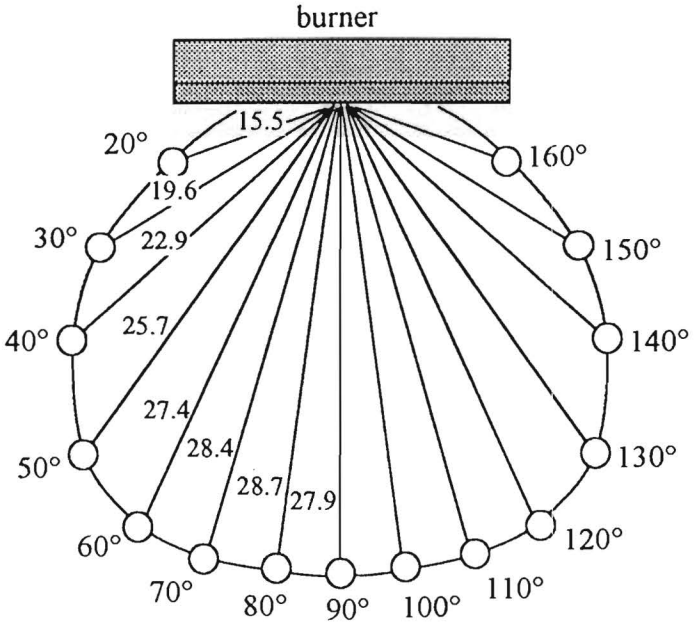
burner
15.5
20°
160°
19.6
30°
22.9
150°
40°
25.7
140°
27.4
28.4
50°
130°
28.7
27.9
60°
120°
70°
80°
90°
100°
110°

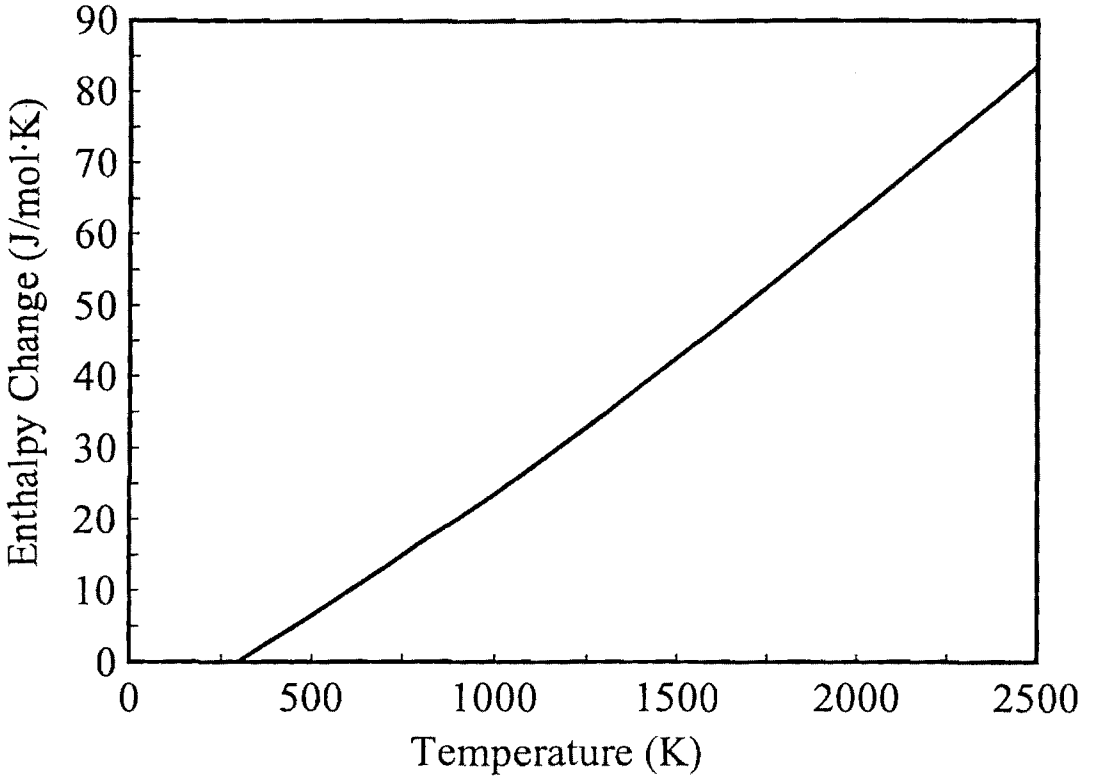
Enthalpy Change (J/mol·K)
90
80
70
60
50
40
30
20
10
0
0
500
1000
1500
2000
2500
Temperature (K)

FIG 10

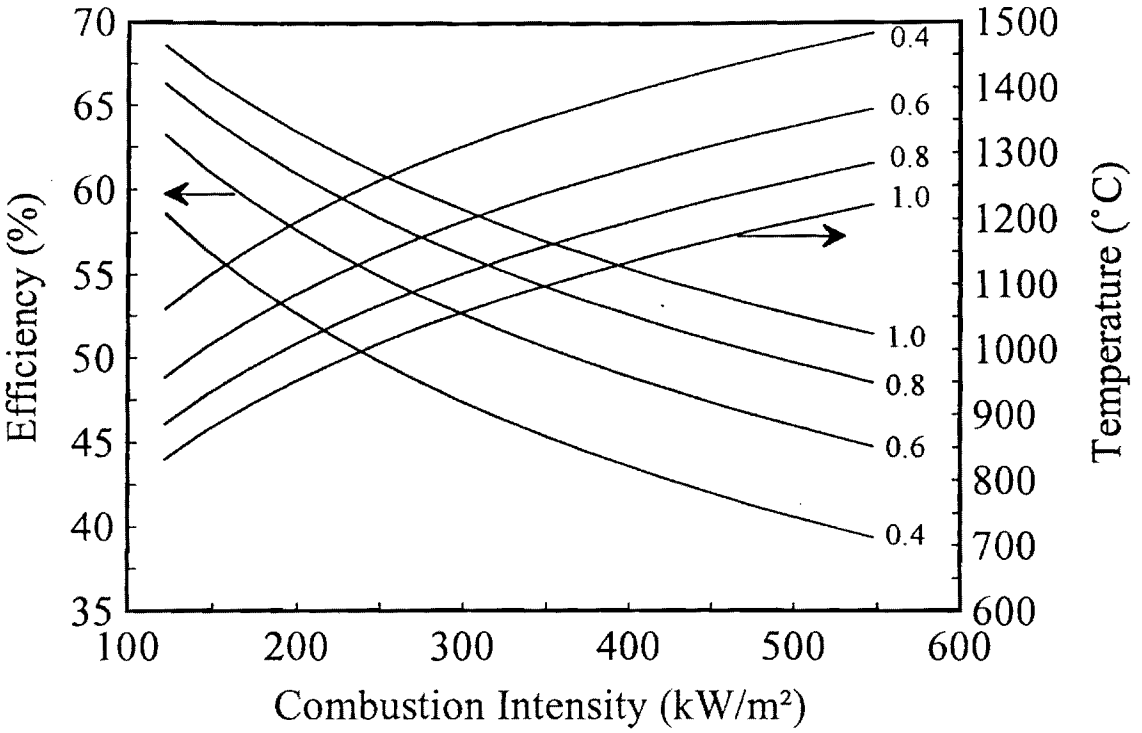
70
65
60
55
50
45
40
35
Efficiency (%)
1500
1400
1300
1200
1100
1000
900
800
700
600
Temperature (°C)
100
200
300
400
500
600
Combustion Intensity (kW/m²)
0.4
0.6
0.8
1.0
1.0
0.8
0.6
0.4

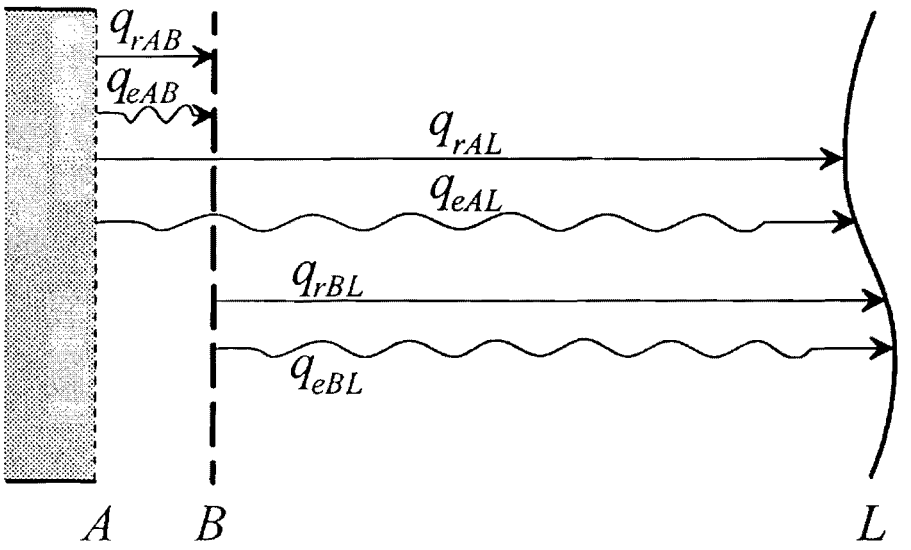
q_{rAB}
q_{eAB}
q_{rAL}
q_{eAL}
q_{rBL}
q_{eBL}
A
B
L

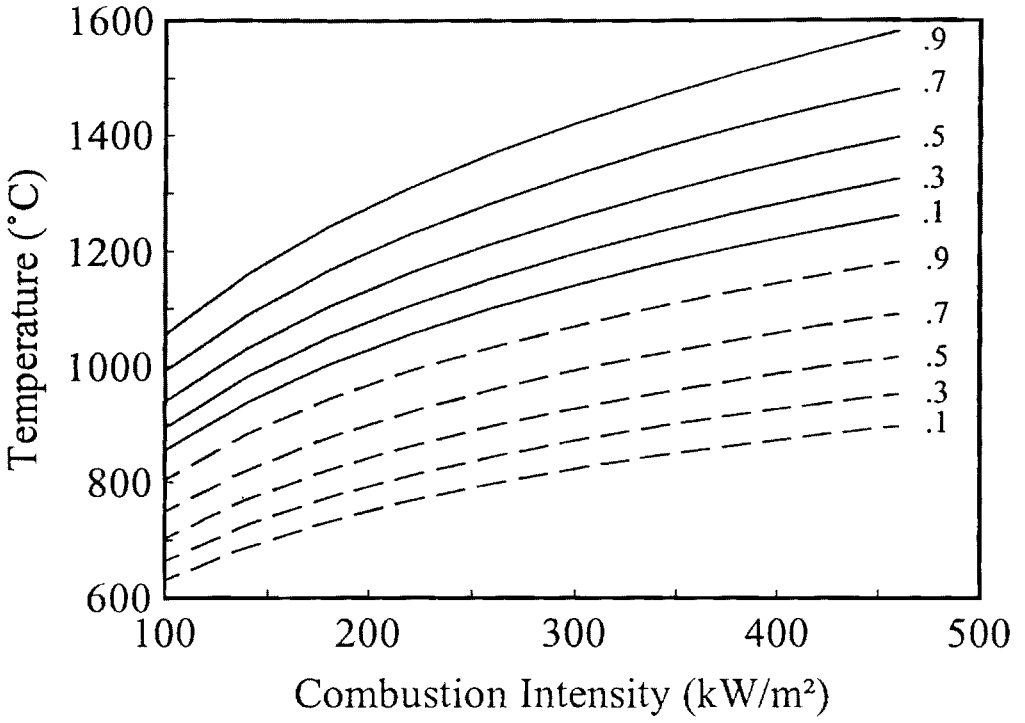

F16 13

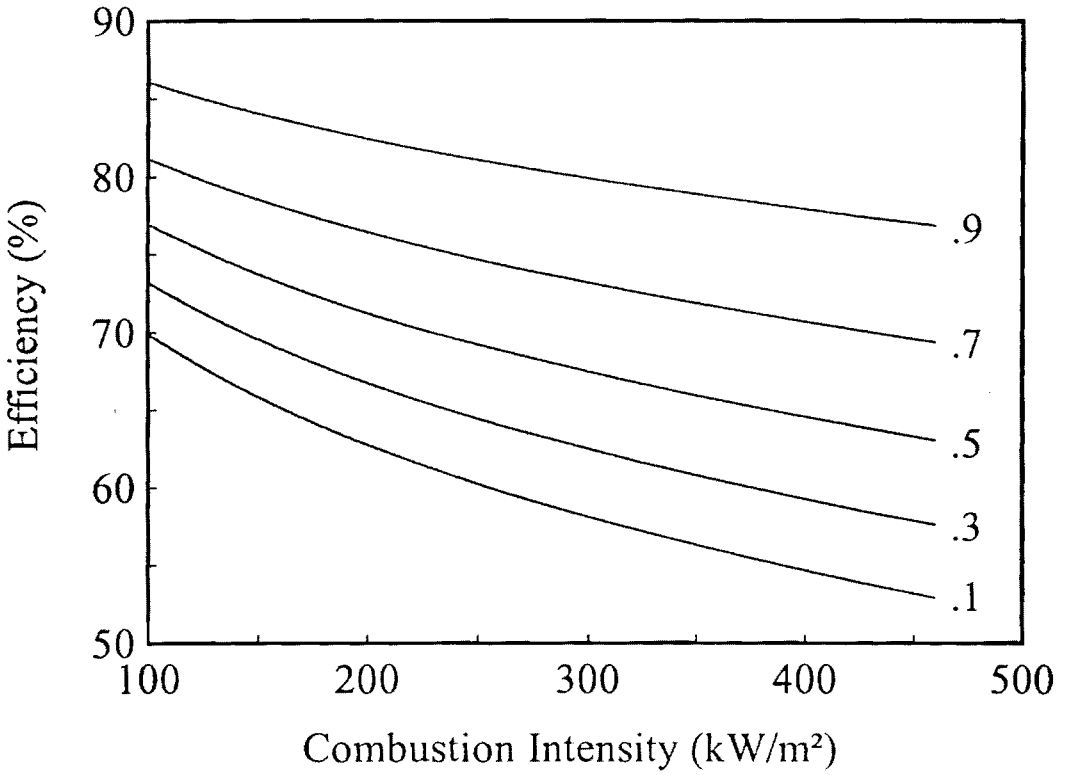

F16 14

$\epsilon = 0.3$

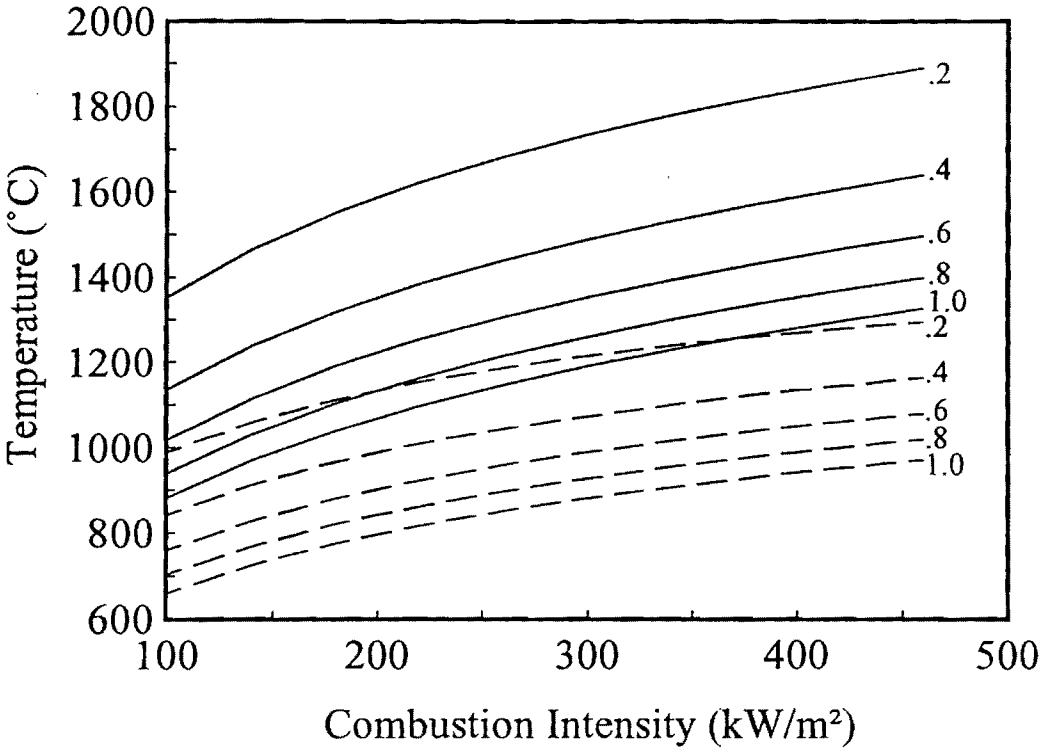

F16 15

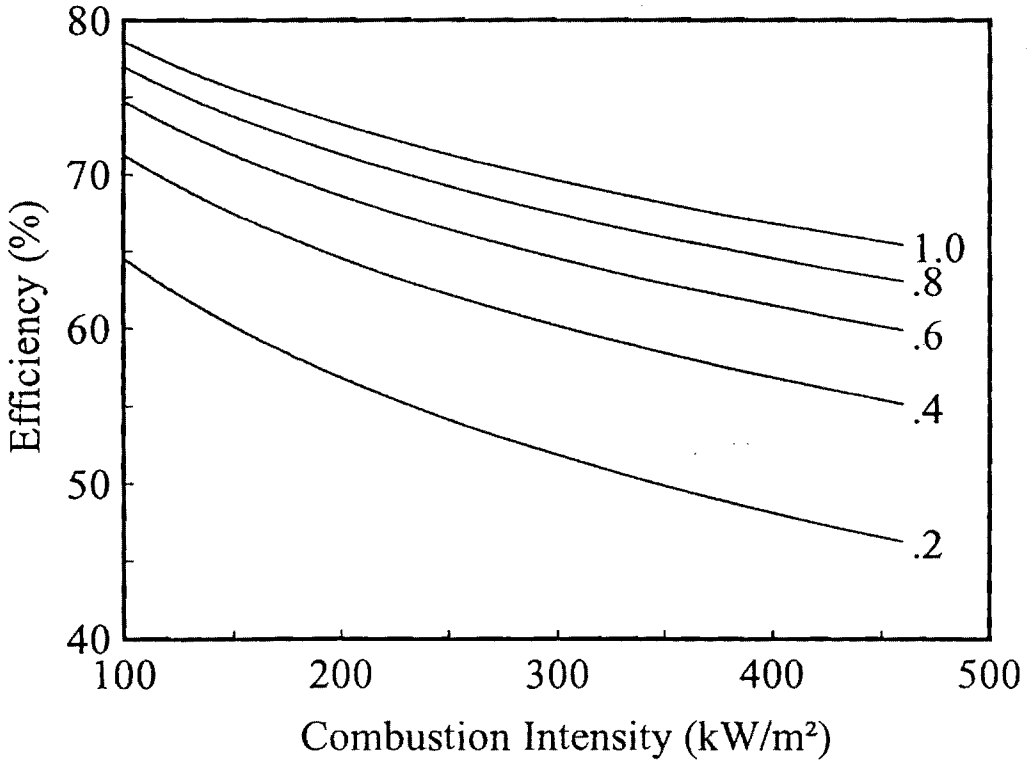

F16 16

$f = 0.5$

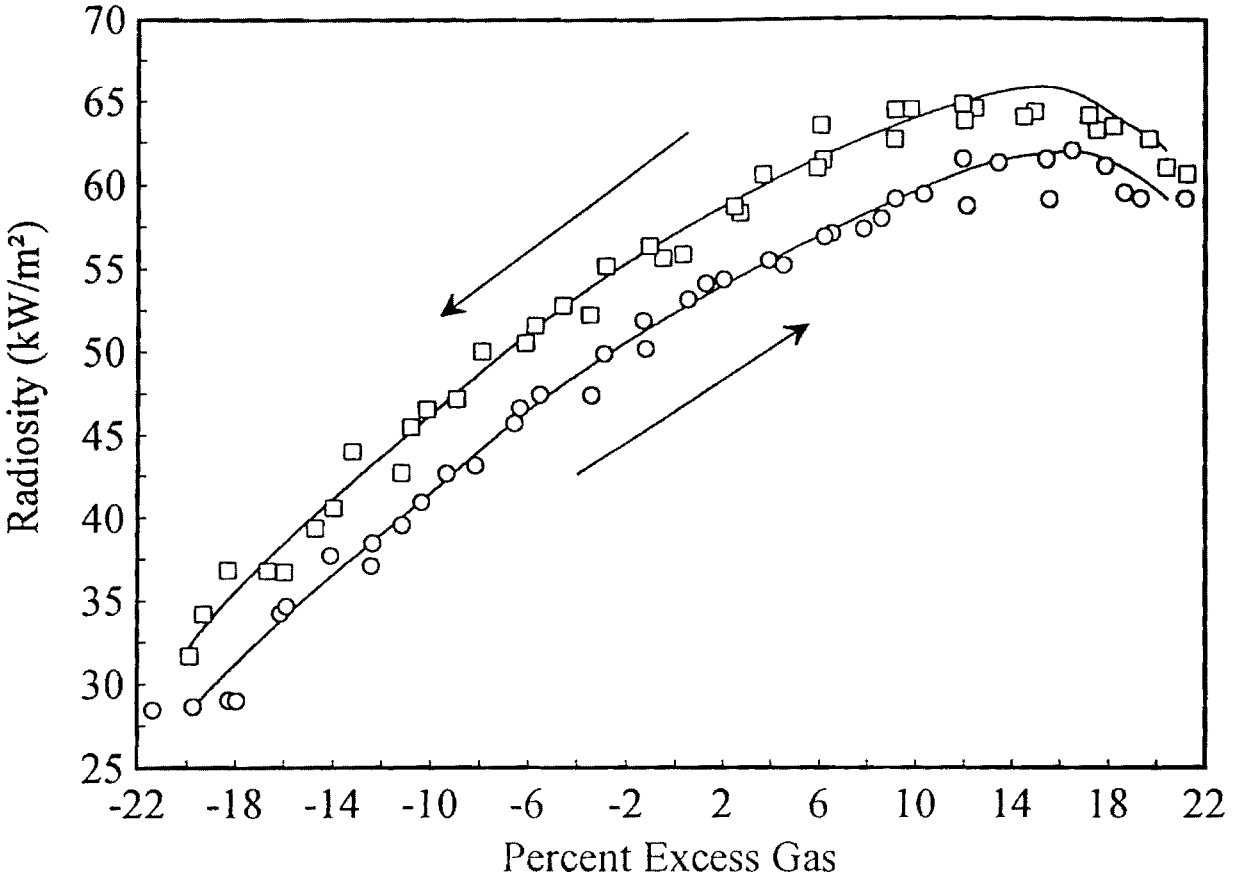
70
65
60
55
50
45
40
35
30
25
Radiosity (kW/m²)
-22
-18
-14
-10
-6
-2
2
6
10
14
18
22
Percent Excess Gas

FIG 17

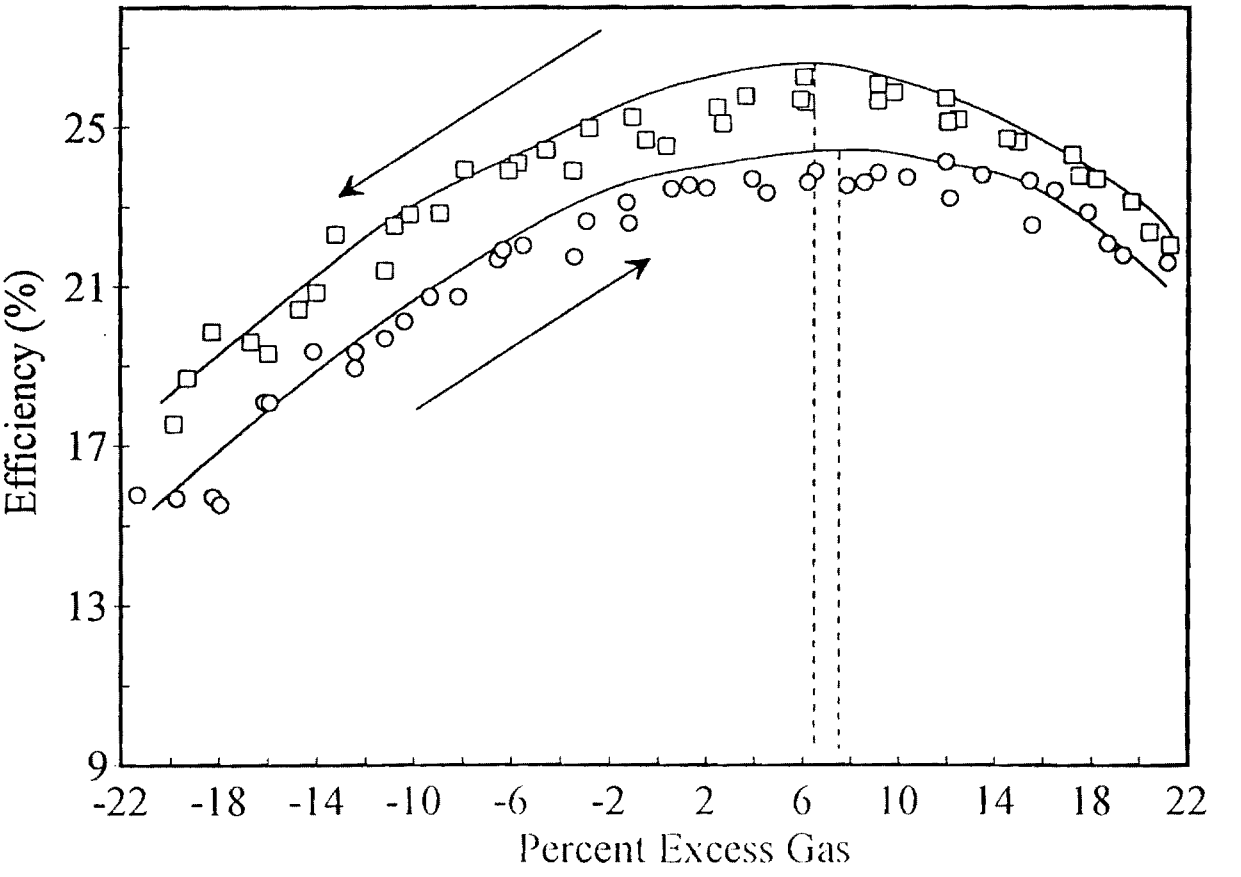
25
21
17
13
9
Efficiency (%)
-22
-18
-14
-10
-6
-2
2
6
10
14
18
22
Percent Excess Gas

FIG 18

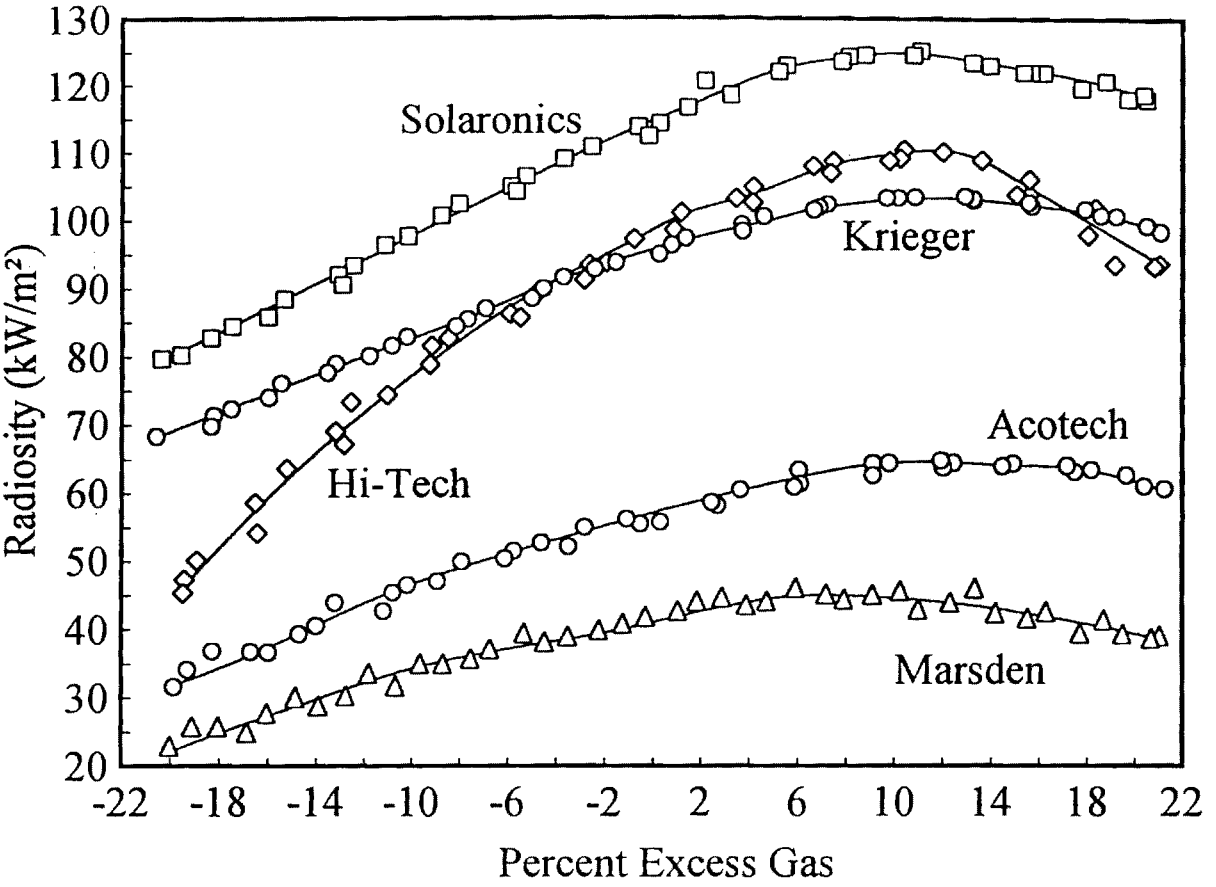
Radiosity (kW/m²)
130
120
110
100
90
80
70
60
50
40
30
20
-22
-18
-14
-10
-6
-2
2
6
10
14
18
22
Percent Excess Gas
Solaronics
Krieger
Acotech
Hi-Tech
Marsden

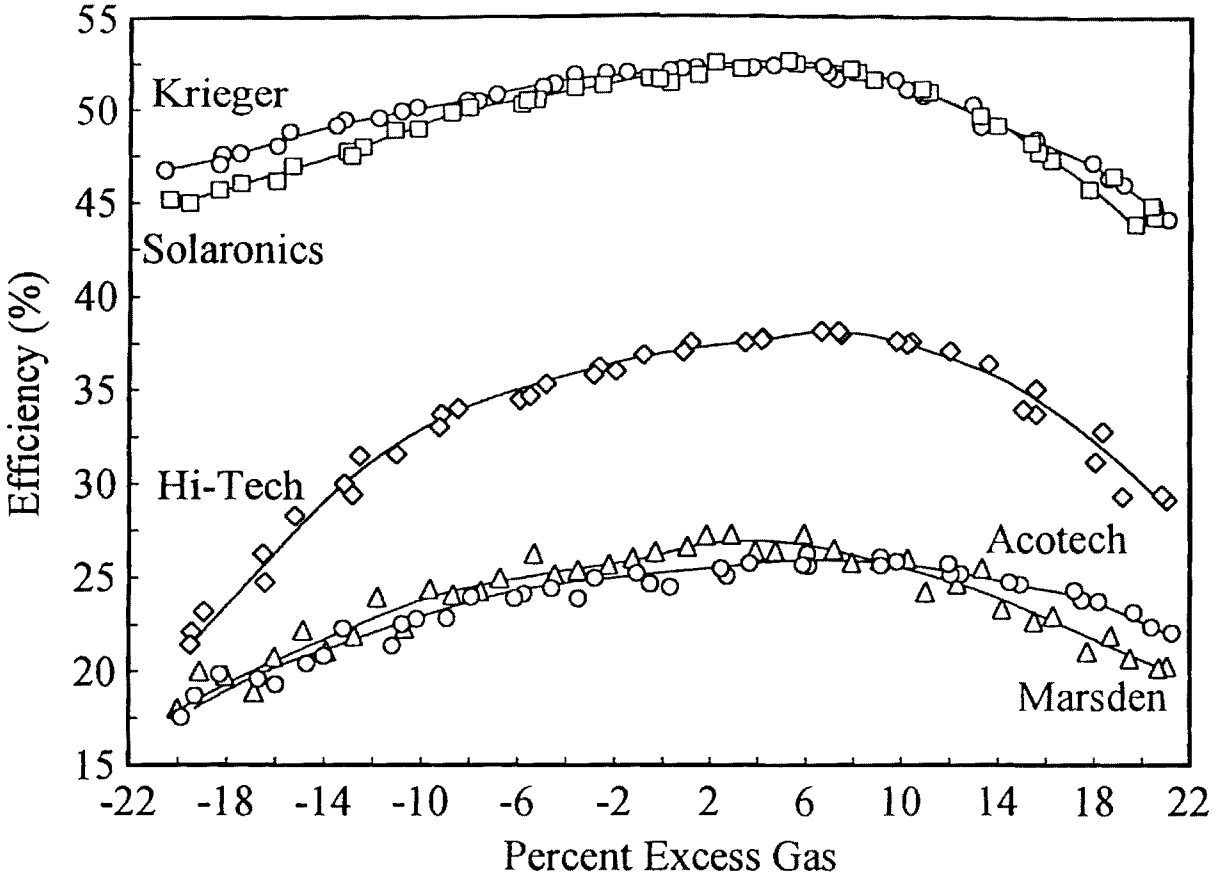
Krieger
Solaronics
Hi-Tech
Acotech
Marsden
Efficiency (%)
55
50
45
40
35
30
25
20
15
-22
-18
-14
-10
-6
-2
2
6
10
14
18
22
Percent Excess Gas

F16.20

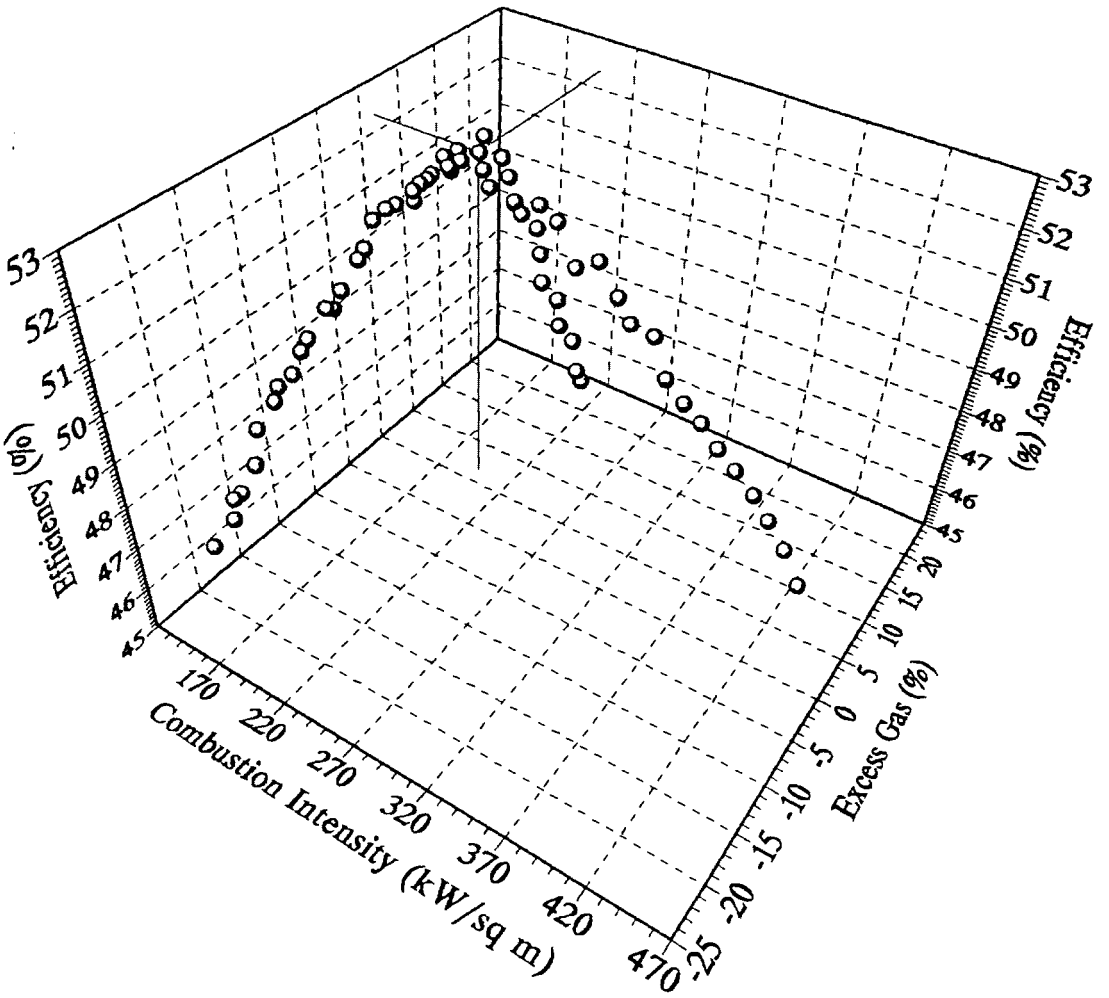
Efficiency (%)
53
52
51
50
49
48
47
46
45
Combustion Intensity (kW/sq m)
170
220
270
320
370
420
470
Excess Gas (%)
-25
-20
-15
-10
-5
0
5
10
15
20
Efficiency (%)
53
52
51
50
49
48
47
46
45

FIG 21

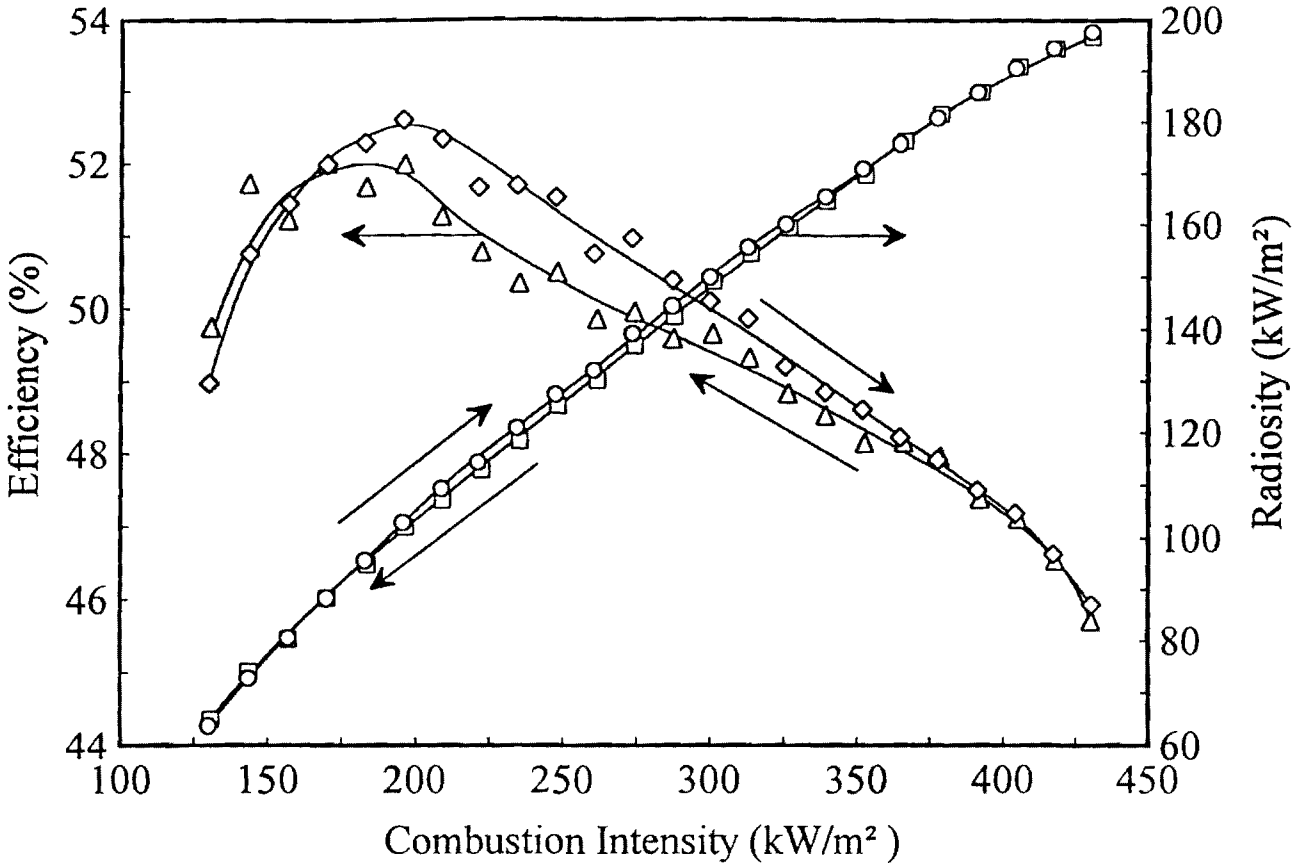
54
52
50
48
46
44
Efficiency (%)
200
180
160
140
120
100
80
60
Radiosity (kW/m²)
100
150
200
250
300
350
400
450
Combustion Intensity (kW/m²)

FIG. 3

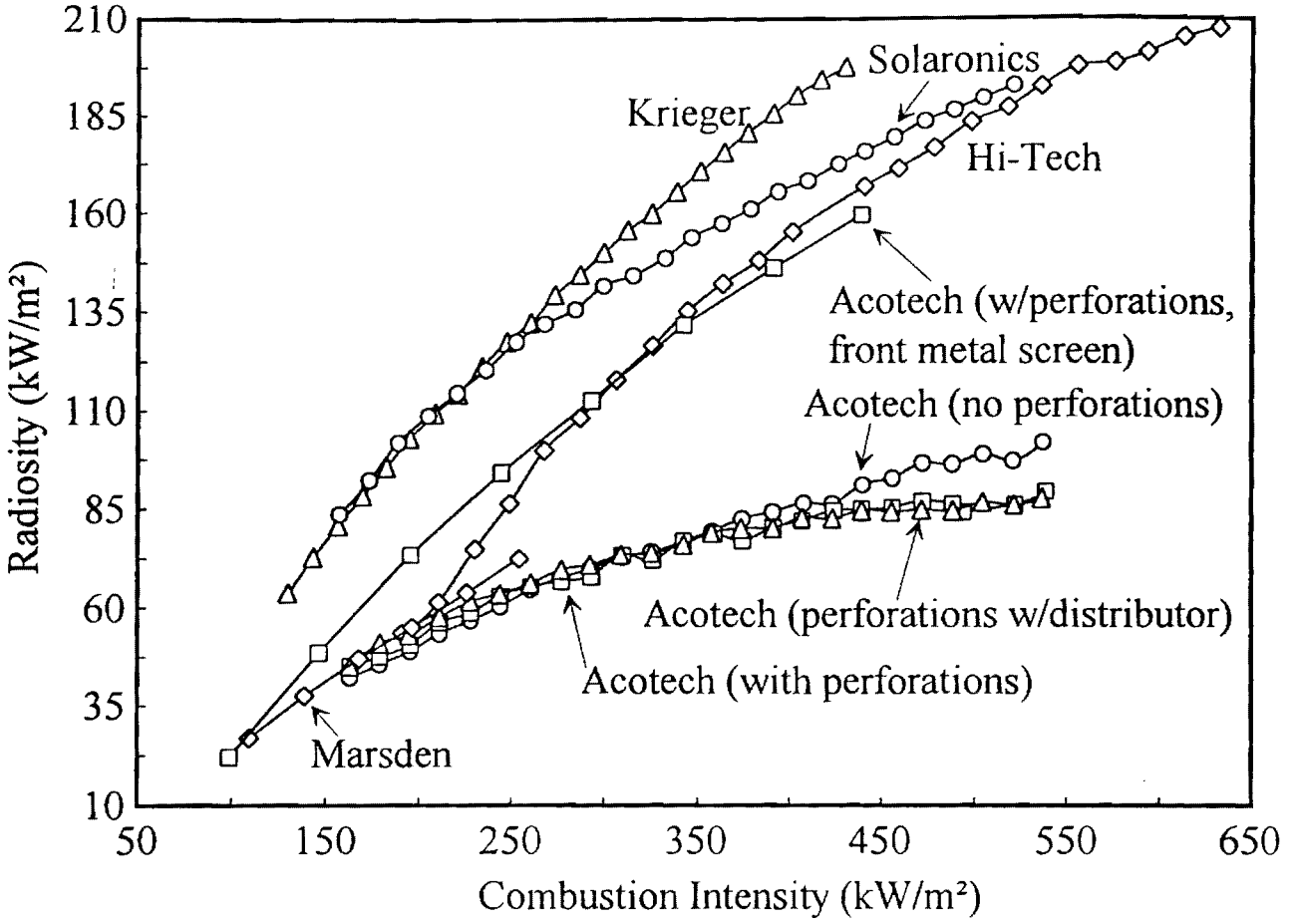
Radiosity (kW/m²)
Combustion Intensity (kW/m²)
Solaronics
Krieger
Hi-Tech
Acotech (w/perforations, front metal screen)
Acotech (no perforations)
Acotech (perforations w/distributor)
Acotech (with perforations)
Marsden
210
185
160
135
110
85
60
35
10
50
150
250
350
450
550
650

FIG 23

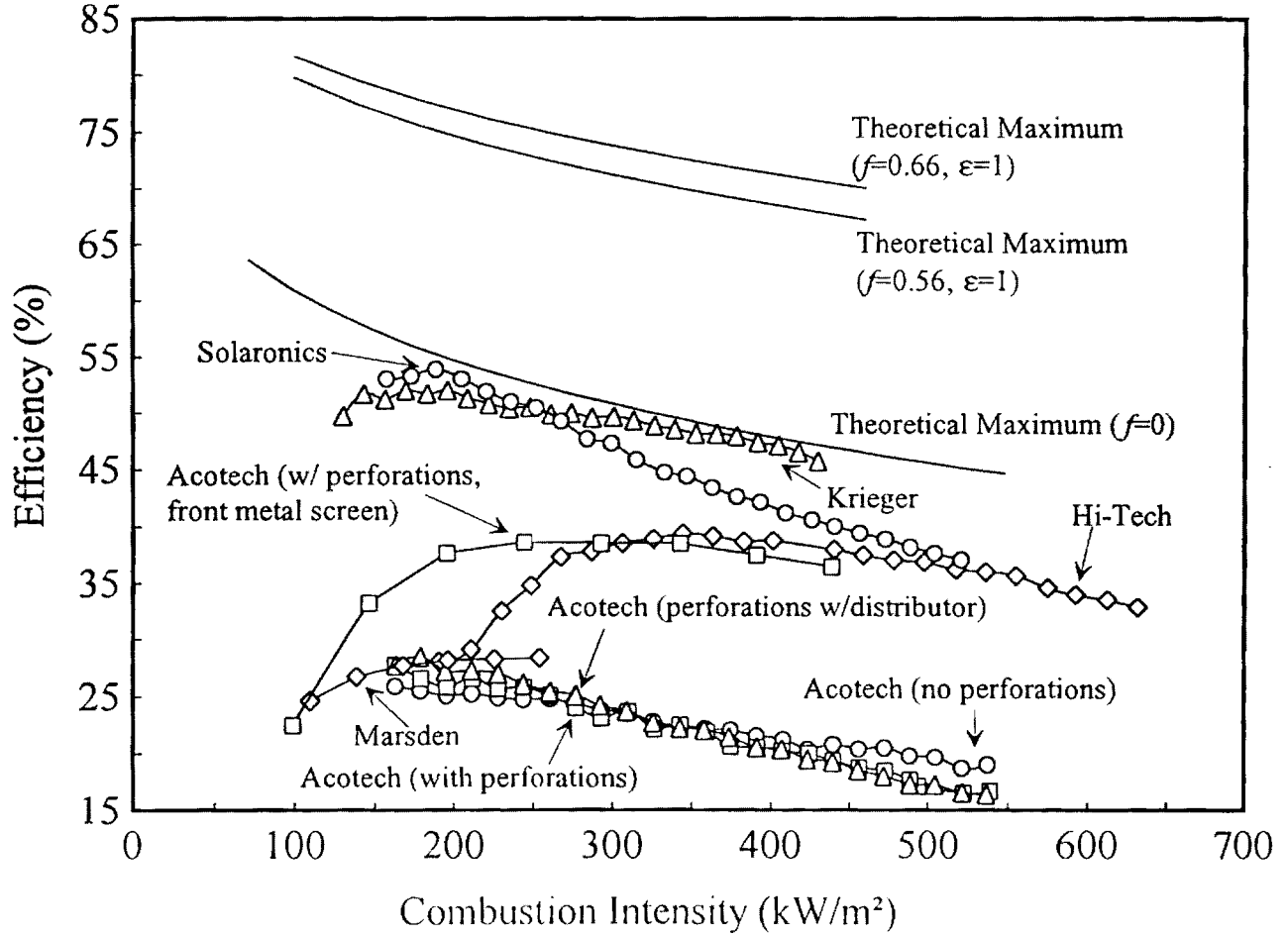
Efficiency (%)
Combustion Intensity (kW/m²)
Theoretical Maximum (f=0.66, ε=1)
Theoretical Maximum (f=0.56, ε=1)
Solaronics
Theoretical Maximum (f=0)
Acotech (w/ perforations, front metal screen)
Krieger
Hi-Tech
Acotech (perforations w/distributor)
Acotech (no perforations)
Marsden
Acotech (with perforations)
85
75
65
55
45
35
25
15
0
100
200
300
400
500
600
700

FIG 24

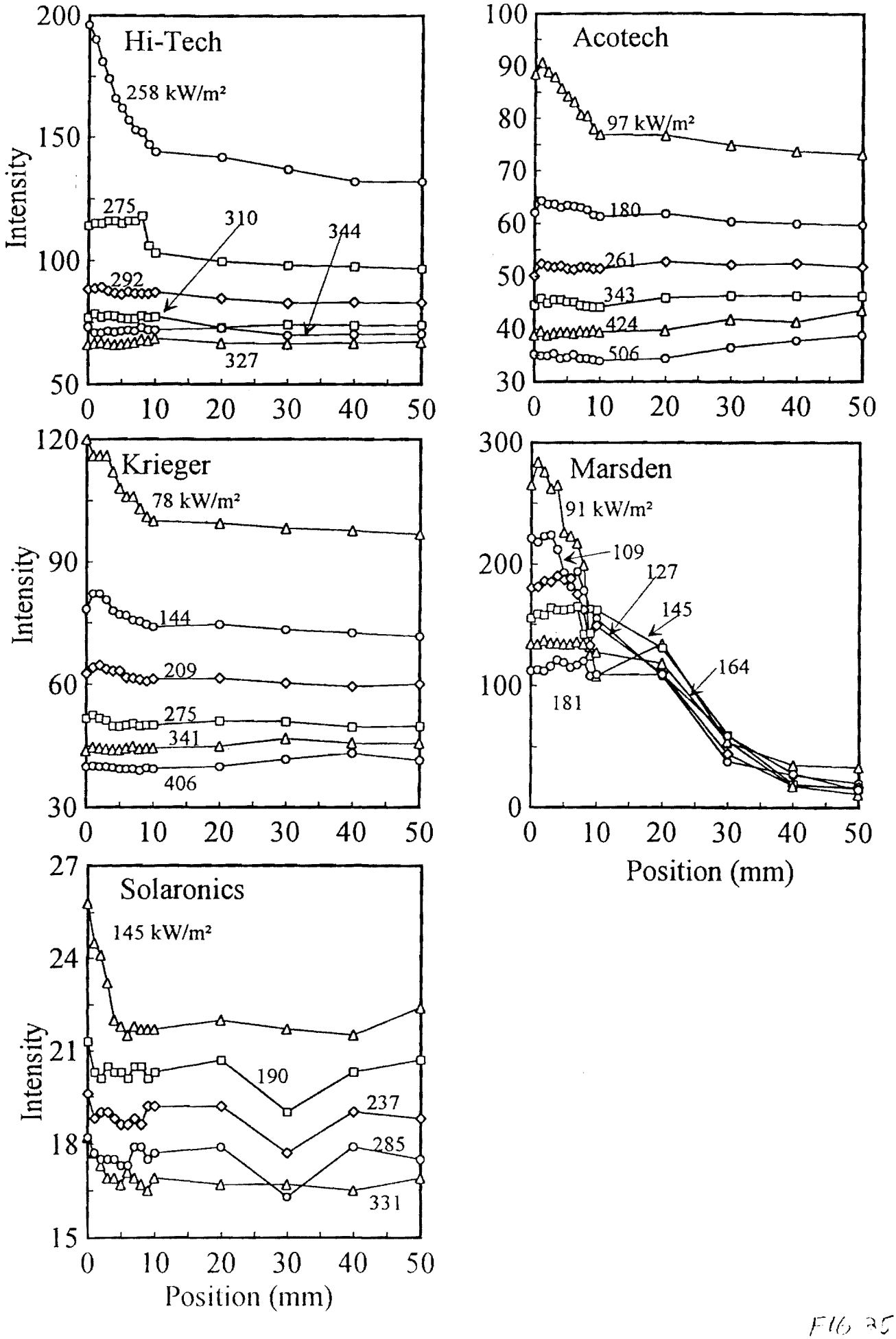
Hi-Tech
258 kW/m²
275
310
344
292
327
Intensity
Acotech
97 kW/m²
180
261
343
424
506
Krieger
78 kW/m²
144
209
275
341
406
Intensity
Marsden
91 kW/m²
109
127
145
164
181
Position (mm)
Solaronics
145 kW/m²
190
237
285
331
Intensity
Position (mm)

FIG 35

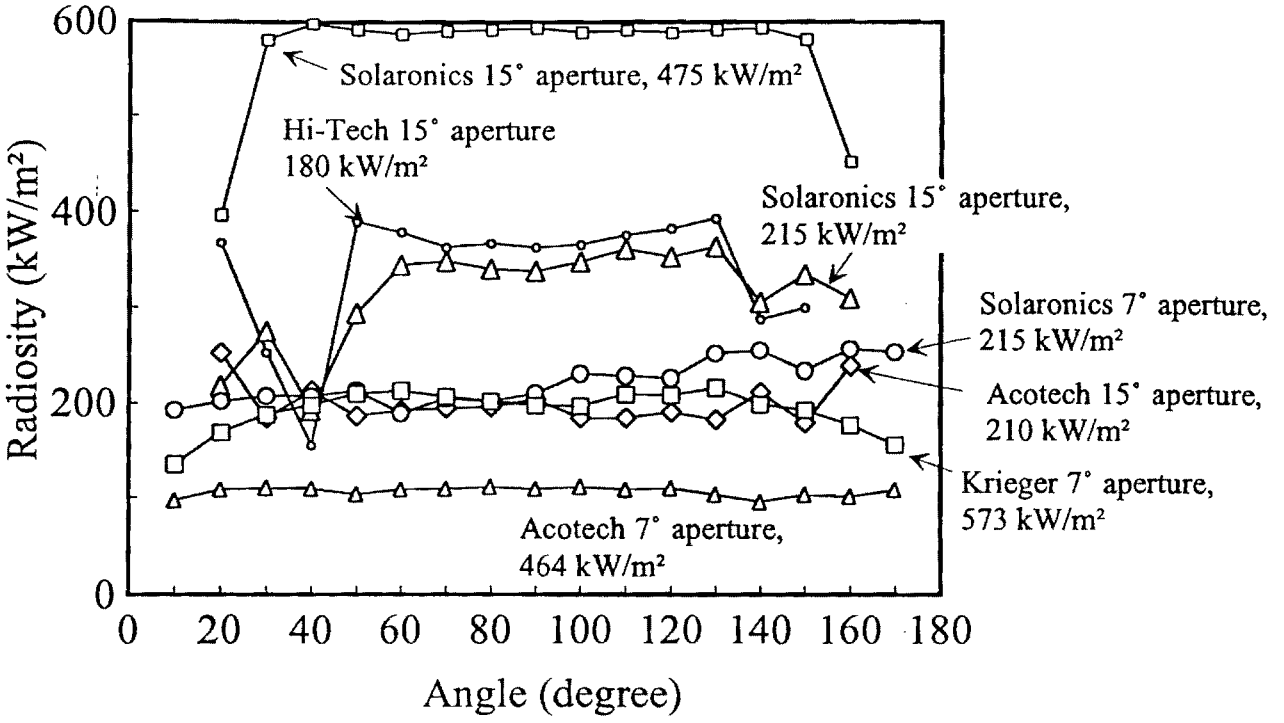
600
400
200
0
Radiosity (kW/m²)
0
20
40
60
80
100
120
140
160
180
Angle (degree)
Solaronics 15° aperture, 475 kW/m²
Hi-Tech 15° aperture
180 kW/m²
Solaronics 15° aperture,
215 kW/m²
Solaronics 7° aperture,
215 kW/m²
Acotech 15° aperture,
210 kW/m²
Krieger 7° aperture,
573 kW/m²
Acotech 7° aperture,
464 kW/m²

F16 26

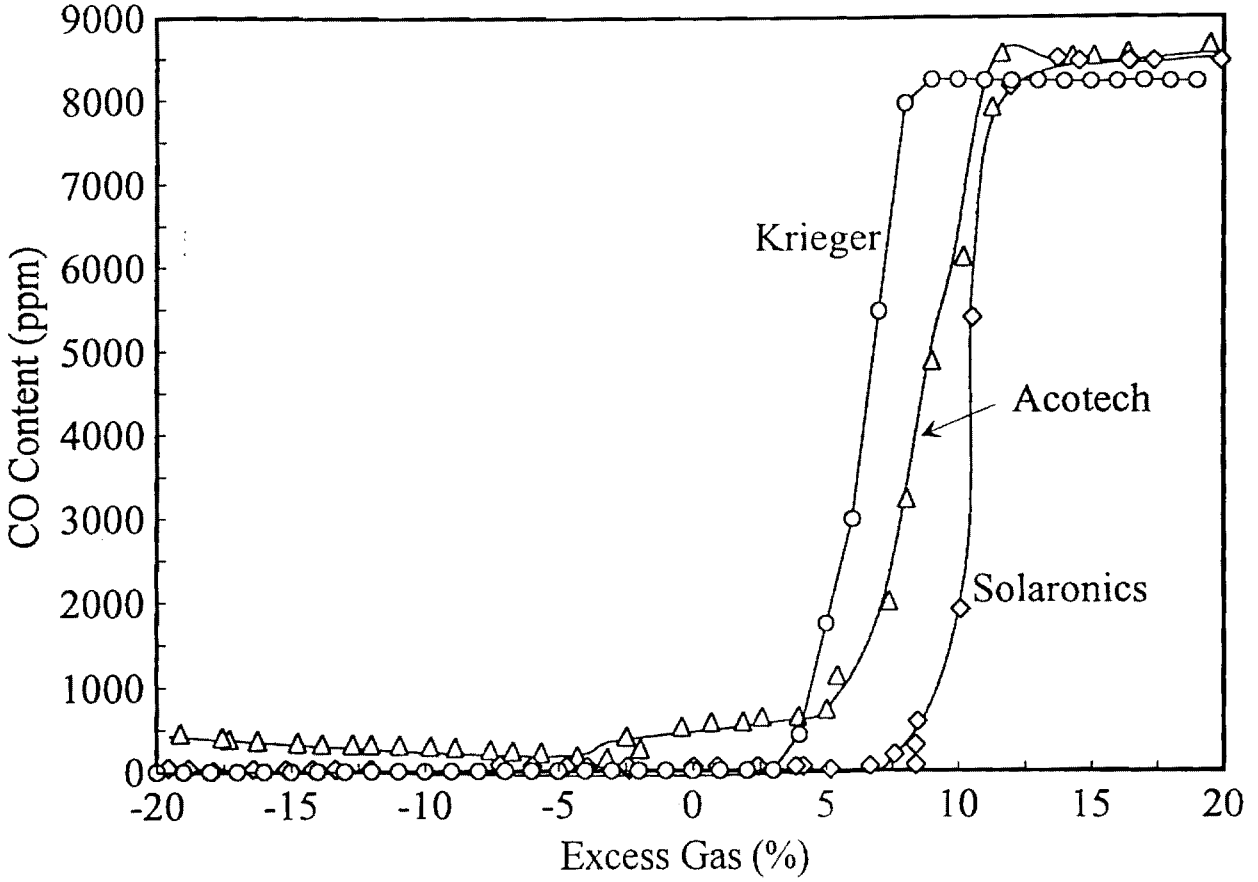
9000
8000
7000
6000
5000
4000
3000
2000
1000
0
CO Content (ppm)
-20
-15
-10
-5
0
5
10
15
20
Excess Gas (%)
Krieger
Acotech
Solaronics

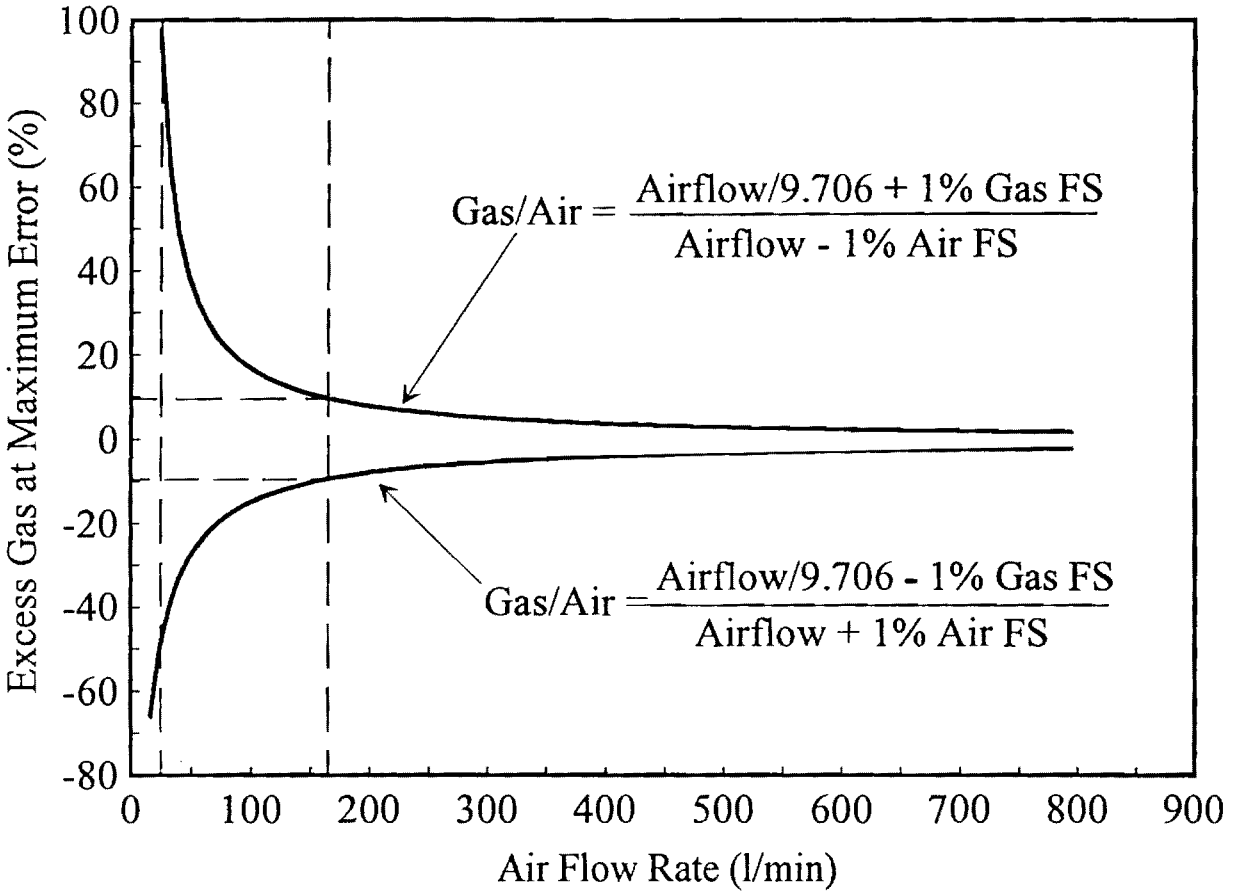
100
80
60
40
20
0
-20
-40
-60
-80
Excess Gas at Maximum Error (%)
0
100
200
300
400
500
600
700
800
900
Air Flow Rate (l/min)
Gas/Air = Airflow/9.706 + 1% Gas FS / Airflow - 1% Air FS
Gas/Air = Airflow/9.706 - 1% Gas FS / Airflow + 1% Air FS

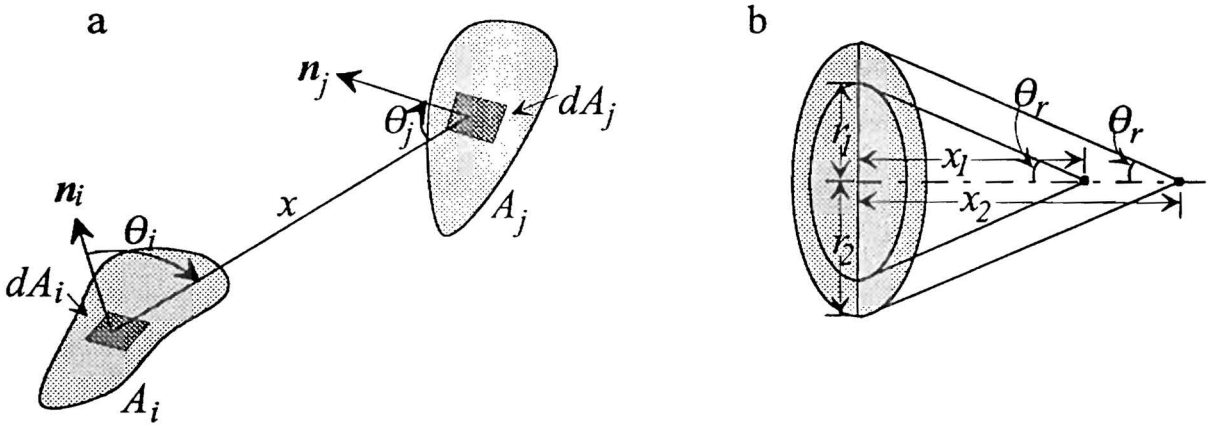

F16 29

EFFECT OF FLAME SUPPORT LAYER GEOMETRY AND MATERIALS ON THE RADIANT EFFICIENCY OF GAS RADIANT BURNERS

Gaurav Agarwal, Wen-Yi Lin, and Robert F. Speyer,

School of Materials Science and Engineering, Georgia Institute of Technology, Atlanta, GA 30332

ABSTRACT

Parallel rods/tubes were used to study variations in geometry and materials of flame support layers on radiant burners. The prediction of the maximum efficiency heat transfer model that the efficiency of a radiant burner increases with increasing flame support layer fraction closed area was confirmed experimentally. Thinner rods (with percent closed area constant), having a lower thermal conduction resistance, fostered higher efficiency. Greater distances between the base and rods decreased efficiency due to air entrainment. Conduction thermal isolation of radiating materials from the burner housing has a marked effect on burner efficiency. Low to high efficiency was measured for alumina, mullite and oxidized stainless steel rods, respectively; this was directly related to the emittances of the materials used. SiC and $MoSi_2$ coatings on alumina rods resulted in burners which were as efficient as one with stainless steel rods. A burner designed as a restricted band spectral emitter was not as efficient in its high emission range as a more greybody emitter under the same combustion intensity; the higher temperature spectral emitter discouraged extraction of sensible heat from the combustion product stream.

1 INTRODUCTION

Our accompanying work[1, 2] showed the merits of a flame support layer in increasing the efficiency of gas radiant burners. For commercial burners, a flame support layer generally takes the form of a metal screen. In the design of a burner manufactured by Hi-Tech Ceramics, Inc., a comparatively open reticulated ceramic foam functions as a flame support layer, bonded to the downstream side of a lower permeability reticulated ceramic diffuser base. Another company with a burner under development, Ceramic Fillers, Inc., uses rows of ceramic tubes as a flame support layer in front of a porous ceramic base.

The maximum efficiency heat transfer model[1] indicates that the flame support layer should have a high emittance, high blocking surface, and have a surface conducive to con-

vective heat transfer. The aforementioned tube/rod-type flame support layer facilitated an experimentally convenient way to study the effects of materials and geometries, and thus to experimentally evaluate the predictions of the model.

2 EXPERIMENTAL PROCEDURE

A Hi-Tech burner was altered by scraping off the flame support layer so that only the base tile was used. This base (25.6 pores/cm) was mounted on an Eclipse housing, which in turn was threaded onto our burner testing rig, described elsewhere[1][3]. Mounted on each side of the housing were steel plates, 6.0 mm thick with a length matching that of the side dimension of the burner (15.2 cm). The plates extended perpendicularly away from the burner face, with holes machined at uniform distances, where tubes/rods could be inserted. A standard mixture of 7.5% excess gas was used throughout, unless otherwise stated.

To study the effect of percent closed area of the flame support layer, 3.2, 2.4, and 1.6 mm solid rods, made of either stainless steel (Type 304 stainless steel, Small Parts, Inc., Miami Lakes, FL) or alumina (99.8% purity, Coors Ceramics Co., Golden, CO) were used. Each rod set was inserted into the same hole spacing, resulting in percent closed areas of 50.0, 66.6, and 75.0%, respectively. The distance between the base and the closest upstream surface of the rods was 7 mm. To measure the effect of varying the rod diameter, maintaining the percent closed area constant, three sets of hole spacings were machined into the steel side plates. For the 3.2, 2.4, and 1.6 mm rods, distances between hole centers were 6.33, 4.22 and 3.16 mm, all resulting in a percent closed area of 50%. The setting of the side plates was changed when different hole spacings were used so that the distance between the base and the closest upstream surface of the rods was maintained at a constant 7 mm. The effect of varying base/flame support layer distance was investigated using 3.2 mm rods with a 6.3 mm center-to-center inter-rod spacing. Base-rod distances were altered by repositioning the clamp points and set screw adjustments of the side plates. The effect of conductive heat loss from the flame support layer to the housing was investigated using 2.4 mm rods in 4.2 mm holes, with and without insulating glass wool at the contact points between them.

Alumina and steel rods, as well as alumina and mullite tubes, were used to study the

effect of flame support layer materials. The outer diameters of tubes/rods were 3.2 mm. The inner diameter of Al_2O_3 tubes was 1.6 mm and for mullite tubes was 1.6 mm and 2.3 mm. Center to center spacings between rods/tubes was 6.3 mm. Coatings of SiC (99.9% pure, -325 mesh, Norton Co., Worcester, MA), $La_2Cr_2O_6$ and $MoSi_2$ (99.5% pure, -325 mesh, Cerac Inc., Milwaukee, WI) were applied to 3.2 mm diameter alumina rods. $La_2Cr_2O_6$ was prepared by reacting (1100°C, 1 h) equimolar amounts of La_2CO_3 (99.99% pure, Cerac Inc., Milwaukee, WI) and Cr_2O_3 (99.99% pure, Cerac Inc., Milwaukee, WI). $La_2Cr_2O_6$ and $MoSi_2$ powders were wet milled with distilled water for 12 hours. The water content was adjusted after ball milling to formulate a slurry with a low viscosity suited for dip coating. Alumina rods were then dipped while constantly stirring the slurry. These rods were then dried for 6 h at 100°C. The coatings were then fired during testing as flame support layers. SiC coatings were applied via a spray, dried similarly, and then fired at 1000°C in air for 30 minutes.

The spectral behavior of the aforementioned rods, tubes, and coatings, along with fused silica tubes was investigated using a spectral radiometer. Reported efficiencies were based on data from a calibrated total radiation pyrometer[1][3].

3 RESULTS AND DISCUSSION

Figure 1 shows that closing the mutual distance between rods increases burner efficiency. This was predicted by the maximum efficiency model: With increasing fraction closed area, a greater proportion of combustion products exiting the base convected to the flame support layer. This decreased the heat lost as exhausted combustion products, therefore increasing efficiency. Keeping the percent opening the same, larger diameter stainless steel rods showed lower efficiency than a larger quantity of smaller diameter rods (Figure 2). The larger rods with correspondingly greater inter-rod spacing resulted in the convective surface area remaining constant. Therefore surface area cannot be used to explain decreasing efficiency with increasing rod diameter. Rather the diminished efficiency is related to the increased thermal resistance of the larger rods. This thermal resistance would be a determining factor in conduction of absorbed energy from the upstream side to the downstream side, where it would be radiated to the load. The same general trend was apparent for alumina, though with considerably less spread and some crossover. For

Figure 1: Effect of increasing flame support layer rod diameter on burner efficiency. Solid symbols: stainless steel rods. Open symbols: alumina rods. Numbers in the figure indicate the outer diameter of the rods in mm.

Figure 2: Effect of rod diameter (marked in the figure in units of millimeters), maintaining a 50% closed area in the flame support layer. Open symbols: stainless steel rods. Solid symbols: alumina rods.

alumina, it is interpreted that the emittance of the thicker rods were higher: Emissions can originate in the bulk of a semi-transparent medium; thus, larger volume rods will provide more sites for radiative emission. The competition of effects resulted in a much less precipitous change in efficiency with rod size for the alumina rods, as compared to the stainless steel rods.

Figure 3 shows a generally decreasing efficiency as the flame support layer rods are moved to more extended positions from the base. Extended distances encouraged mixing of ambient air with combustion products exiting the base, so that leading up to when the combustion product stream reached the flame support layer, its heat content was attenuated. At low flow rate, an increase, followed by a decrease in efficiency is measured with increasing combustion intensity. The initial increase in efficiency may be attributed to an increase in turbulent flow via the increased open volume between the base and the flame support layer rods. The results shown in Figure 3 can be viewed in a different fashion, where the abscissa is in terms of combustion intensity (Figure 4). Accompanying work[1] showed that the flame lifts downstream of the base for combustion intensities lower than that of the maximum in efficiency. It is apparent from Figure 4 that the maximum in efficiency Decreased base temperatures do not foster rapid combustion of emerging mixture, causing this. shifts to lower combustion intensity as the rods are moved closer to the base. Entrainment of ambient air between the base and the flame support layer lowers the temperature of combustion products and solids. Thus, extended base/flame support layer distances, which foster entrainment, would allow flame liftoff to persist at higher combustion intensities.

Heat losses through conduction to the housing can be appreciable, as shown in Figure 5. The increase in efficiency with insulation is greater at low combustion intensities ($\sim$7% at 172 kW/m^2) than high combustion intensities ($\sim$3% at 345 kW/m^2). It is therefore not surprising that commercial burner manufacturers, such as Solaronics[1] design carefully for thermal isolation of radiating surfaces from the burner housing.

As can be seen from Figure 6, for the same outer diameter, alumina, mullite, and oxidized stainless steel demonstrate low to high efficiency, respectively. This can be directly related to the emittance of the materials, determined from spectral data shown in Figure 7. The greybody emittance of the mullite tubes was lower than steel rods, while the alumina rods were still lower and deviated significantly from greybody behavior. A

Figure 3: Burner efficiency as a function of distance of the stainless steel flame support layer rods from the base. Numbers in the figure correspond to the combustion intensity in kW/m^2.

Figure 4: Burner efficiency as a function of combustion intensity. Numbers in the figure correspond to distances (mm) between the base surface and the closest upstream surface of the steel rods. The dashed line shows the shift in efficiency maxima.

Figure 5: Effect of insertion of glass wool at contact points between the stainless steel flame support layer rods and the machined holes in the steel side plates.

Figure 6: Effect of flame support layer materials on efficiency. Outer diameter of all rods was 3.2 mm.

Figure 7: Radiation spectra using a Hi-Tech base and various materials as flame support layer rods. Combustion intensity: 361 kW/m^2. Mixture: 5.9% excess gas.

significant increase in efficiency is apparent when alumina tubes are replaced by alumina rods (Figure 6). The effect of varying inner diameter of mullite rods is not as distinct. It is interpreted that mullite is a higher and more grey emitting/absorbing material, so that radiation is more largely a surface phenomenon, and therefore more thickness independent. Radiation from alumina, being more transmissive, would originate to a greater degree from the interior. Thus, as argued previously, the greater solid volume rods would result in a greater emittance. This would in turn increase the efficiency of the burner.

Figure 8 shows the effect of various coatings on alumina rods. Alumina was chosen as the substrate material because of its low emittance. In this way, increases in efficiency over that of alumina rods could clearly be attributed to the merits of the coating. $La_2Cr_2O_6$ coatings increased burner efficiency over uncoated rods. However, SiC and $MoSi_2$ coatings showed the highest improvement. Spectral results (Figure 9) show again that the high efficiencies correlate well to high averaged burner emittance.

Rather than designing a burner for spectrally uniform emission, there may be an advantage for burners which sharply emit in a spectral range for which the load was highly absorbing. As an example, for shaping flat glass into automobile rear windshields. The spectra of a typical window (Na_2O-CaO-SiO_2) glass is shown in Figure 10. As can be seen, glass becomes highly absorbing at wavelengths longer than $\sim$2.7 μm. Pure fused silica would have a cutoff at slightly longer wavelengths ($\sim$3.4 μm)[5]. The spectral range where a material is highly absorbing is the same spectral range where the material is highly emitting. Thus, it was thought that using a fused silica tube flame support layer would spectrally emit in a wavelength range where a glass load would be highly absorptive. The spectral radiosity of such a burner is shown in Figure 11. Assuming that in the spectral range 2000-2600 nm, the glass rods were fully transmissive, a simplex fit to this band represents radiation from the base material alone. Subtracting this greybody spectra from the spectral radiosity of the burner provides an indication of radiation contribution from the glass tubes (plus the contributions from combustion product emissions). The enhanced radiant emissions for wavelengths in excess of 3000 nm might indicate that such a burner would be effective in transferring heat to a glass load. However, integrating the area under the spectral radiosity curve from 2700 to 5000 nm results in a power output of 48.2 kW/m^2, whereas the same integration of a $MoSi_2$-coated alumina rod flame support layer burner, under the same combustion intensity, yields a power output of 56.3

Figure 8: Effect of coating material on alumina rods.

Figure 9: Radiation spectra for the Hi-Tech base with various coatings on alumina rods, functioning as a flame support layer. Combustion intensity: 361 kW/m^2. Mixture: 5.9% excess gas.

Figure 10: Variation of spectral absorption coefficient of window glass with wavelength[4]. Superimposed is the Planck blackbody distribution at 1400°C.

Figure 11: Circles: Spectral radiosity of a burner with a fused silica tube flame support layer on a Hi-Tech base, using a combustion intensity of 361 kW/m^2 and a mixture of 9% excess gas. Tubes were 3 mm OD and 1 mm ID. Line: best-fit greybody distribution (T = 949°C, ϵ = 0.8), fit in the spectral range 2000-2600 nm. Squares: subtraction of greybody distribution from the spectral radiosity measured from the burner.

kW/m^2. Clearly then, there is no advantage to a spectral emitter to exploit the absorption behavior of a load. Qualitatively, the fact that the glass rods could only emit in at wavelengths longer than 2700 nm would cause the rods to sustain a higher steady state temperature than a more grey flame support layer. This higher temperature would decrease the sensible heat removed from combustion products, resulting in a lower burner radiosity throughout the electromagnetic spectrum.

4 CONCLUSIONS

Rod/tube burners demonstrated the effects of fraction closed area of the flame support layer, distance of the flame support layer to the base, and the effect of surface emittances on burner efficiency. The efficiency of the burner, as well as its temperature, increased with increasing blocking area on the flame support layer. Clearly then, the next generation improved burners must be made of materials refractory enough to withstand these temperatures, while at the same time, demonstrate good thermal shock resistance and high emittance.

5 ACKNOWLEDGEMENTS

We greatly appreciate the assistance and helpful advice of Drs. Joe K. Cochran and James Lee. The authors acknowledge Dr. Kevin Krist of the Gas Research Institute and Mr. Shyam Singh of SSEEI, Inc., for funding this investigation. This manuscript was prepared by the Georgia Institute of Technology as an account of work sponsored by the Gas Research Institute. Neither GRI, members of GRI, nor any person acting on behalf of either; A. Makes any warranty or representation, expressed or implied, with respect to the accuracy, completeness, or usefulness of the information contained in this manuscript, or that the use of any information, apparatus, method, or process disclosed in this manuscript may not infringe on privately-owned rights, or B. Assumes any liability with respect to the use of, or for damages resulting from the use of, any information, apparatus, method, or process disclosed in this manuscript.

References

[1] R. F. Speyer, W. Lin, and G. Agarwal, and R. F. Speyer, "Radiant Efficiencies of Commercially Manufactured Gas Radiant Burners", unpublished work.

[2] W. Lin, G. Agarwal, and R. F. Speyer, "Performance Considerations of Commercially Manufactured Gas Radiant Burners", unpublished work.

[3] R. F. Speyer, W. Lin, and G. Agarwal, "Performance Evaluation of Porous Radiant Gas Burners", *Journal of Experimental Heat Transfer*, vol. 8, no. 1, pp. 73-95, 1995.

[4] R. Seigel and J. R. Howell, *Radiation Heat Transfer*, Hemisphere Publishing Corp, (1992).

[5] F. D. Incropera and D. P. DeWitt, *Fundamentals of Heat and Mass Transfer*, 2d ed, John Wiley and Sons, New York, 1985.

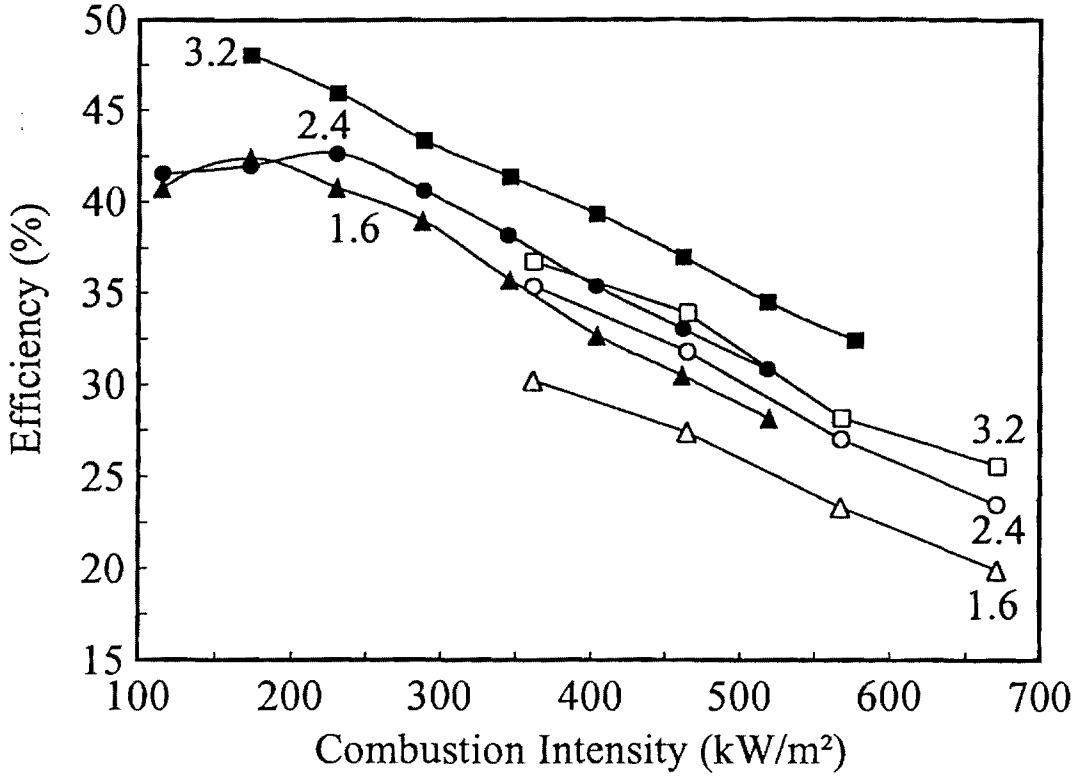
50
45
40
35
30
25
20
15
Efficiency (%)
100
200
300
400
500
600
700
Combustion Intensity (kW/m²)
3.2
2.4
1.6
3.2
2.4
1.6

F16 1

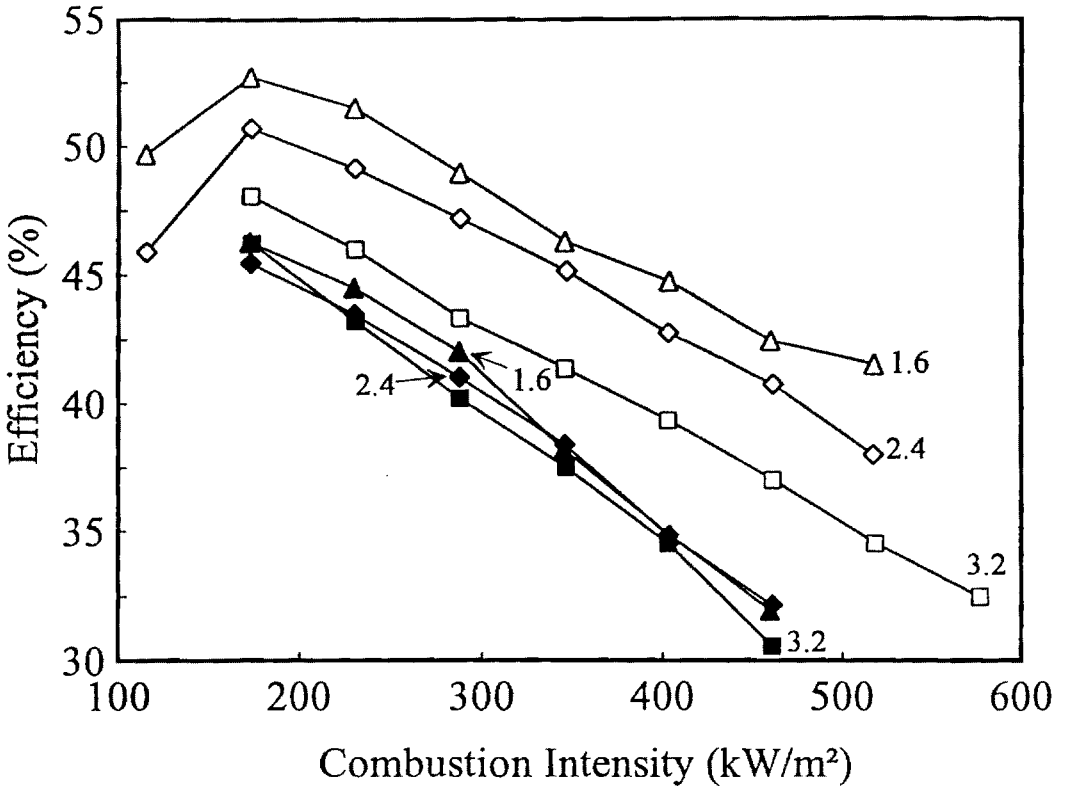
55
50
45
40
35
30
Efficiency (%)
100
200
300
400
500
600
Combustion Intensity (kW/m²)
1.6
2.4
3.2
1.6
2.4
3.2

FIG 2

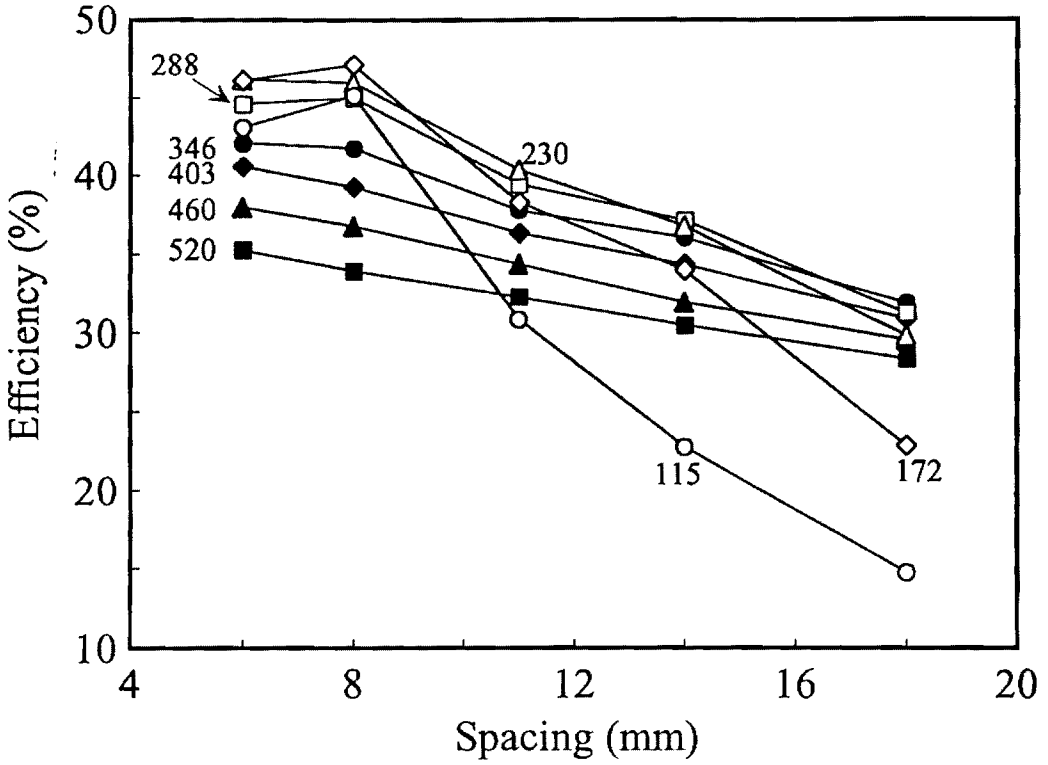
50
40
30
20
10
Efficiency (%)
288
346
403
460
520
230
115
172
4
8
12
16
20
Spacing (mm)

Fig 3

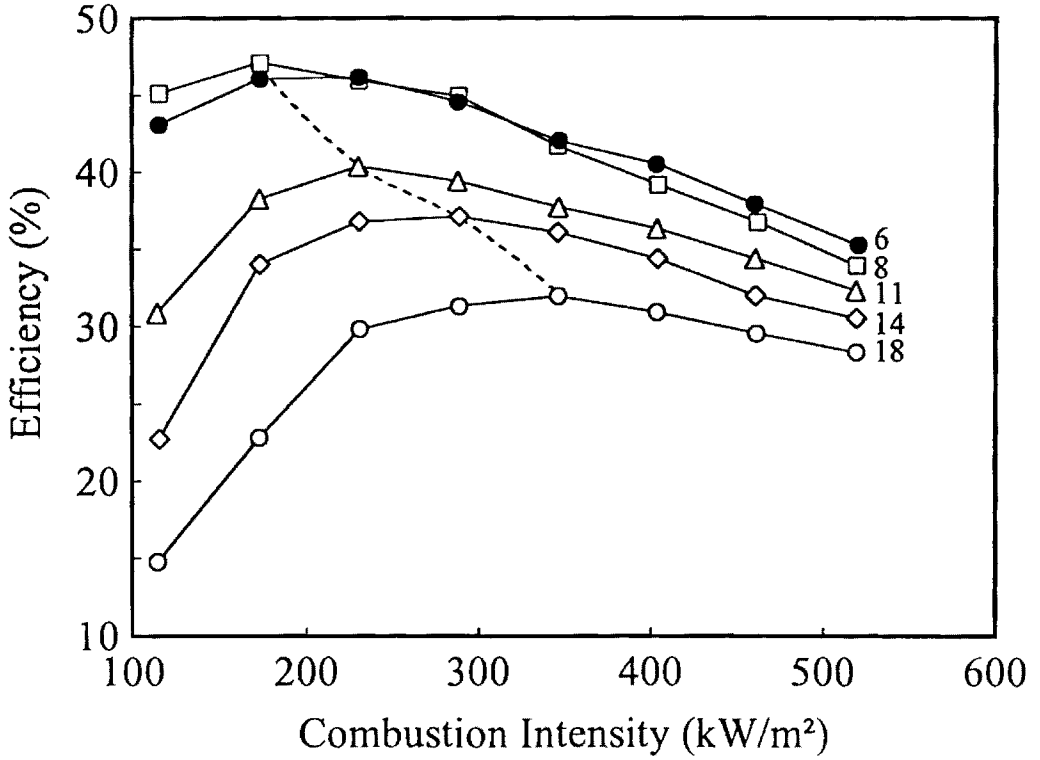
50
40
30
20
10
Efficiency (%)
6
8
11
14
18
100
200
300
400
500
600
Combustion Intensity (kW/m²)

Fig 4

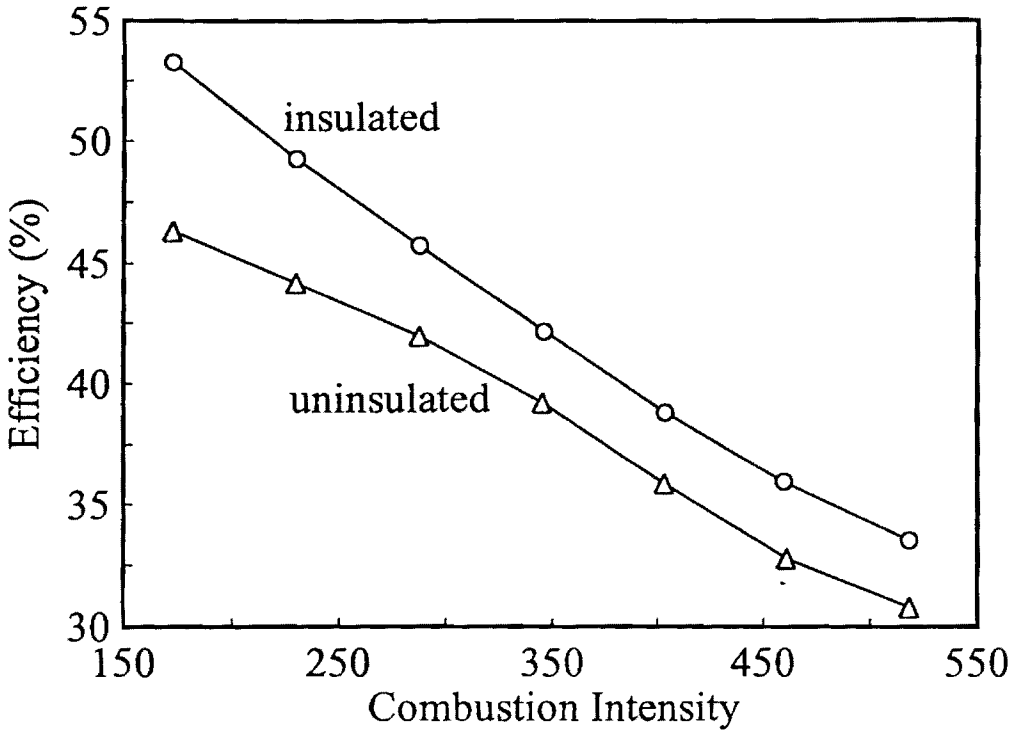
55
50
45
40
35
30
Efficiency (%)
insulated
uninsulated
150
250
350
450
550
Combustion Intensity

FIG 5

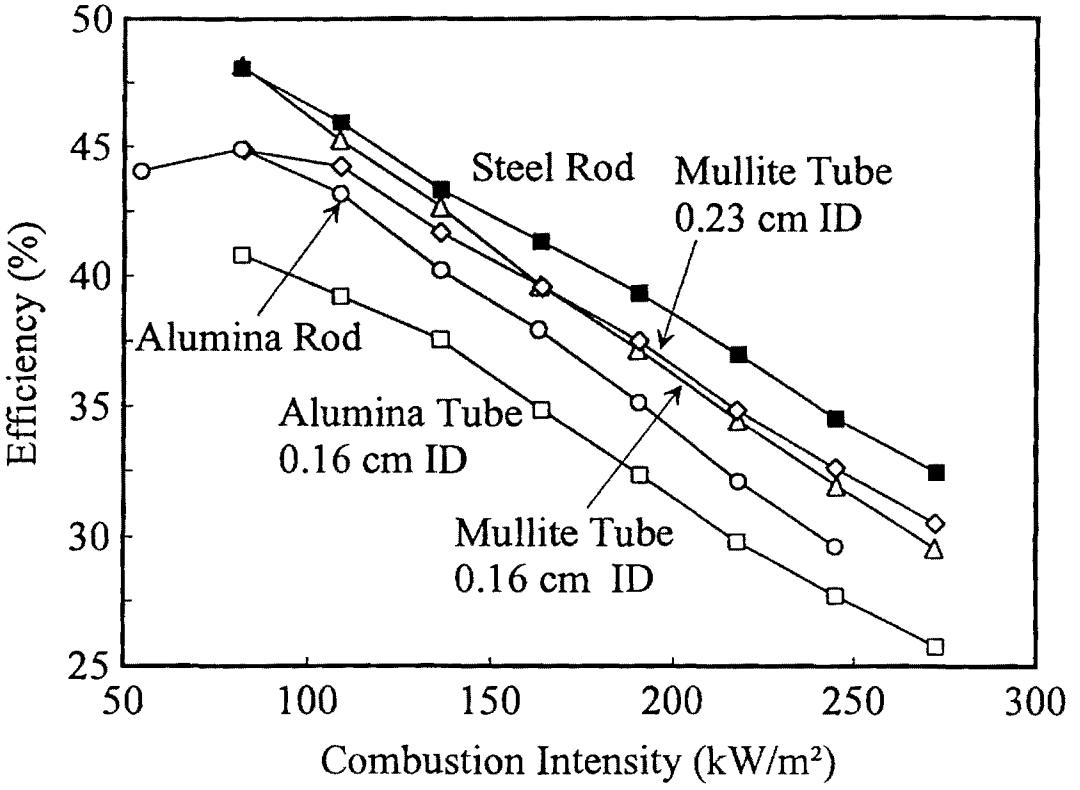
50
45
40
35
30
25
Efficiency (%)
50
100
150
200
250
300
Combustion Intensity (kW/m²)
Steel Rod
Mullite Tube
0.23 cm ID
Alumina Rod
Alumina Tube
0.16 cm ID
Mullite Tube
0.16 cm ID

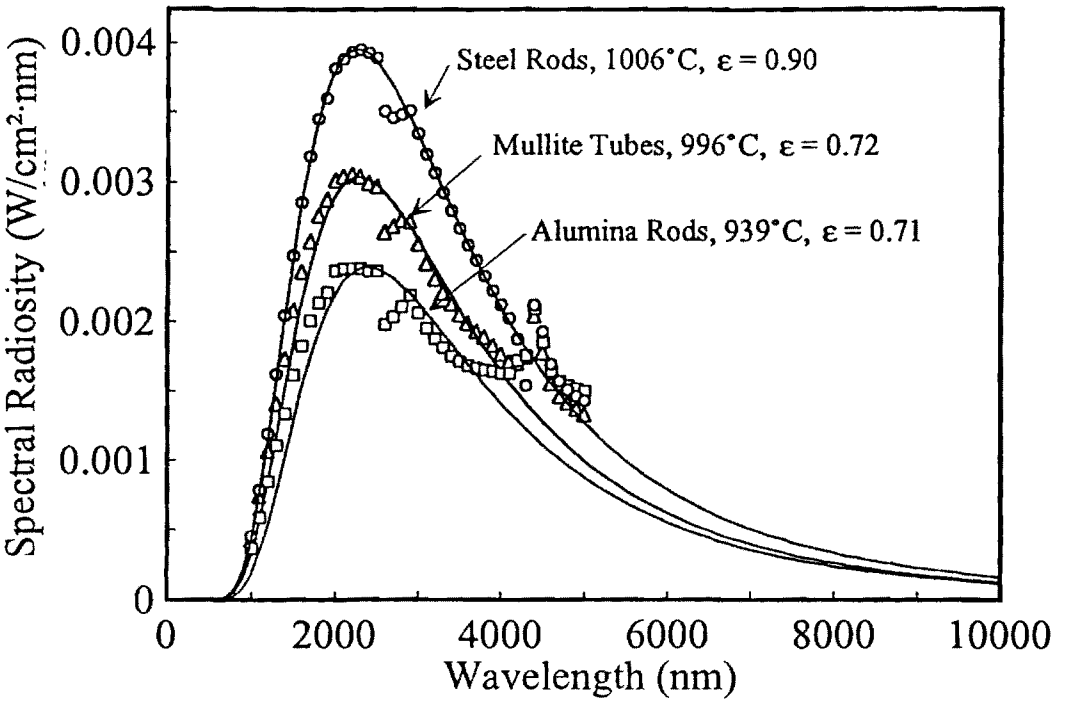
Steel Rods, 1006°C, ε = 0.90
Mullite Tubes, 996°C, ε = 0.72
Alumina Rods, 939°C, ε = 0.71
Spectral Radiosity (W/cm²·nm)
0.004
0.003
0.002
0.001
0
0
2000
4000
6000
8000
10000
Wavelength (nm)

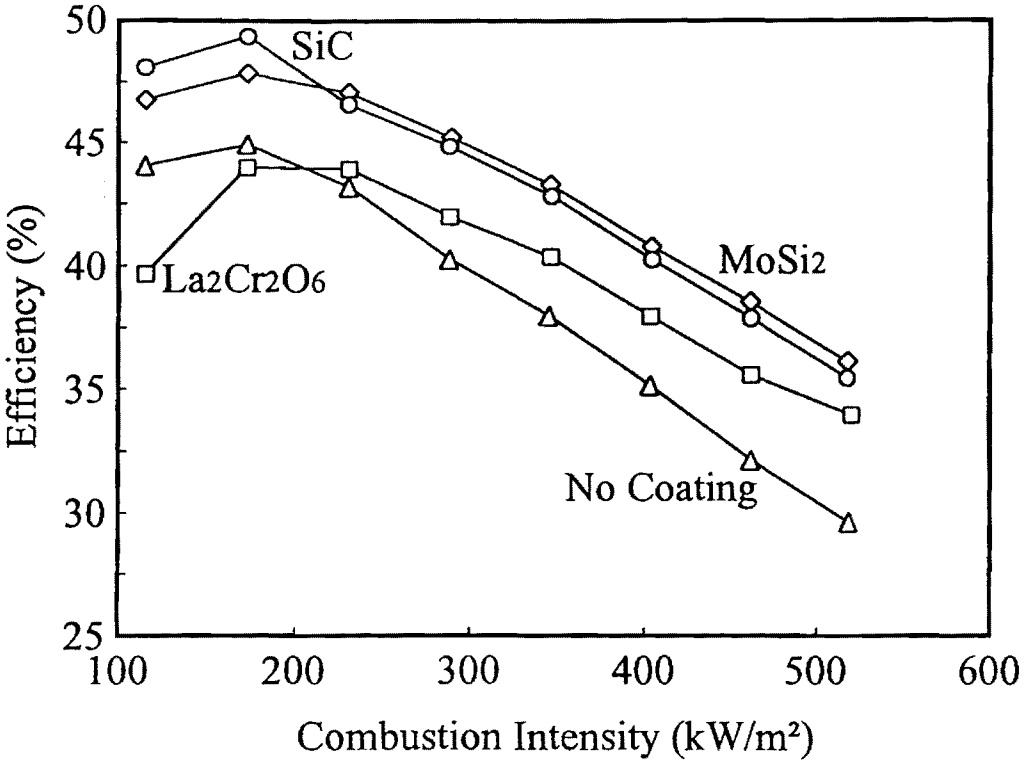
50
45
40
35
30
25
Efficiency (%)
SiC
MoSi2
La2Cr2O6
No Coating
100
200
300
400
500
600
Combustion Intensity (kW/m²)

FIG 8

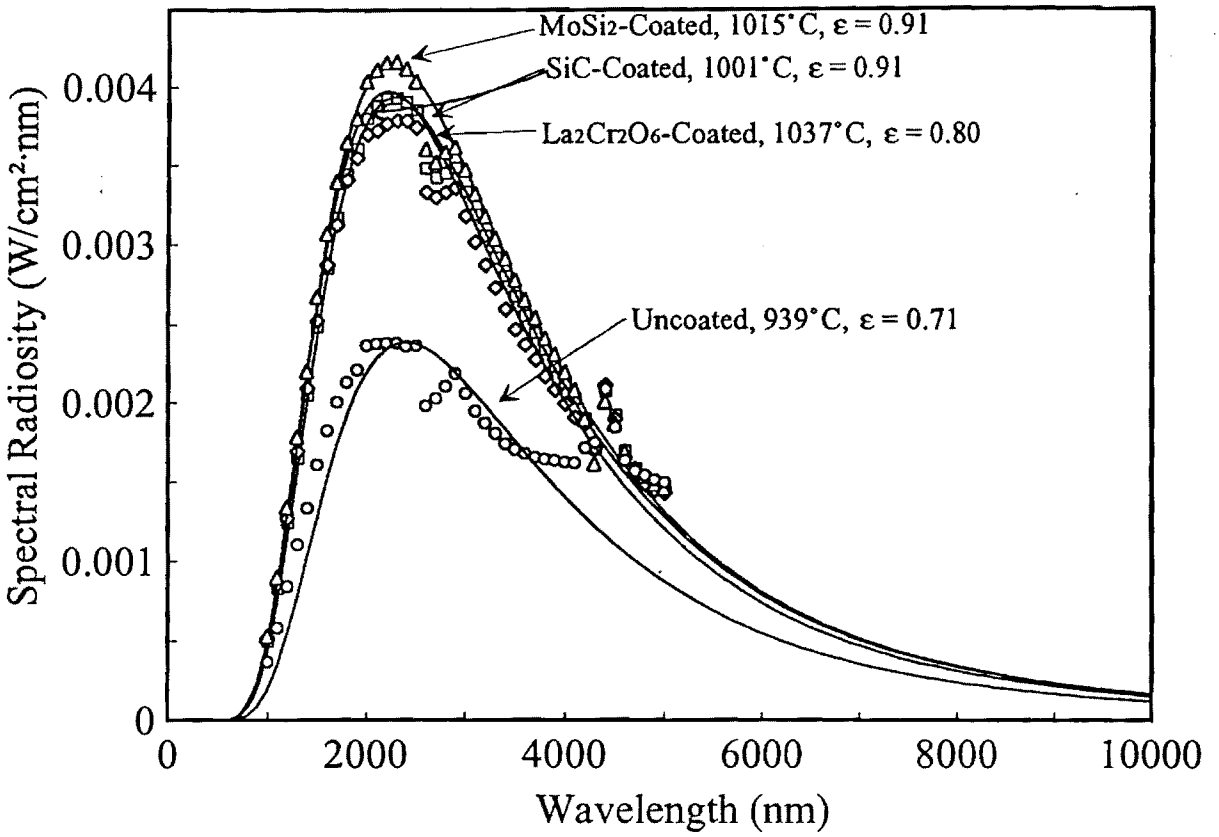
MoSi2-Coated, 1015°C, ε = 0.91
SiC-Coated, 1001°C, ε = 0.91
La2Cr2O6-Coated, 1037°C, ε = 0.80
Uncoated, 939°C, ε = 0.71
Spectral Radiosity (W/cm²·nm)
0.004
0.003
0.002
0.001
0
0
2000
4000
6000
8000
10000
Wavelength (nm)

Fig 9

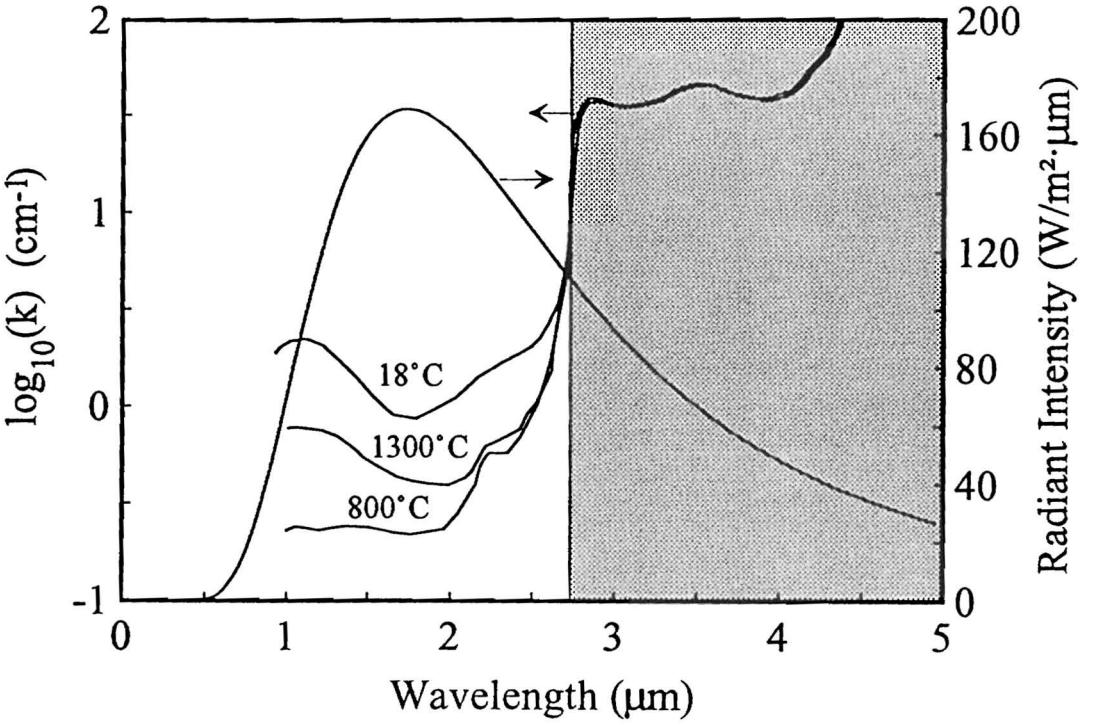
2
1
0
-1
0
1
2
3
4
5
200
160
120
80
40
0
log10(k) (cm-1)
Radiant Intensity (W/m2·μm)
Wavelength (μm)
18°C
1300°C
800°C

Fig 10

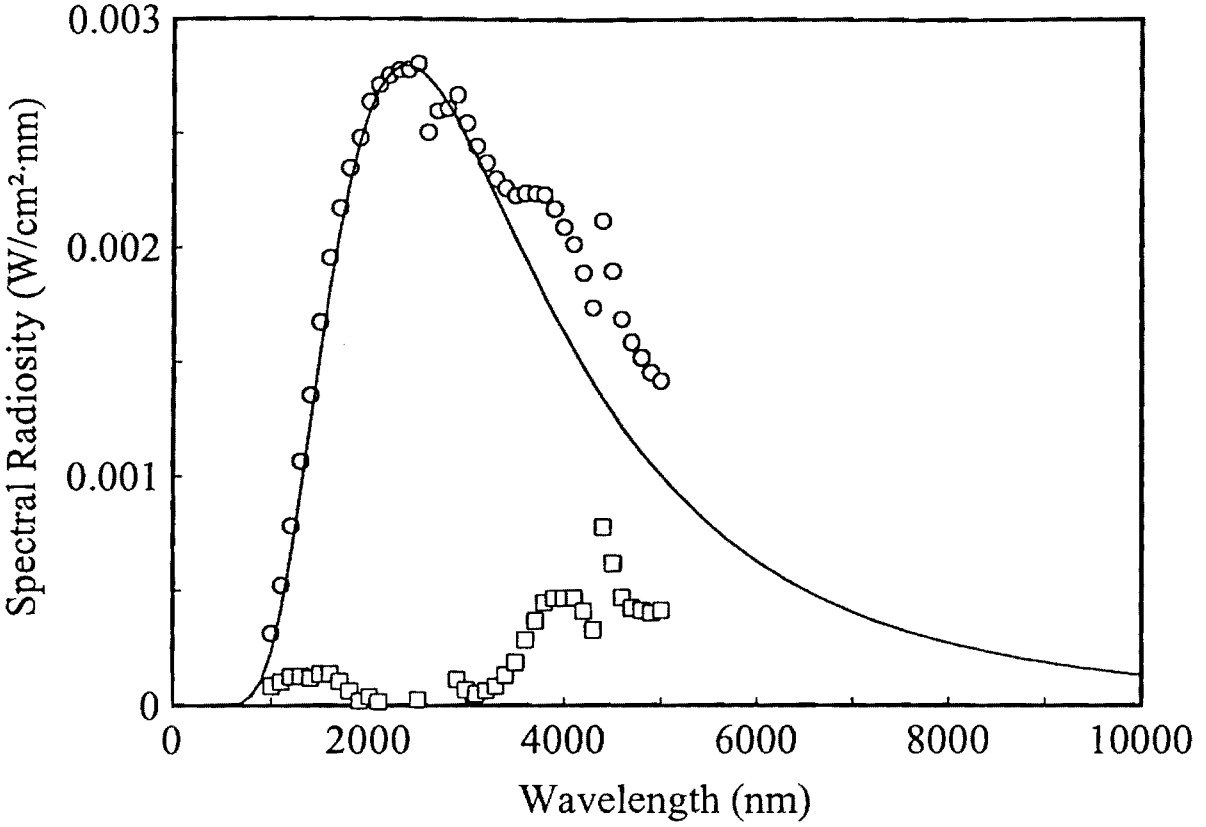
0.003
0.002
0.001
0
Spectral Radiosity (W/cm²·nm)
0
2000
4000
6000
8000
10000
Wavelength (nm)

FIG 11

PERFORMANCE CONSIDERATIONS OF COMMERCIALLY MANUFACTURED GAS RADIANT BURNERS

Wen-Yi Lin, Gaurav Agarwal, and Robert F. Speyer

School of Materials Science and Engineering, Georgia Institute of Technology, Atlanta, GA 30332

ABSTRACT

Gas radiant burners were evaluated using a spectral radiometer, from which greybody emittances and surface temperatures could be determined. Radiant efficiency was then determined using the Stefan-Boltzmann law, the results of which were in good agreement with those from a total radiation pyrometer. Acotech and Marsden burners were not effective at transferring heat from combustion products to solid surfaces, as compared to Krieger and Solaronics burners. For the Krieger burner, surface temperatures measured by optical means compared sensibly with that from a thermocouple, while greybody emittances were in agreement with literature values. Experimental results were compared to the predictions of the theoretical maximum efficiency heat transfer model. Burner orientation did not have a significant effect, while a mixture preheated to 120°C resulted in a 3.2% increase in the value of efficiency. NO_x emissions from the burners increased with increasing combustion intensity, ranging from 16-38 ppm.

1 INTRODUCTION

Gas radiant burners are judged based on their cost, longevity, range of radiant power output, and their radiant efficiency. In this and the accompanying work[1], our focus has been to characterize the efficiencies of commercially marketed burners. Since this is a most important criterion for both consumers and manufacturers of this technology, the work presented herein further evaluates burner efficiency by another means; a spectral radiation pyrometer. The accompanying work showed that commercial burners perform well below the theoretical limit for efficiency. For these burner designs, further improvements in efficiency may come from higher solid emittances, higher flame support layer blocking surface area, and improved solid surface textures and surface geometries for high convec-

tive heat transfer. Other methods of efficiency enhancement entail mixture preheating, or using an oxygen enriched air supply; the former topic was evaluated herein.

One of the distinct advantages of these burners over an open flame is the significant reduction in NO_x emissions[3]. This results from the rapid removal of heat from the flame by solid surfaces, diminishing thermally generated NO_x. Some practical considerations such as the effect of burner orientation, and the lean mixture limit were also evaluated.

2 EXPERIMENTAL PROCEDURE

The effect of burner orientation was studied using an adjustable adapter fitting between the mixer and the burner housing. Burner face orientations of: vertical, 45° from vertical, horizontal, and 45° downward from horizontal were used. The temperatures of the burner housings were measured by locking a chromel/alumel thermocouple junction to the side of the burner housing, using a screw head. The temperature of the mixture just upstream of the back side of the burner tile, or the back side of the burner tile itself, was measured using a platinum resistance temperature detector (RTD, encased in a thin, flat ceramic housing). A vacuum seal feed-through connector was used to carry the RTD (1000Ω at 0°C) signal out of the burner housing. The RTD was used in favor of a thermocouple, since it circumvented the problem of cold junction compensation at the connector which had a variable temperature.

The air line preheater (Sylvania Emissive Products, Exeter, NH) consisted of a steel gas flow tube with coiled nichrome heating element wire within it. Preheat temperature was maintained by proportional-integral-derivative feedback control on preheater element power, based on an upstream chomel/alumel thermocouple. Once a constant air preheat temperature was established for 10 min, the power setting to the pre-heater was fixed, and the gas and air mass flow controllers were re-balanced to the mixture previously determined (without preheat) which results in maximum efficiency. The temperature of the mixture measured by the RTD just upstream of the burner tile was taken as the true preheat temperature; significant heat loss occurred in the piping between the pre-heater control thermocouple and the upstream entry to the burner tile. A smaller, but added cooling effect was aspiration of room temperature natural gas. The radiosity was then measured, and the process repeated for various preheated mixture temperatures.

Radiosities were measured using the total radiation pyrometer described in accompanying work[1].

Combustion product analyses were undertaken using an enclosure and a stack gas analyzer[1]. Reported gas constituent concentrations were normalized to 3% oxygen levels. The lean limit for each burner was determined as the mixture at which combustion extinguished; after a 5 min soak at a stoichiometric mixture, steps of -1% excess gas with 1 min delays between steps followed until combustion ceased.

A schematic of the spectral radiometer[2] is shown in Figure 1. A sheathed bundle of mixed metal fluoride fibers with a sapphire window was positioned to fill the field of view (24°) of its optical entry with radiation from the burner. The fiber optic cable fed into the spectrometer enclosure where a rotating chopper periodically interrupted the light source so that the detector could measure and subtract background radiation (lock-in amplifier). The light was reflected onto one of two diffraction gratings, specified for use in the ranges: 800-2000 nm, and 2000-6500 nm. The diffraction grating rotated on a turret, bringing differing wavelengths of diffracted light in coincidence with the detector. The diffracted light was transmitted through a filter prior to reaching the PbSe detector to remove secondary diffraction intensities. Different filters were automatically rotated into position depending on the wavelength range being analyzed.

The spectral radiometer was calibrated using the same graphite and steel cavities as described in the accompanying work[1]. The signal of the PbSe detector is a function of not only the irradiation on the field of view of the fiber optic cable inlet, but also attenuation from the fibers, collimating mirrors, etc. along the optical path to the detector. These will all vary with wavelength; thus, calibration needed to be performed at all wavelengths used. Spectral radiosity measurements (and hence calibrations) were performed at 100 nm intervals from 1000 to 5000 nm. The calibration factors were in terms of spectral radiosity per volt, where the spectral radiosity was determined from Planck's blackbody law, using the known temperature of the back wall of the blackbody. This calibration needed only to have been performed for a blackbody at a single temperature. However, to check for reproducibility, the calibration was performed at five different temperatures for the steel cavity from 895 to 1086°C, as shown in Figure 2. The graphite cavity resulted in formation of appreciable CO_2 vapor in the optical path, resulting in bumps in the calibration data set in the wavelength ranges 2600-2900 and 4200-4400 nm. The calibration data set from

Figure 1: Spectral radiometer with fiber optic sighting[2].

Figure 2: Calibration of the spectral radiometer. The vertical dashed line represents the wavelength at which the diffraction grating was replaced. ○: graphite at 1024°C, □: steel at 895°C, △: steel at 945.5°C, ×: steel at 1044.5°C, +: steel at 1086.5°C.

the steel cavity at 945.5°C was adopted.

Spectral radiosity data from the burners was fit to Planck's equation assuming greybody emittance:

$$R_T(\lambda) = \frac{\epsilon 2\pi hc^2}{\lambda^5 \left(\exp\left(\frac{hc}{\lambda kT}\right) - 1\right)} \quad (1)$$

where $R_T(\lambda)$ is the temperature dependent spectral radiosity of a diffuse grey radiating surface, ϵ is the greybody emittance, h is Planck's constant, c is the speed of light in vacuum, k is Boltzmann's constant, and T is absolute temperature. Experimental results were fit by method of least squares to this equation, with temperature and emittance as coefficients, using the simplex method of computer iteration[4]. From this analysis, the best-fit surface temperature and greybody emittance of the burner was calculated. Wavelength ranges 2100-2500 and 3000-4000 nm were used for the simplex numerical optimization. Other wavelength ranges represent regions of H_2O and CO_2 absorption and emission[5] which would alter the measured value of spectral radiosity from that emitted strictly by the solid.

3 RESULTS

Figure 3 shows the effect of burner orientation. Although the effect was minor, a 45° downward orientation resulted in a slightly higher efficiency throughout. At low combustion intensity, a horizontal orientation fostered a comparatively low efficiency, while the reverse was true for the highest tested combustion intensity. Downward orientation caused the burner housing to sustain a higher temperature, as shown in Figure 4. The 45° upward direction corresponds to an orientation where the flow stream of exhausted combustion products pointed most directly at the room exhaust inlet. Figure 5 shows that the upstream face the burner decreased in temperature, while the downstream face increased in temperature, with increasing flow rate. In the range of combustion intensities evaluated, the burner housings heated to temperatures between 50 and 100°C (Figure 6). An exception was the Krieger burner whose housing temperature reached as high as 179°C.

Most burners were able to function under lean conditions up to -40-50% excess gas (Figure 7). The Solaronics burner showed the highest lean limit (-51%) while the Acotech burner showed the lowest (-41%).

The results of stack gas analyses as a function of mixture for the Solaronics burner

Figure 3: Effect of burner orientation on efficiency for the Acotech burner. High to low flow rate study. Mixture: 6.5% excess gas.

Figure 4: Effect of burner orientation on housing temperature for Solaronics burner. High to low flow rate study. Mixture: 6% excess gas.

Figure 5: Burner front, back and housing temperatures with combustion intensity, varied from high to low for the Hi-Tech burner. Mixture: 7.5% excess gas.

Figure 6: Housing temperatures for various burners tested from high to low combustion intensity.

Figure 7: Mixture at which combustion was extinguished for various burners.

are shown in Figure 8. The NO_x levels generated by the three burners as a function of combustion intensity is shown in Figure 9. It should be noted that the combustion product stream temperature measured at the stack gas analyzer probe correspondingly increased with combustion intensity, as shown in Figure 10.

The effect of air pre-heating on burner efficiency is shown in Figure 11. Over a 120°C interval in preheated mixture temperature, the efficiency rose by ~3.2%. The effect of preheating predicted by the maximum efficiency model[1] is shown in Figure 12. In this determination, the sensible heat associated with the temperature rise of the combustible mixture with temperature was added to the heat of combustion in the determination of radiating surface temperature. This sensible heat was not added to the heat of combustion in the denominator of the subsequent calculation of efficiency.

Radiation spectra for the Solaronics burner for various combustion intensities are shown in Figure 13. Similar spectra for other burners are shown in Figures 14 through 16. Peaks corresponding to gaseous emissions and absorptions are of significant intensity for the Acotech and Marsden burners, compared to the Solaronics and Krieger burners. Using a simplex fit of these data to equation 1, the surface temperatures of the burners were determined from their spectra, and are shown in Figure 17. These are compared to surface temperatures determined via a contact thermocouple junction for the Solaronics and Krieger burners. Greybody emittances as a function of burner surface temperatures (both determined from spectral data), are shown in Figure 18. This figure also shows the variation of emittance with temperature for various materials from the literature[6]. Using the determined values of greybody emittance, a maximum possible temperature of the burner surface was calculated using the theoretical maximum efficiency model[1]. These temperatures are compared against those measured by spectral means in Figure 19. From the temperatures and greybody emittances determined from spectral measurements, radiosities as a function of combustion intensity were determined using the Stefan-Boltzmann law. Efficiencies were then determined by dividing radiosity by the combustion intensity, and are shown in Figure 20. This figure also shows efficiencies determined by total radiation pyrometry to facilitate comparison.

Figure 8: CO, CO_2, O_2, NO_x (open circles), and temperature (solid circles) analyses from the stack gas analyzer for the enclosed Solaronics burner at 220 kW/m^2. To obtain oxygen content in percent, multiply by 0.062. To obtain CO content in ppm, multiply by 85.04. To obtain NO_x content in ppm, multiply by 0.35. To obtain CO_2 content in percent, multiply by 0.117.

Figure 9: NO_x levels for various enclosed burners. Mixtures in percent excess gas: Acotech: 7.5, Solaronics: 6, Krieger: 6

Figure 10: Combustion product stream temperatures measured at the stack gas analyzer probe.

Figure 11: Radiosity/efficiency of the Hi-Tech burner with preheat of the upstream mixture. Firing conditions: 10% excess gas, 361 kW/m^2.

Figure 12: Effect of mixture preheat temperature on the ideal burner (no flame support layer) efficiency.

Figure 13: Spectral radiosities (symbols) of the Solaronics burner, evaluated at various combustion intensities. Lines represent best-fit greybody Planck's functions (equation 1) to experimental data. High to low combustion intensities were used with a 5 min initial soak, and 2 min delay before spectra were collected at each combustion intensity. Each spectra collection required approximately 3 min.

Figure 14: Spectral radiosities of the Acotech burner. See caption for Figure 13.

Figure 15: Spectral radiosities of the Krieger burner. See caption for Figure 13.

Figure 16: Spectral radiosities of the Marsden burner. See caption for Figure 13.

Figure 17: Surface temperatures of various burners based on a simplex fit of spectral data to equation 1 (SR), or via a thermocouple junction in contact with the burner base or flame retention plate (TC).

Figure 18: Emittances of burner surfaces, and materials from the literature[6]. Experimental emittances and temperatures were determined by a simplex least squares fit of spectral radiosity data to equation 1.

Figure 19: Solid symbols: surface temperatures from the theoretical maximum efficiency model. Open symbols: surface temperatures determined from the spectral radiometer.

Figure 20: Comparison of efficiencies of commercial burners as determined by the total (TR, open symbols) and spectral (SR, solid symbols) radiation pyrometers.

4 DISCUSSION

The burner orientation study (Figure 3) indicated that orientation did not appreciably effect burner efficiency. A downward orientation fostered the highest efficiency; buoyant combustion products were forced to swirl back in contact with the radiating solids as well as the burner housing. This would improve convective heat transfer to the solid, and the increased burner housing temperature (Figure 4) would function to preheat the upstream gas/air mixture. The potential drawback of this orientation is that excessive heating of the housing (see Krieger burner, Figure 6), increases the potential for ignition of the premix, causing flashback. The horizontal orientation had the interesting behavior of having the lowest efficiency at low combustion intensities, and the highest efficiency at high combustion intensities. It is speculated that at low flow rates, cold air was drawn into the burner by the negative pressure of the moving combustion products, decreasing radiosity/efficiency. At high flow rates, the high volume of exhaust combustion products prohibited convective cooling, and the burner behaved similarly to that of 45° downward orientation.

The downstream surface of the burners increased in temperature with combustion intensity. However, the upstream surface temperature of the Hi-Tech burner tile (Figure 5) decreased with increasing combustion intensity. This can be attributed to the cooling effects of the increasing flow rate of cold mixture dominating over back-conduction from the hot downstream face. This trend would be expected for the other burners as well. The competing effects of incoming mixture and downstream face temperatures tended to maintain the burner housing temperatures constant with combustion intensity. The Krieger burner housing was roughly 80-100°C higher in temperature than for the other burners (Figure 6). Heat from the Krieger burner housing would undoubtedly contribute to conduction losses to the surrounding ambient, but at the same time, function to preheat the incoming gas/air mixture. The drop-off in burner housing temperature at high combustion rates is due to the start-up transient before the burner housing reached a steady state temperature.

Starting from -20% excess gas (lean combustion side), NO_x levels increased with increasing percent excess gas, then decreased as stoichiometric combustion was reached[1]

[1] As discussed in the accompanying work[1], true stoichiometric combustion corresponds to an indicated mixture of ~8% excess gas.

(Figure 8). The increase in NO_x levels corresponds to an increase in combustion intensity; this increased the combustion product temperature, in turn increasing thermally generated NO_x. The decrease in NO_x content as stoichiometric combustion was approached can be attributed to the decrease in available oxygen to react with nitrogen to form NO_x. The increased NO_x levels for rich mixtures may be attributed to loss of calibration of the electrolytic sensor in reducing atmospheres.

The measured NO_x levels of all tested burners as a function of combustion intensity ranged from 16 to 38 ppm (Figure 9). For a given combustion intensity, NO_x concentration appears to increase with downstream combustion product exhaust temperatures (Figure 10). The temperature within the enclosure would be determined from a heat balance between heat absorbed from burner radiation plus the sensible heat of combustion products, and the heat loss between the enclosure and the ambient. Larger burners required a greater volume flow rate to maintain a given combustion intensity, and would thus release more heat per unit time to the enclosure. This would foster a comparatively higher average temperature of the combustion product stream in the enclosure. The higher average combustion product temperature in the enclosure would translate to a longer residence time at elevated temperature as combustion products depart the burner, encouraging NO_x production. The Acotech burner showed ineffective convection from combustion products to the solid, resulting in comparatively very high exiting combustion product temperatures (see subsequent discussion). However, the small size of the burner caused rapid quenching of the temperature of combustion products as they propagated into the enclosure. The low corresponding NO_x production of this burner implies that NO_x production was more a function of residence time at elevated temperature than the peak value of temperature. Based on this discussion, the reported NO_x values are an artifact of the size of the enclosure relative to the size of the burner, and cannot be assigned as a characteristic of the burner.

The effect of air pre-heating on efficiency follows closely that predicted by the maximum efficiency model. A 120°C increase in mixture temperature resulted in a measured 3.2% increase in efficiency, while a 3.7% increase is predicted by the model. Additional increases in efficiency with greater preheating cannot realistically be anticipated since the minimum ignition temperature of some of the hydrocarbons in natural gas may be reached.

The wavelength range 2500-3000 nm corresponds to emission/absorption from both

CO_2 and H_2O, while the wavelength range 4000-5000 nm corresponds to emission/absorption strictly from CO_2[5]. The Acotech and Marsden burners show significantly more intense CO_2 emission peaks (Figures 14 and 16) than the Solaronics and Krieger burners (Figures 13 and 15). This implies significantly improved convective heat transfer between combustion products and solid surfaces for the latter two burners, in turn, decreasing combustion product temperatures. For the latter two burners, a net absorption from CO_2/H_2O gases at 2500-3000 nm is observed, while a net emission is apparent for the former two burners. It is interpreted that the hot combustion products contribute to emission, while near-room temperature CO_2 and H_2O in the optical path to the detector function as absorbers of radiant energy in the same spectral bands. Only 0.03% of standard air is composed of CO_2, while at 50% relative humidity, ambient air is composed of 1.3% water vapor[7][2]. This would imply that of the two, water vapor would be the significant absorbing species in the optical path. This would explain why net absorption is never indicated in the 4000-5000 nm (CO_2 only) range. The negative deviations in the 2500-3000 nm range for the Solaronics and Krieger burners indicate that ambient water absorption dominated over emissions from hot CO_2/H_2O. This was not true for the Acotech and Marsden burners, since the exiting combustion products did not effectively convect their thermal energy to the solids, thus emissions from the very high temperature combustion products dominated over downstream absorption. The more intense H_2O absorption demonstrated for the Solaronics burner relative to the Krieger burner may simply be due to higher relative humidity in the room the day the former burner was tested.

The temperatures measured by spectral means for the Krieger burner (Figure 17) were roughly 30°C higher than that indicated by the thermocouple in contact with the flame retention plate. The spectrally determined temperature would be influenced by radiation from both the flame retention plate and the lower temperature screen; the spectrally determined temperature would be lower than the temperature of the flame retention plate alone. Significantly elevated temperatures (~225°C) were measured by the thermocouple junction in contact with the ceramic base of the Solaronics burner, as compared to those measured by spectral means. By comparison, the aforementioned lower screen temperature effect would not be enough to explain this temperature difference. For

[2]Partial pressure values of H_2O and CO_2 in this work would be higher due to contributions from the burner; however not appreciably, since the laboratory air was continuously refreshed via an exhaust hood near the burner.

the Krieger burner, combustion took place between the nozzle exits and the upstream side of the flame retention plate. Un-reacted mixture would not be present on the downstream face of the flame retention plate, where the thermocouple junction was making contact. This would not be true for the Solaronics burner, where ignition took place as mixture exited the capillaries. The thermocouple junction was in contact with the ceramic surface very near one of these exits, and it is likely that the Pt thermocouple junction catalyzed combustion on its surface. In this sense, it is clear that spectral measurements are a useful method of measuring surface temperature as compared to using a thermocouple junction. However, the spectral method determines an averaged temperature if the base and flame support layer are at different temperatures. Correspondingly, the spectral method determines an averaged greybody emittance when the base and flame support layer are made of different materials.

For the same combustion intensity, the surface temperature of burners without flame support layers was significantly lower than those having them. This is consistent with Figures 14 and 16 where gaseous emission peaks for the Acotech and Marsden burners imply significant temperature differences between solid and combustion product temperature. All burners showed imperfect convective heat transfer to solid surfaces, as evidenced by significant temperature differences between optically measured and theoretical maximum solid temperatures (Figure 19).

The spectrally determined greybody emittance of the Krieger burner was a good match to the literature value for stainless steel. The Marsden burner had a higher and more grey emittance than that expected of an oxide glass. Glass is generally transmissive for wavelengths shorter than ~3000 nm, and absorptive/emissive for longer wavelengths. For such a case, the 3000-4000 nm band should have been more intense, and the 2100-2500 nm band should have been less intense than the greybody fit to the spectra of the Marsden burner in Figure 14. Apparently, the zirconia content in the aluminosilicate glass fiber mat[1], fostered an increased and more grey surface emittance. The Solaronics burner, being composed of both a ceramic base and a metal screen flame support layer, would have a greybody emittance which could not be attributed to a single material. The Acotech burner showed significantly lower emittance than that expected from an oxidized steel surface. It is apparent that the fit to the model in the 2100-2500 nm range is comparatively not as good for the Acotech burner (Figure 14) as the other burners.

This casts some doubt on the accuracy of the determined values of greybody emittance and surface temperature for this burner.

The efficiencies determined via least squares fit of restricted ranges of output of the spectral radiometer fall closely below or are coincident with data from the total radiation pyrometer (Figure 20). Even though spectrally determined temperatures and greybody emittances may have represented averaged effects of base and flame support layers, they result in a Planck's function which fits very closely to experimental spectra. Thus, use of these values in the Stefan-Boltzmann equation well represent integrated spectral data. The total radiation pyrometer was sensitive to emissions from both solids and combustion products. However, since restricted spectral ranges were used from spectral radiation pyrometer data, radiosities/efficiencies reflect strictly greybody radiation from solid surfaces. Thus, the slightly higher efficiencies in Figure 20 determined from the total radiation pyrometer may be attributed to added contributions from gaseous emissions.

For low combustion intensities, the Marsden burner represents an exception to the rule that higher efficiencies are measured from the total radiation pyrometer as compared to the spectral radiation pyrometer. For this burner, the falling efficiency with decreasing combustion intensity, as determined by the total radiation pyrometer (Figure 20) is an artifact of the voluminous output of combustion products, heating the pyrometer housing. This resulted in a lower temperature difference between the detector and its housing, in turn decreasing the thermoelectric signal from the device. This effect does not occur in the operation of the spectral radiation pyrometer; thus trends in efficiency with combustion intensity for the Marsden burner using spectral data were consistent with those of other (smaller) burners.

5 CONCLUSIONS

Use of the spectral radiometer provides significant insight into the operation of gas radiant burners. The Solaronics and Krieger burners very effectively transferred the heat of combustion to solid surfaces, resulting in higher surface temperatures and radiant efficiencies. Good agreement was obtained between efficiencies determined by spectral and total radiation pyrometers.

6 ACKNOWLEDGEMENTS

The authors acknowledge Dr. Kevin Krist of the Gas Research Institute and Mr. Shyam Singh of SSEEI, Inc., for funding this investigation. This manuscript was prepared by the Georgia Institute of Technology as an account of work sponsored by the Gas Research Institute. Neither GRI, members of GRI, nor any person acting on behalf of either; A. Makes any warranty or representation, expressed or implied, with respect to the accuracy, completeness, or usefulness of the information contained in this manuscript, or that the use of any information, apparatus, method, or process disclosed in this manuscript may not infringe on privately-owned rights, or B. Assumes any liability with respect to the use of, or for damages resulting from the use of, any information, apparatus, method, or process disclosed in this manuscript.

References

[1] R. F. Speyer, W. Lin, and G. Agarwal, and R. F. Speyer, "Radiant Efficiencies of Commercially Manufactured Gas Radiant Burners", unpublished work.

[2] R. F. Speyer, W. Lin, and G. Agarwal, "Performance Evaluation of Porous Radiant Gas Burners", *Journal of Experimental Heat Transfer*, vol. 8, no. 1, pp. 73-95, 1995.

[3] M. G. Apte and G. W. Traynor, "Pollutant Emission Rates from a Radiant Fiber-Matrix Gas Burner", *Air and Waste*, **43**, (1993).

[4] R. F. Speyer, "Deconvolution of Superimposed DTA/DSC Peaks Using the Simplex Algorithm", *J. Mat. Res.*, 8 (3) 675-679 (1993).

[5] R. Seigel and J. R. Howell, *Radiation Heat Transfer*, Hemisphere Publishing Corp, (1992).

[6] F. D. Incropera and D. P. DeWitt, *Fundamentals of Heat and Mass Transfer*, 2d ed, John Wiley and Sons, New York, 1985.

[7] R. C. Weast, ed., CRC Handbook of Chemistry and Physics, 58th edition, CRC Press, Inc, Cleveland, OH, 1978.

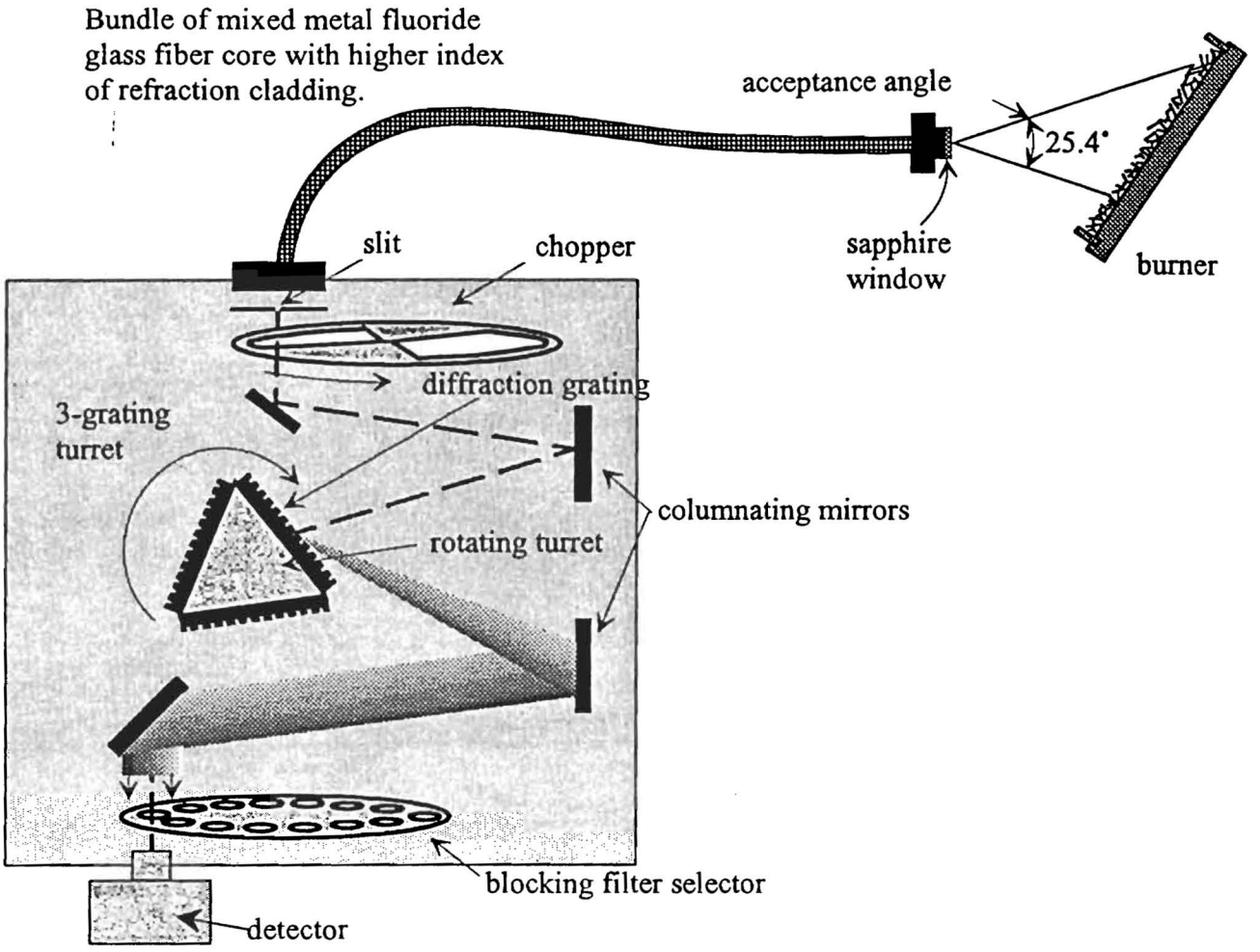
Bundle of mixed metal fluoride glass fiber core with higher index of refraction cladding.
acceptance angle
25.4°
sapphire window
burner
slit
chopper
diffraction grating
3-grating turret
columnating mirrors
rotating turret
blocking filter selector
detector

Fig 1

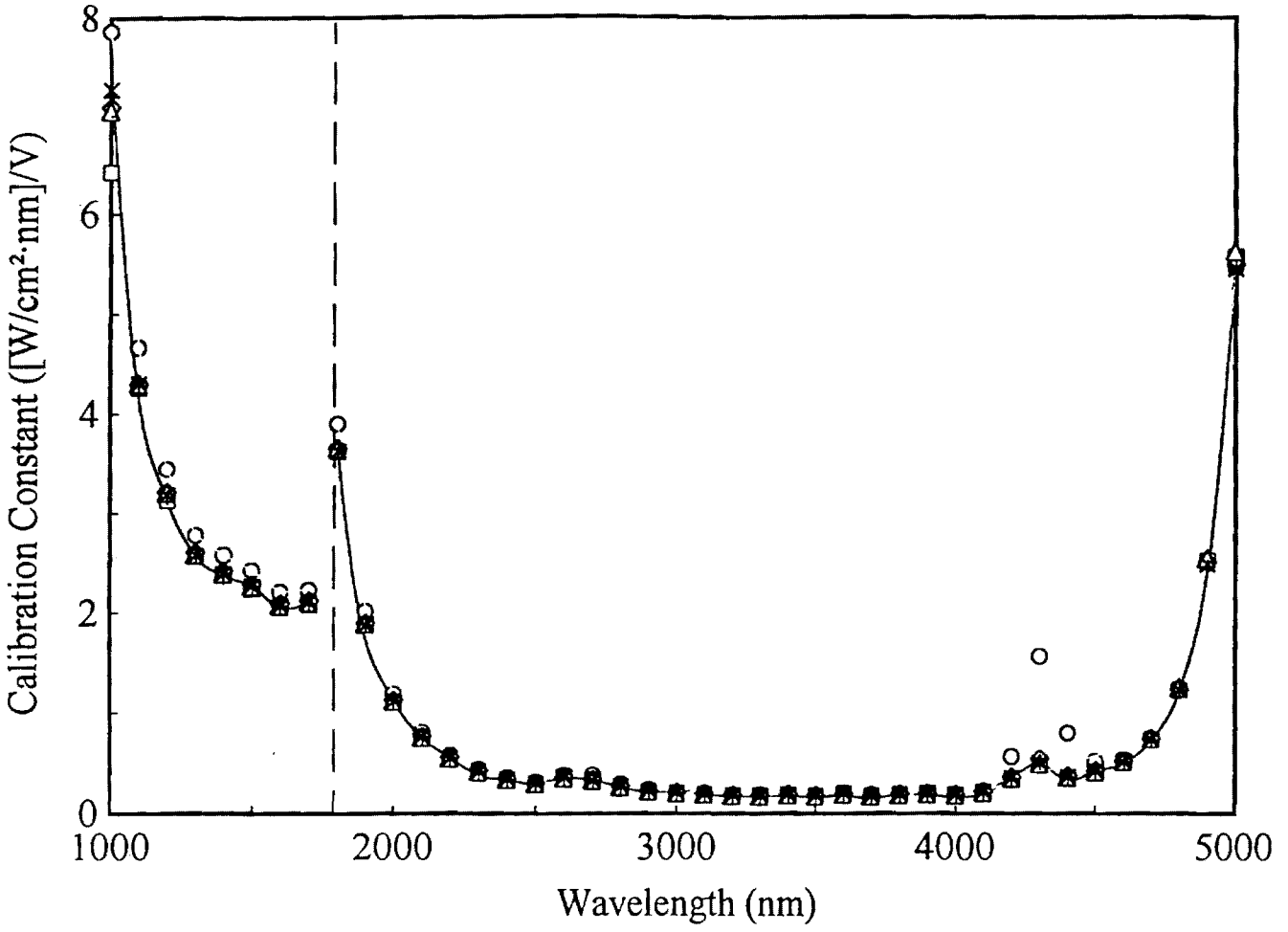
Calibration Constant ([W/cm²·nm]/V)
8
6
4
2
0
1000
2000
3000
4000
5000
Wavelength (nm)

Fig. 2

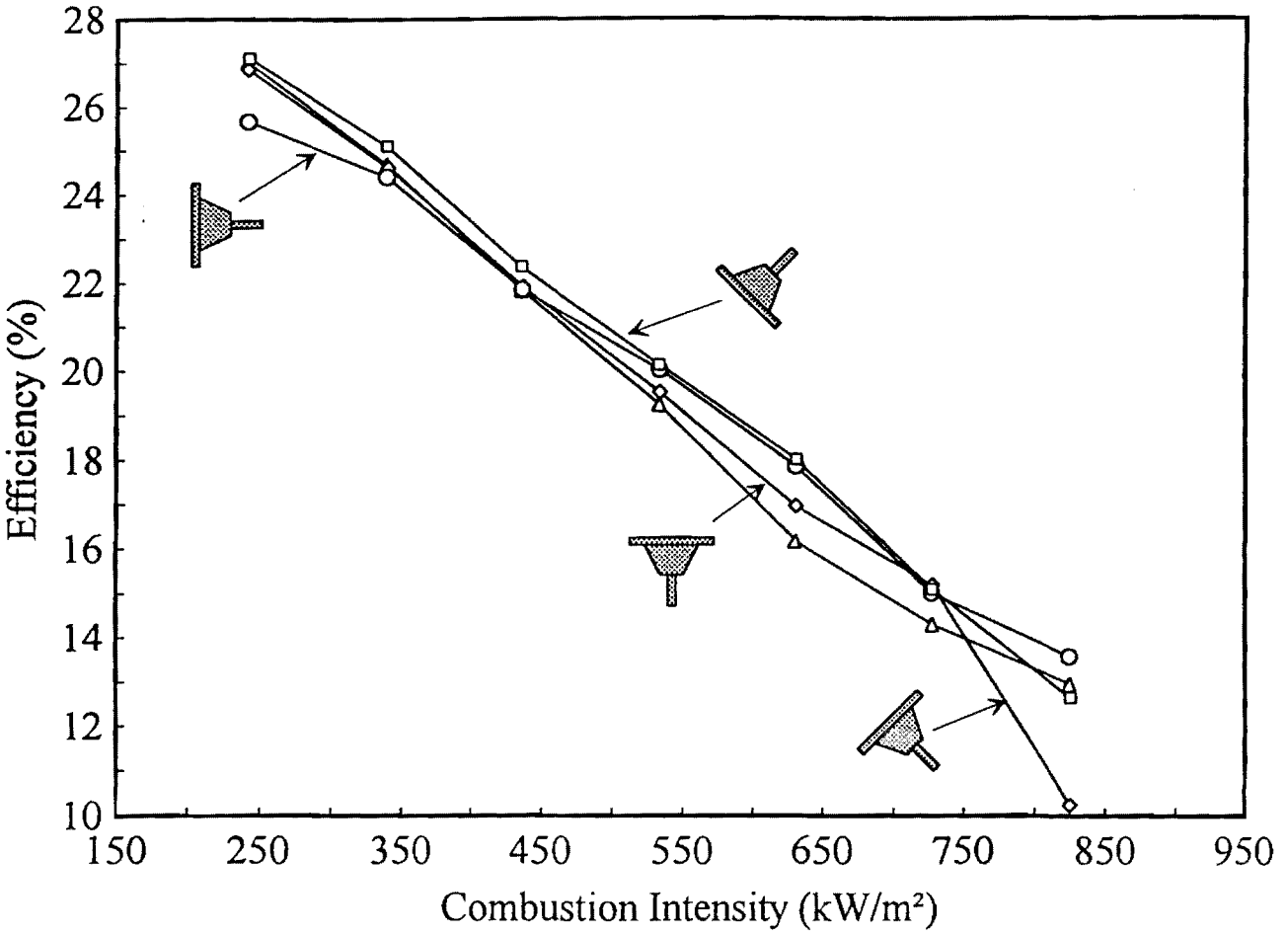
28
26
24
22
20
18
16
14
12
10
Efficiency (%)
150
250
350
450
550
650
750
850
950
Combustion Intensity (kW/m²)

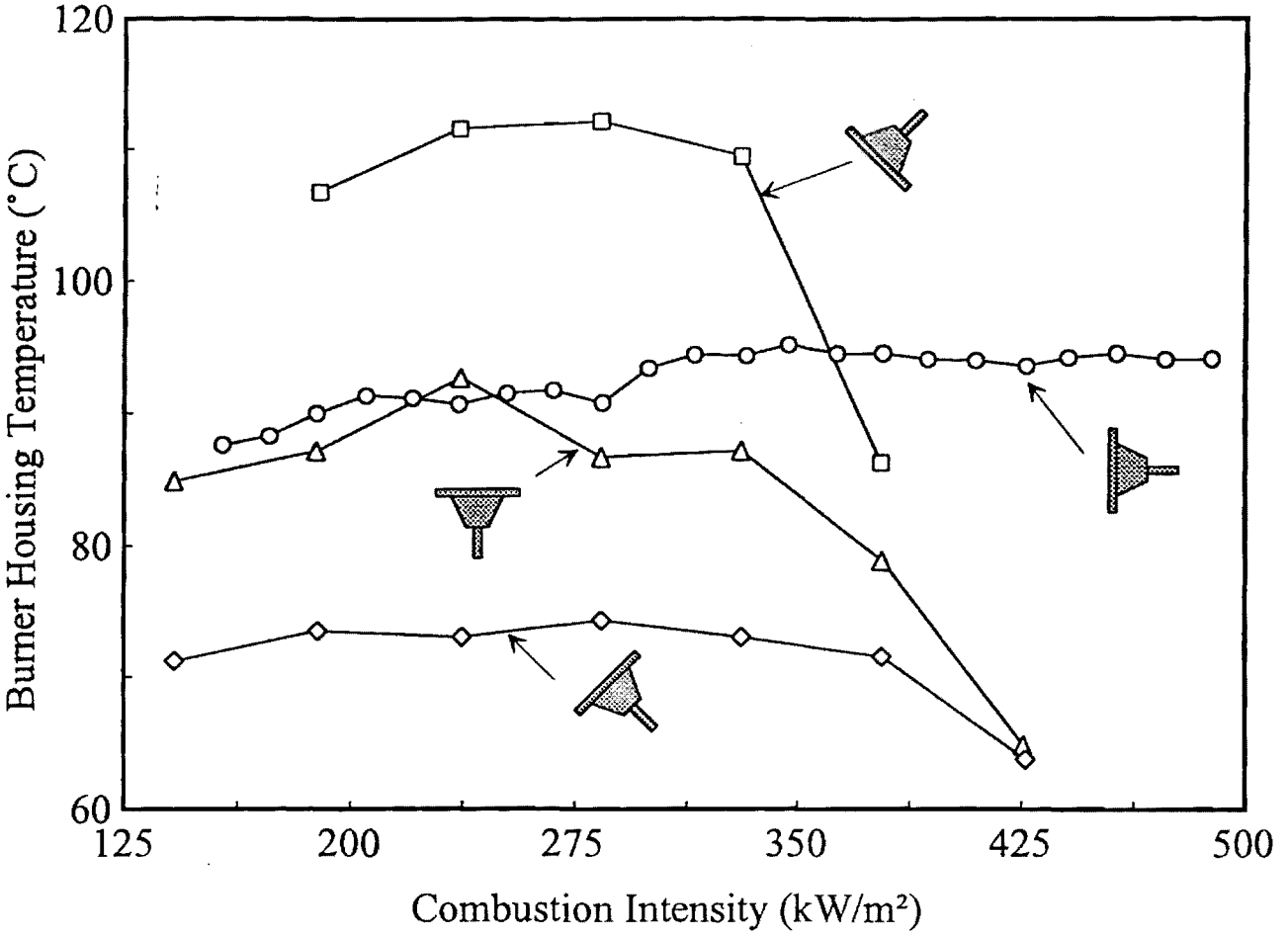
120
100
80
60
Burner Housing Temperature (°C)
125
200
275
350
425
500
Combustion Intensity (kW/m²)

Fig. 4

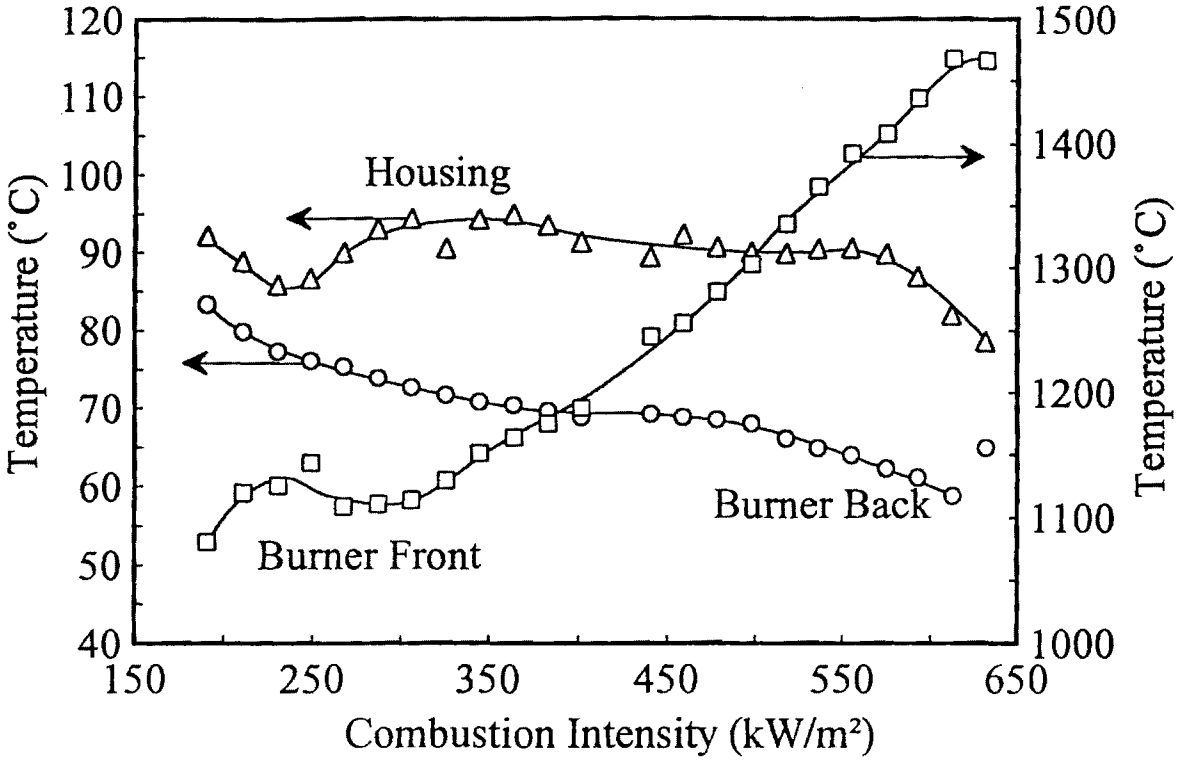
120
110
100
90
80
70
60
50
40
Temperature (°C)
1500
1400
1300
1200
1100
1000
Temperature (°C)
Housing
Burner Back
Burner Front
150
250
350
450
550
650
Combustion Intensity (kW/m²)

Fig. 5

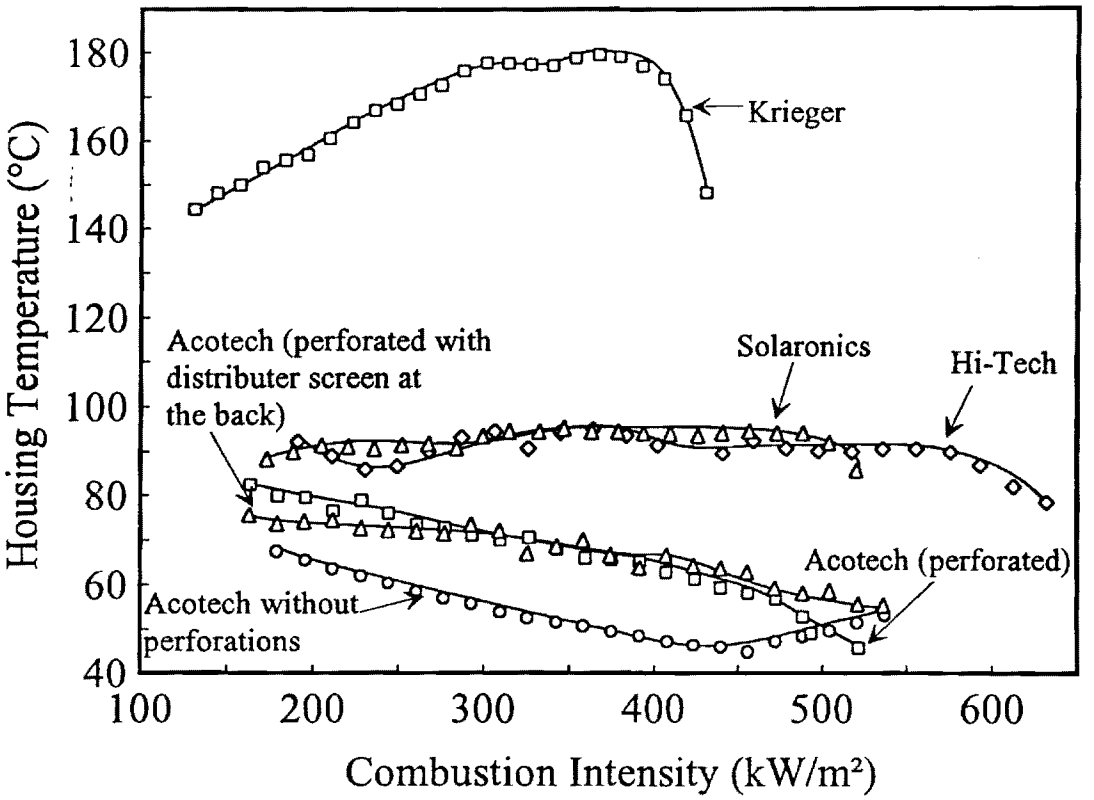
Housing Temperature (°C)
180
160
140
120
100
80
60
40
100
200
300
400
500
600
Combustion Intensity (kW/m²)
Krieger
Acotech (perforated with distributer screen at the back)
Solaronics
Hi-Tech
Acotech (perforated)
Acotech without perforations

FIG 6

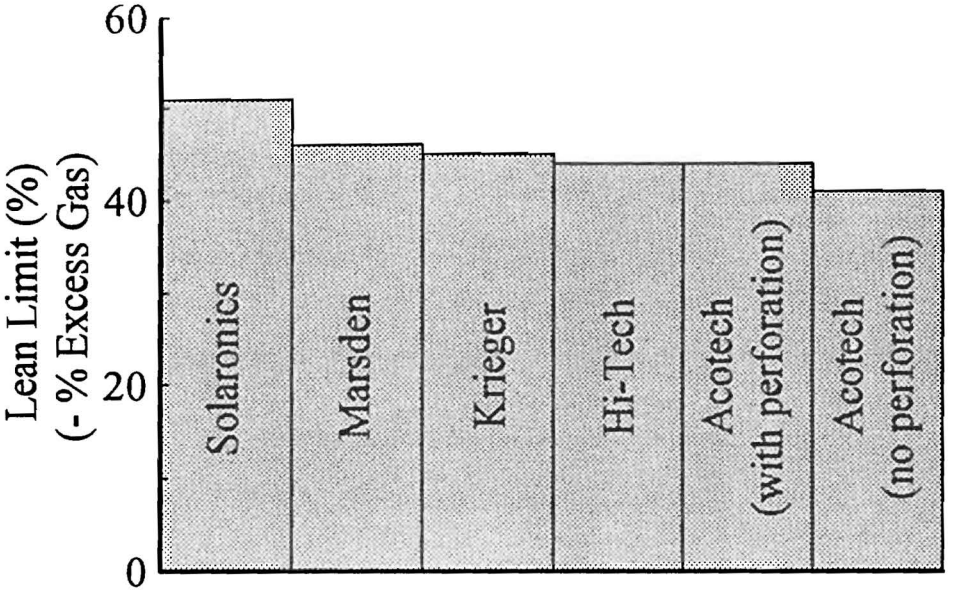
Lean Limit (%)
(- % Excess Gas)
60
40
20
0
Solaronics
Marsden
Krieger
Hi-Tech
Acotech
(with perforation)
Acotech
(no perforation)

Fig. 7

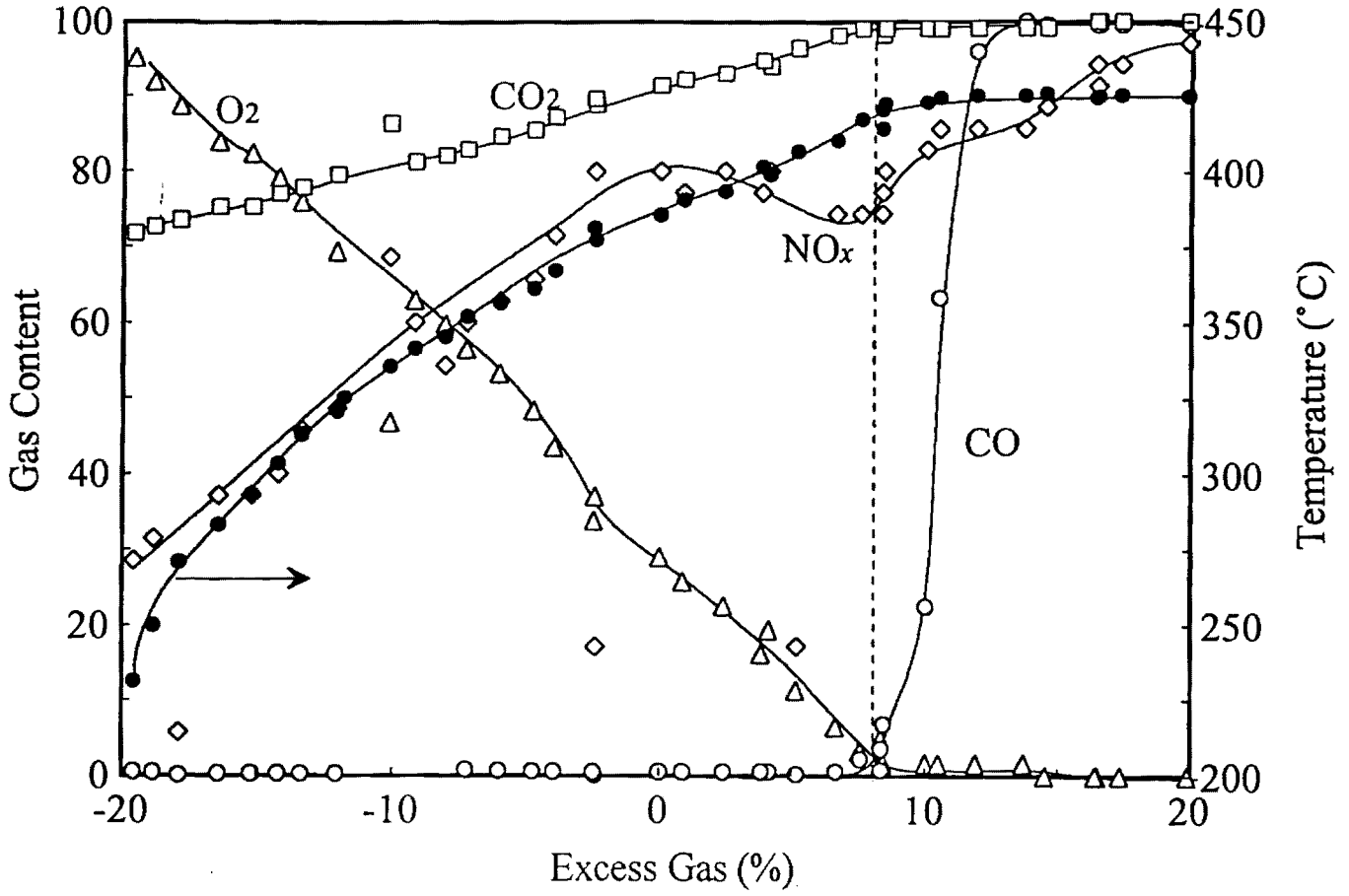
100
80
60
40
20
0
450
400
350
300
250
200
-20
-10
0
10
20
O2
CO2
NOx
CO
Gas Content
Temperature (°C)
Excess Gas (%)

Fig 2

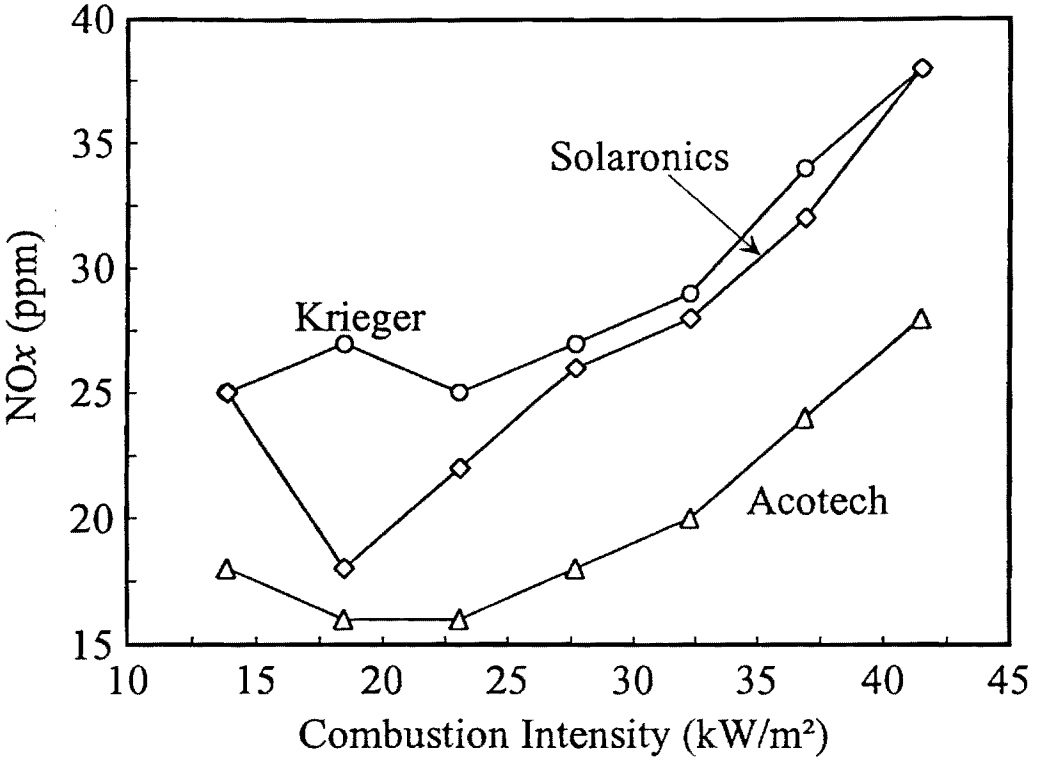
40
35
30
25
20
15
NOx (ppm)
Solaronics
Krieger
Acotech
10
15
20
25
30
35
40
45
Combustion Intensity (kW/m²)

FIG 9

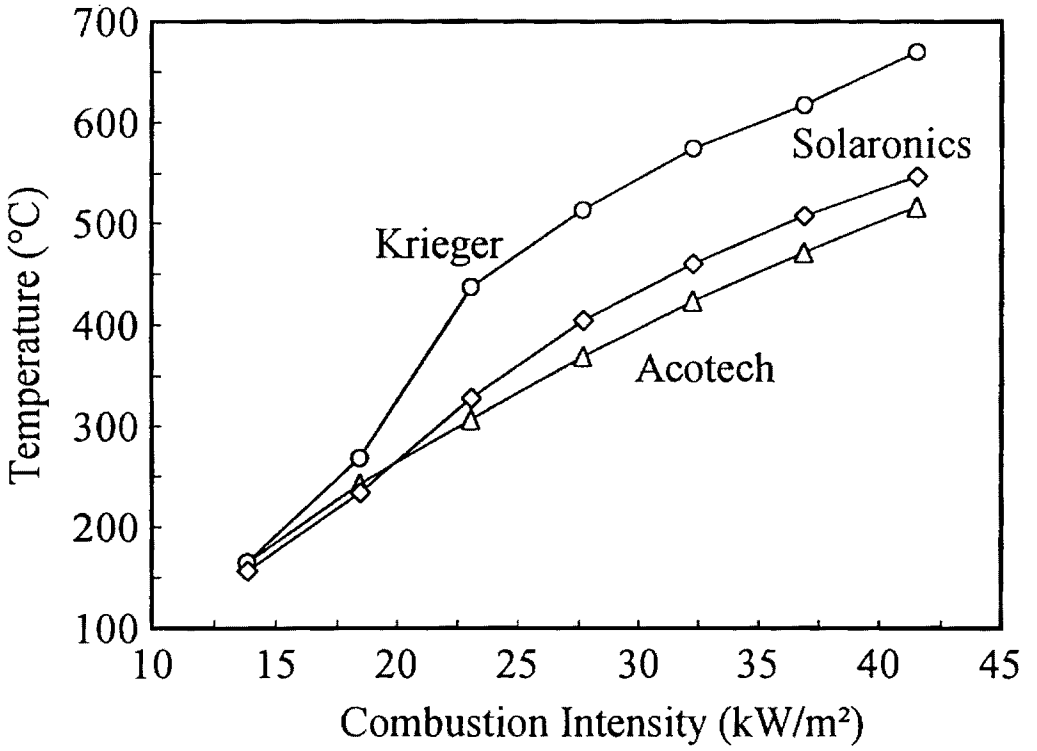
700
600
500
400
300
200
100
Temperature (°C)
Solaronics
Krieger
Acotech
10
15
20
25
30
35
40
45
Combustion Intensity (kW/m²)

FIG 10

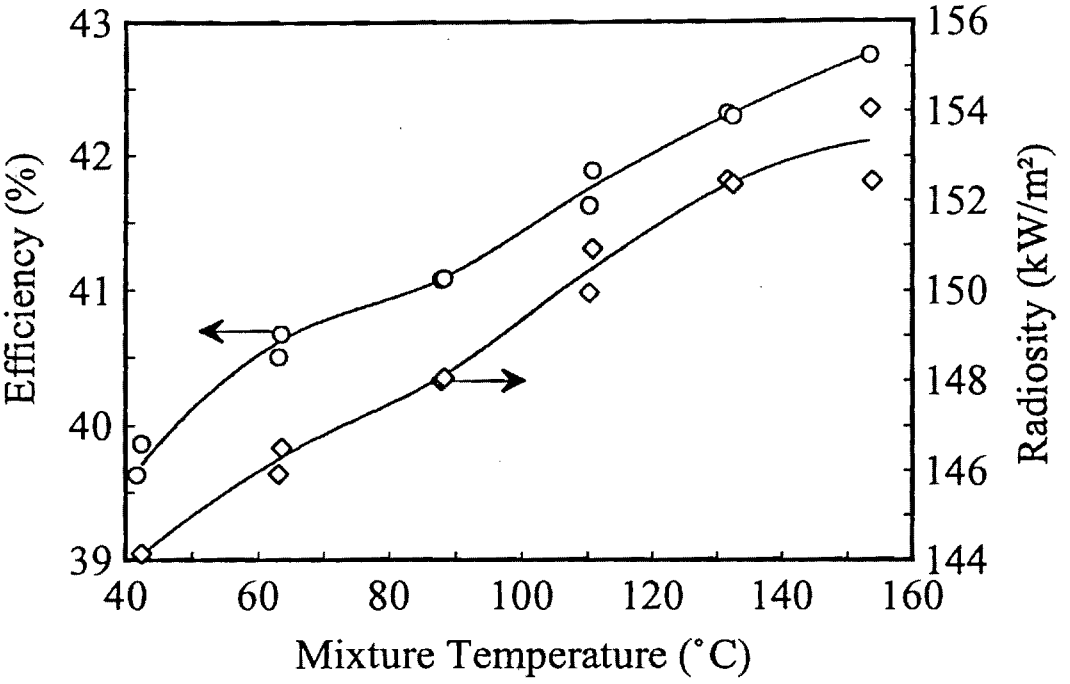
43
42
41
40
39
156
154
152
150
148
146
144
40
60
80
100
120
140
160
Efficiency (%)
Radiosity (kW/m²)
Mixture Temperature (°C)

F16 11

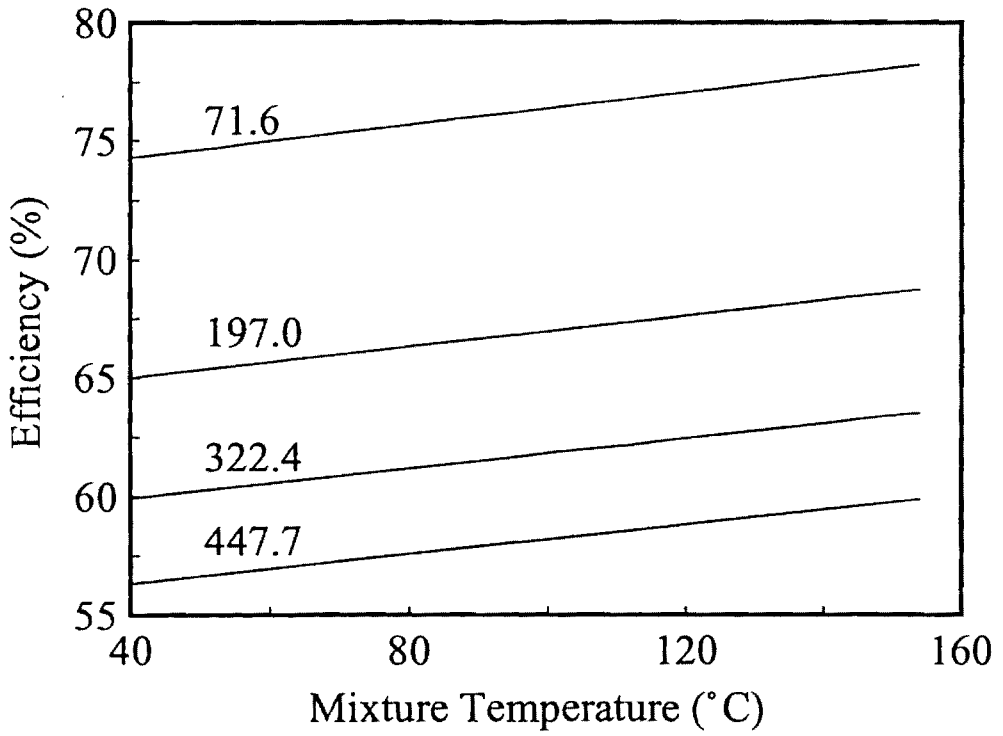
80
75
70
65
60
55
71.6
197.0
322.4
447.7
40
80
120
160
Efficiency (%)
Mixture Temperature (°C)

F16 12

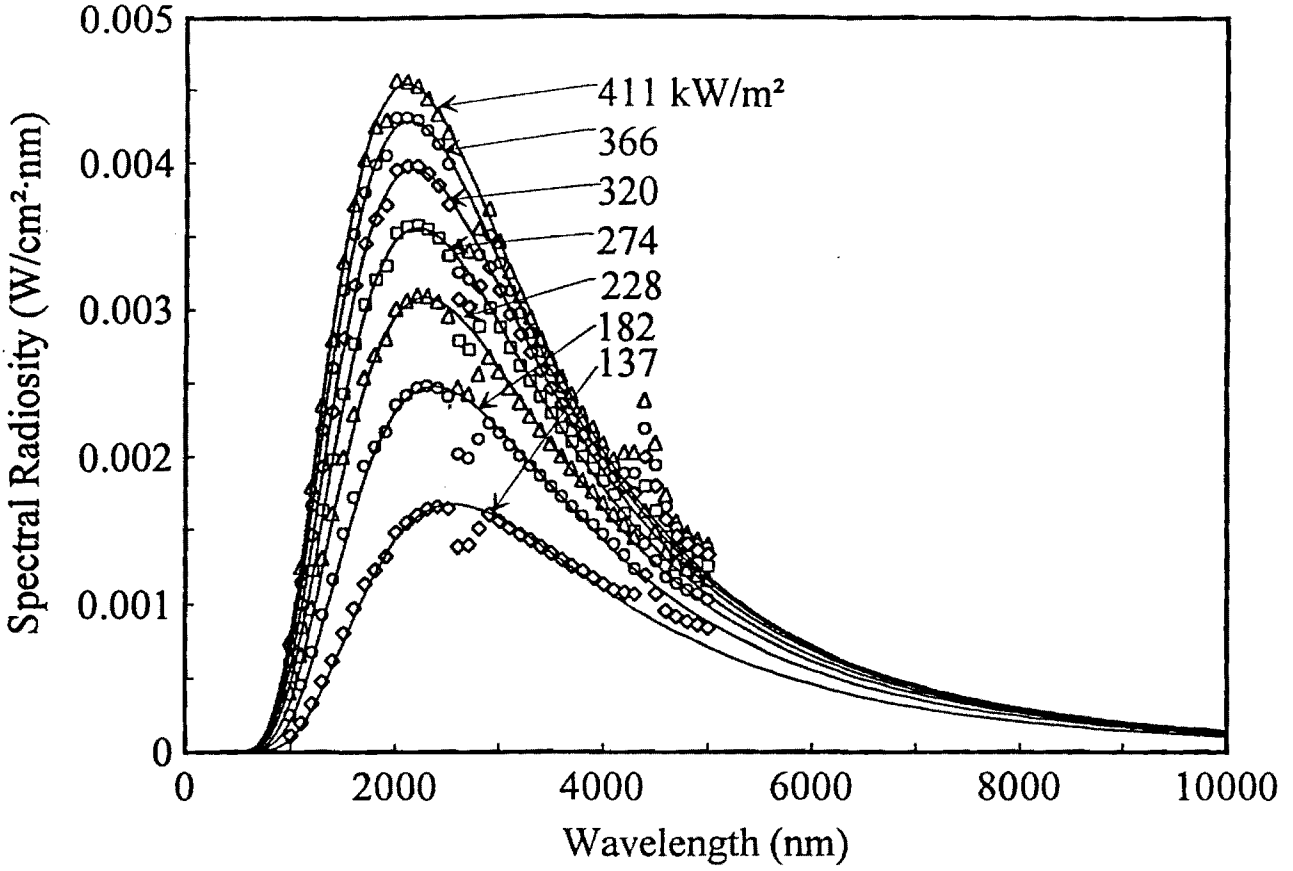

Salamanca Fig. 1

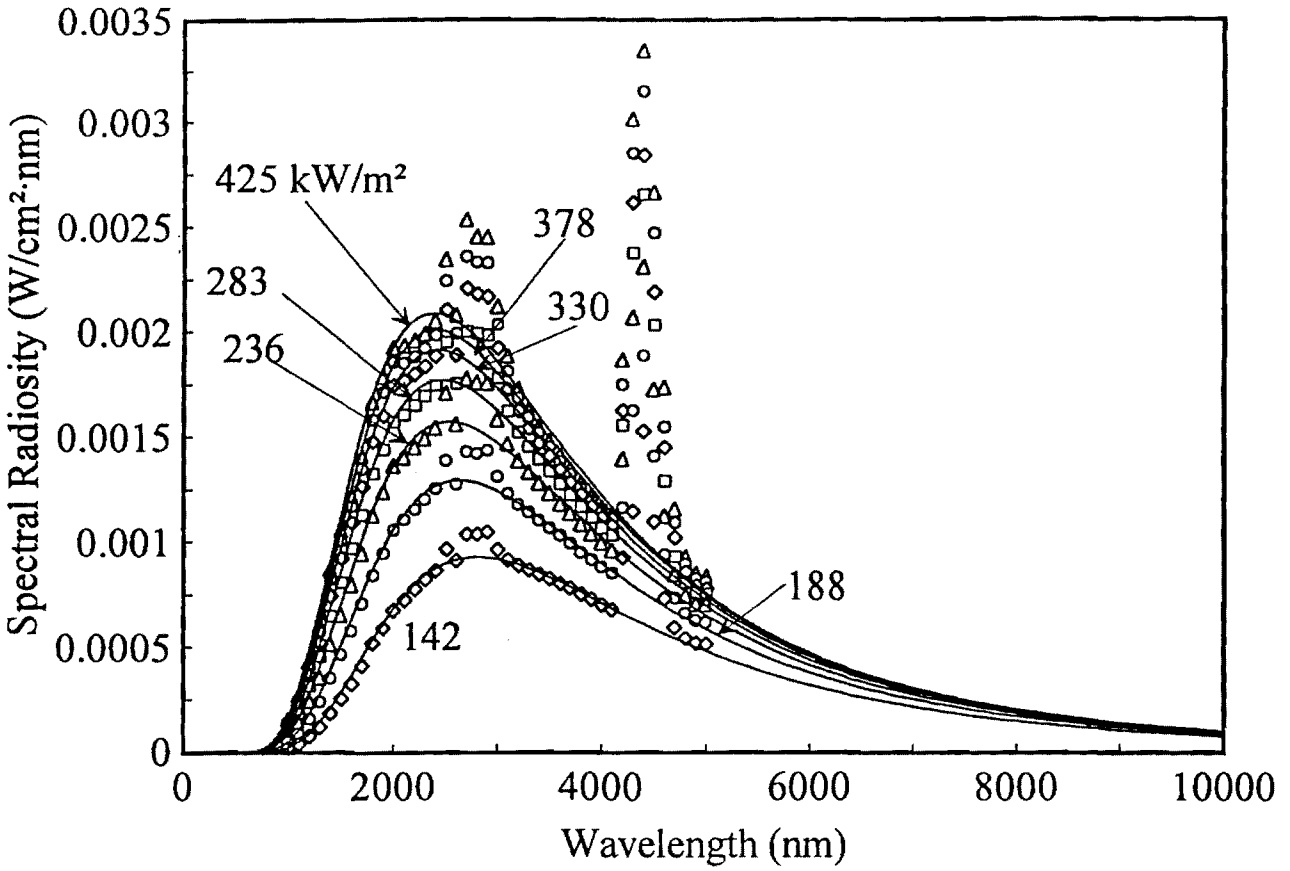

Prateek Fig. 14

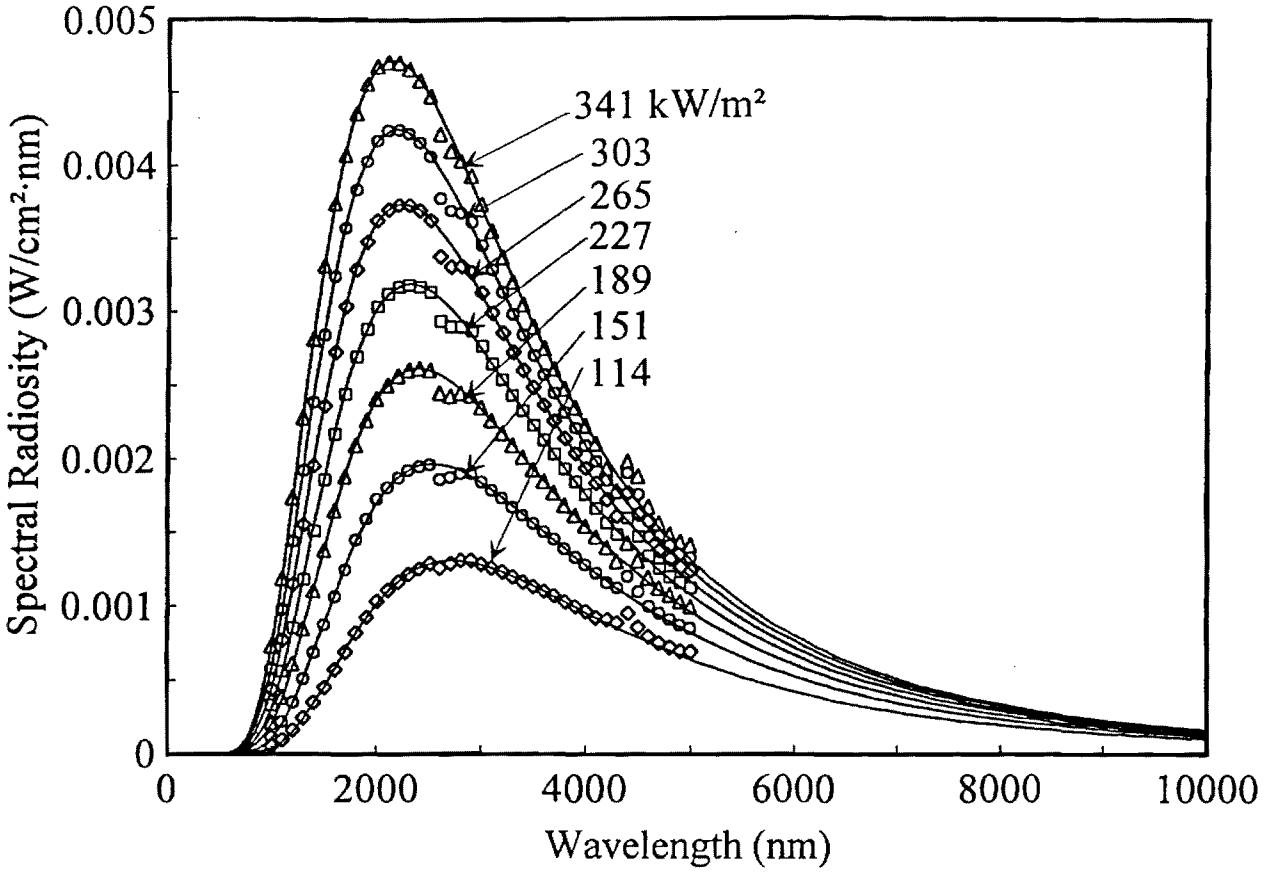
0.005
0.004
0.003
0.002
0.001
0
Spectral Radiosity (W/cm²·nm)
341 kW/m²
303
265
227
189
151
114
0
2000
4000
6000
8000
10000
Wavelength (nm)

Fig 1

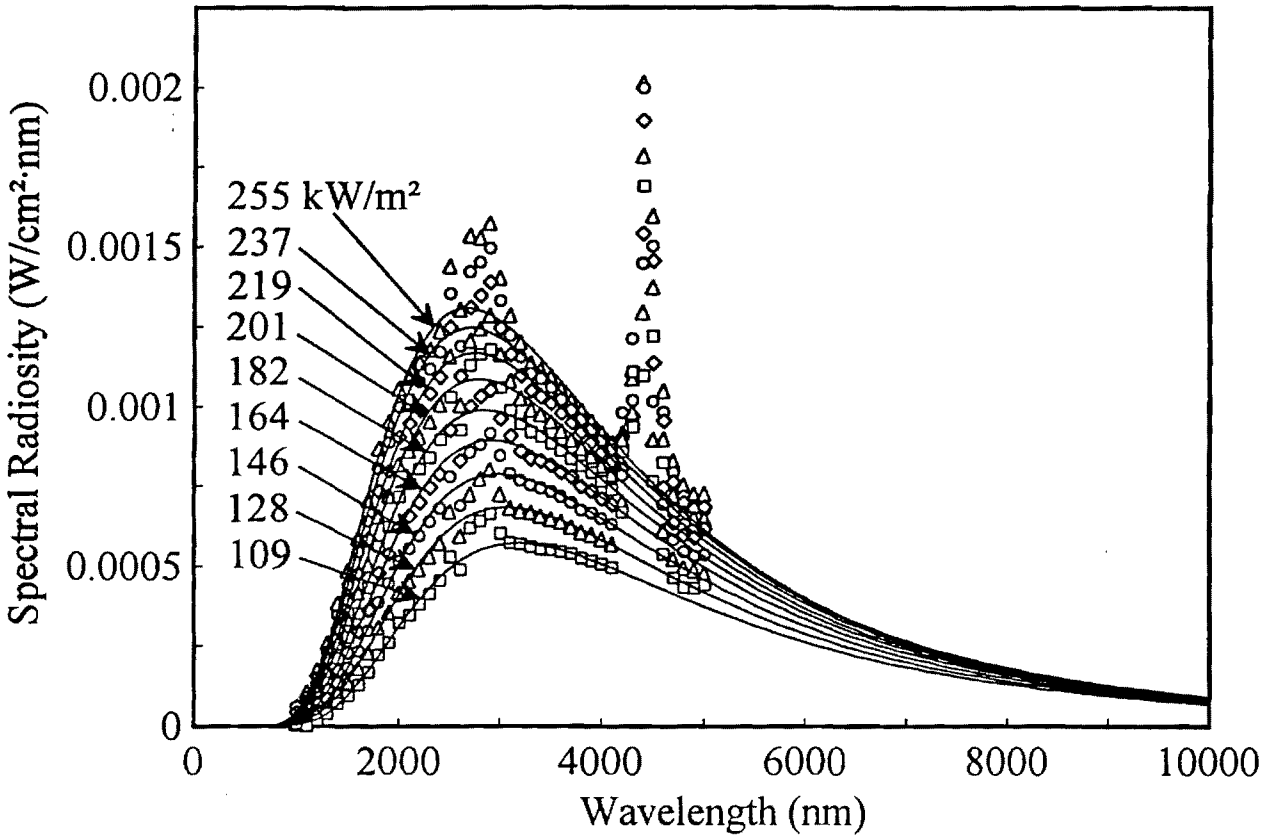
Spectral Radiosity (W/cm²·nm)
0.002
0.0015
0.001
0.0005
0
255 kW/m²
237
219
201
182
164
146
128
109
0
2000
4000
6000
8000
10000
Wavelength (nm)

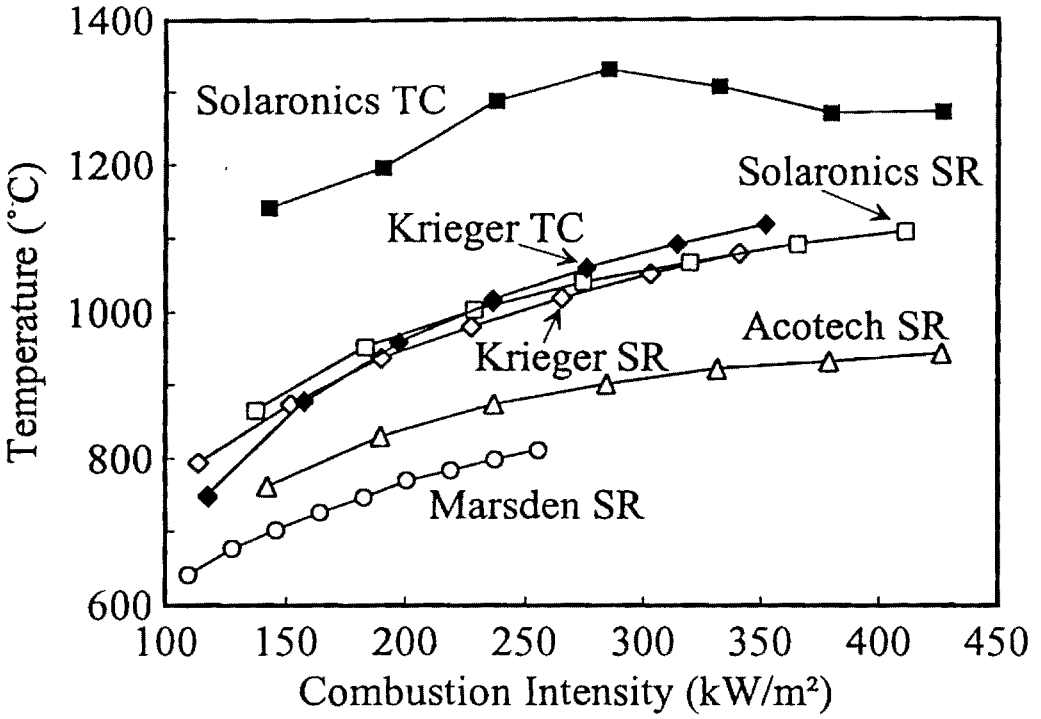
1400
1200
1000
800
600
Temperature (°C)
100
150
200
250
300
350
400
450
Combustion Intensity (kW/m²)
Solaronics TC
Solaronics SR
Krieger TC
Krieger SR
Acotech SR
Marsden SR

Fig. 17

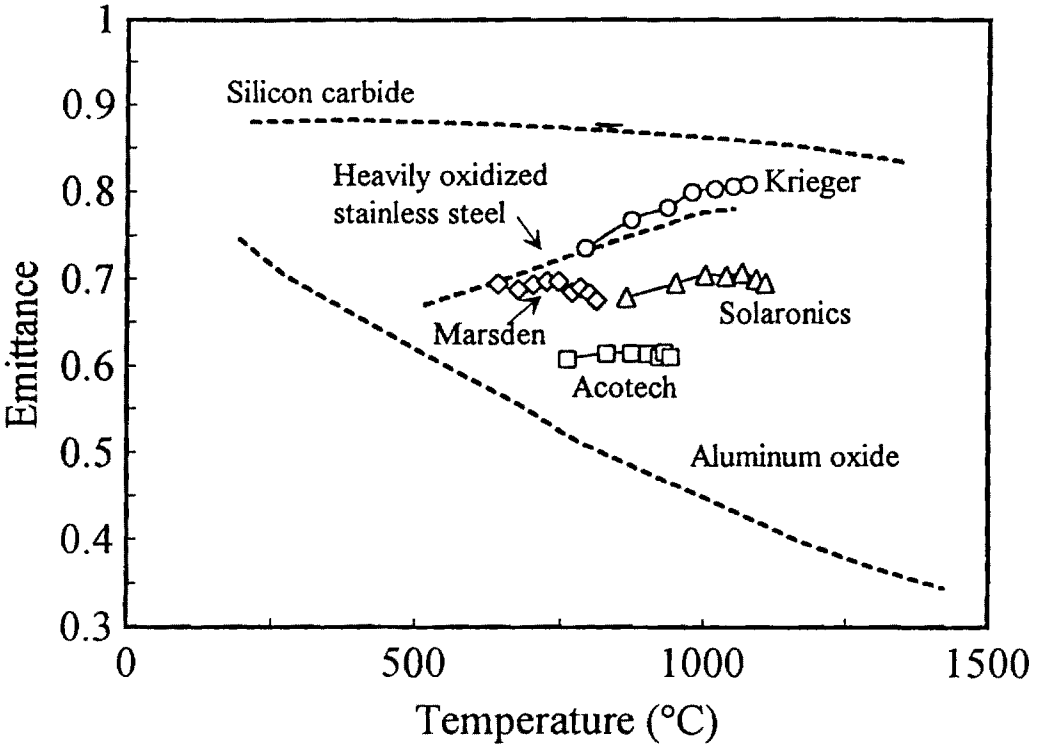
1
0.9
0.8
0.7
0.6
0.5
0.4
0.3
Emittance
0
500
1000
1500
Temperature (°C)
Silicon carbide
Heavily oxidized
stainless steel
Krieger
Solaronics
Marsden
Acotech
Aluminum oxide

Fig. 18

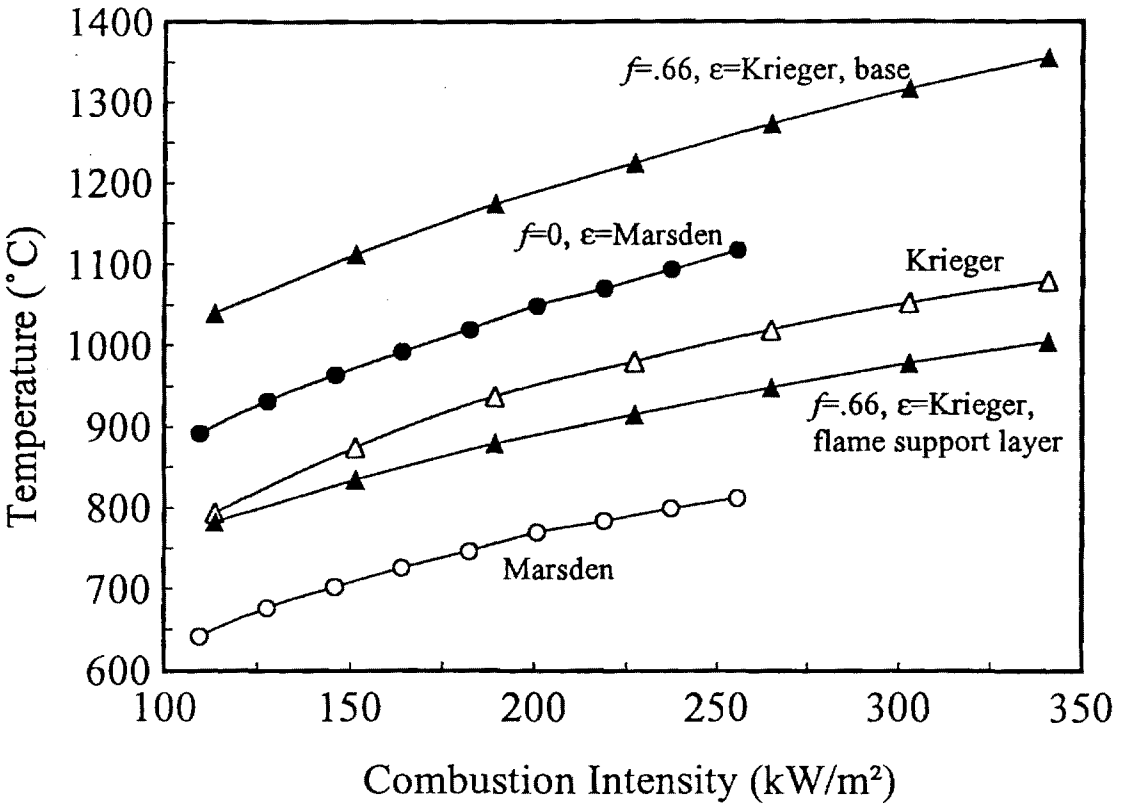
1400
1300
1200
1100
1000
900
800
700
600
Temperature (°C)
100
150
200
250
300
350
Combustion Intensity (kW/m²)
f=.66, ε=Krieger, base
f=0, ε=Marsden
Krieger
f=.66, ε=Krieger,
flame support layer
Marsden

FIG 19

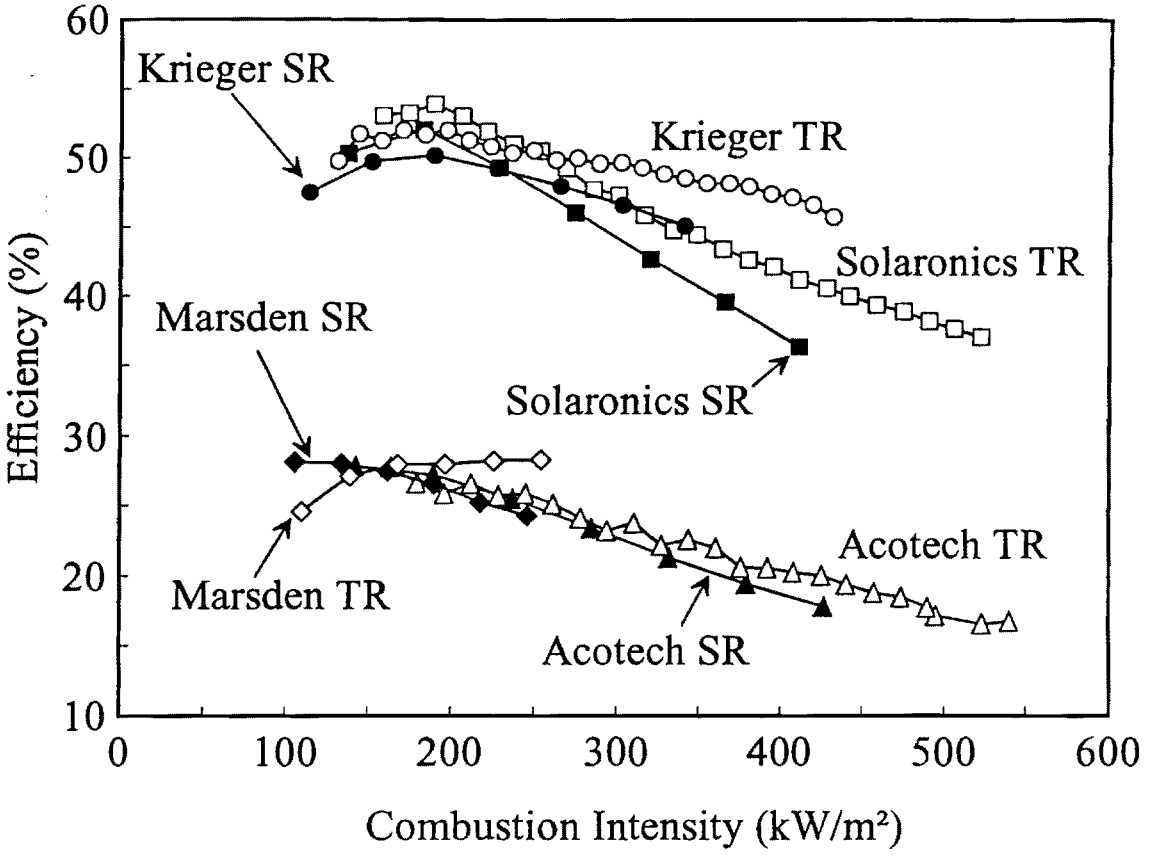
Krieger SR
Krieger TR
Solaronics TR
Marsden SR
Solaronics SR
Acotech TR
Marsden TR
Acotech SR
Efficiency (%)
Combustion Intensity (kW/m²)
60
50
40
30
20
10
0
100
200
300
400
500
600

Fig 2